

University of Alberta

**Kinetic behavior of microtubules driven by dynein motors --- a
computational study**

By

Qiang Chen

A thesis submitted to the faculty of Graduate Studies and Research in partial fulfillment of the
requirements for the degree of Doctor of Philosophy

Medical Sciences - Biomedical Engineering

©Qiang Chen
Fall 2009
Edmonton, Alberta

Permission is hereby granted to the University of Alberta Libraries to reproduce single copies of this thesis and to lend or sell such copies for private, scholarly or scientific research purposes only. Where the thesis is converted to, or otherwise made available in digital form, the University of Alberta will advise potential users of the thesis of these terms.

The author reserves all other publication and other rights in association with the copyright in the thesis and, except as herein before provided, neither the thesis nor any substantial portion thereof may be printed or otherwise reproduced in any material form whatsoever without the author's prior written permission.

Examining Committee

Dongyang Li	Chemical and Materials Engineering
Hasan Uludag	Biomedical Engineering
Jack Tuzzynski	Physics
Chong-Qing Ru	Mechanical Engineering
Daolun Chen	Mechanical and Industrial Engineering, Ryerson University

,

Abstract

Key words: Dynein c, microtubule joining, computer simulation, protein motors, self-organization, nano-bio-machines

In this work, a general dynamic model was proposed to simulate the dynamic motion of microtubules driven by dynein motors, which is of importance to the design of potential nano-bio machines composed of dynein motors and microtubules. The model was developed based on Newton's law of motion. By incorporating a DPD technique, the general model was applied to simulate the unidirectional motion of microtubule. The functions of dyneins and their coordination with each other, which plays an important role in the motion of microtubules, were studied. By taking into account the bending energy of microtubules, we extended the general model to study possible mechanisms responsible for the microtubule-microtubule and microtubule-wall interactions, which are essential to the design of optimal track patterns for potential nano-machine systems. This study helps to evaluate the influence of bending and rotation on microtubule joining processes, involving bumping force, bending moment and torque generation. Finally, a phenomenal modeling study based on the Monte Carlo method, was conducted to investigate the self-organization of microtubules driven by dynein motors and identify out key parameters that control the self-organized movement of microtubules, giving crucial information for nano device design.

This modeling study helps to clarify several important issues regarding the interaction between dynein motors and microtubules as a power transfer

medium, which provides important information for the development of potential nanobio-machines using dynein as a biological motor.

Table of Contents

Chapter 1 – Introduction and Literature Review

1.1	An introduction to protein motors.....	2
1.2	The structure of protein motors and cytoskeletons.....	3
1.2.1	The structure of protein motors.....	3
1.2.2	The structure of cytoskeleton filaments.....	8
1.3	Functions of protein motors.....	10
1.3.1	Roles of motor protein in biological systems.....	10
1.3.2	Roles of protein motors in human diseases.....	14
1.3.3	Protein motors – A new power for nano machine design.....	17
1.4	Mechanics of protein motors and cytoskeletons.....	23
1.4.1	The Mechanical force.....	24
1.4.2	The thermal force	33
1.4.3	The chemical forces.....	34
1.5	Computational modeling.....	37
	Reference.....	43

Chapter 2 –A general model for kinetic behaviour of microtubules driven by dynein C

2.1	Introduction.....	56
2.2	A general model for simulating microtubule-motor interactions	57
2.2.1	Construction of protein motor and microtubule systems	57
2.2.2	The driving force from dyneins.....	60

2.2.3	The spring force between adjacent beads.....	64
2.2.4	Bending Force.....	64
2.2.5	Environmental Forces.....	66
2.3	The simulation process.....	66
2.4	Summary.....	67
	Reference.....	68

Chapter 3 - Unidirectional motion of a single microtubule and influences of motors' coordination on driving and drag forces

3.1	Introduction	70
3.2	Model description.....	71
3.2.1	A modified model for unidirectional movement.....	71
3.2.2	The DPD approach.....	72
3.2.3	Modeling Process.....	75
3.3	Results and discussion.....	78
3.3.1	The effect of motor density on the microtubule motility.....	78
3.3.2	The length of microtubule and sliding velocity.....	82
3.3.3	Force analysis.....	84
3.4	Movement of microtubule driven by mixed fast and slow motors.....	90
3.5	Summary.....	93
	Reference.....	96

Chapter 4 – Microtubule-microtubule interactions and microtubule’s collision against micro-fabricated tracks

4.1	Introduction.....	99
4.2	Experimental analysis.....	102
4.2.1	Protein preparation.....	103
4.2.2	Preparation of wall patterns by microfabrication techniques.....	103
4.2.3	In vitro motility assays.....	104
4.2.4	Experimental observation.....	105
4.3	Theoretical study.....	110
4.3.1	Theoretical modeling of the behavior of microtubules.....	110
4.3.2	Simulation process.....	115
4.3.3	Simulation result analysis.....	116
4.4	Quantitative analysis of two joining processes.....	123
4.4.1	The definition of quantitative parameters.....	123
4.4.2	Quantitative bending distance and instant torque analysis.....	126
4.5	Conclusion.....	133
	Reference.....	136

Chapter 5 - Monte Carlo Simulation of self-organization of microtubule driven by dynein C

5.1	Introduction.....	138
5.2	Model description.....	141

5.2.1	Joining probability distribution and microtubule bias.....	142
5.2.1.1	The MT joining probability distribution.....	142
5.2.1.2	The microtubule bias.....	143
5.2.2	Multiple joining.....	147
5.2.3	The simulation process.....	148
5.2.4	The cell list algorithm for computing efficiency.....	151
5.3	Simulation results and analysis.....	152
5.3.1	The influence of microtubule bias on the MT's self-organization.....	152
5.3.2	The influence of microtubule density on MT self-organization.....	155
5.3.3	The influence of joining probability distribution on the MT self- organization.....	157
5.4	Quantitative analysis.....	159
5.4.1	Variations in the MT joining frequency with time.....	159
5.4.2	Influence of MT bias on the joining frequency.....	160
5.4.3	The joining frequency and MT density.....	162
5.5	Conclusion.....	164
	Reference.....	166

Chapter 6 – Conclusion and Future Work

6.1	General summary of the research	168
6.2	The significance of the research.....	170
6.3	Suggested subjects for future work.....	171
	1) Efficiency of protein motors.....	171

2) The joining probability distribution of microtubule joining process	172
3) 3-D model.....	172
4) Electrostatic effect among microtubules and between microtubule and protein motors.....	173
5) Microtubule bias.....	173
6) Extension of the current model for medical problem analysis.....	174

APPENDIX

A. A flow chart of the simulation of the unidirectional movement of microtubule driven by dynein motors.....	176
B. Flow charts of the simulation of microtubule joining driven by dynein motors.....	177
C. A flow chart of Monte Carlo simulation of self-organization of microtubules driven by dynein motors.....	179
D. The derivation of deflection of microtubule during joining.....	180
E. Derivation of bending force of microtubule.....	185

List of Tables

Table 2.1 Examples of forces acting on molecules.....	58
Table 5.1 Three types of joining probability distribution against bumping angle.	158

List of Figures

Fig.1.1	The structure of myosin S1 fragment motor.....	4
Fig.1.2	The Crystal structure of the kinesin dimer.....	6
Fig.1.3	The model of the chlamydomonas outer dynein arm.....	7
Fig.1.4	Schematic structure of dynein (left) and crystal structure of the ATPase domain of AAA protein (right).....	8
Fig.1.5	The lattice structure of the actin filament.....	9
Fig.1.6	The lattice structure of microtubule.....	10
Fig.1.7	The mechanism of muscle contraction (a) the structure of muscle, (b) the Sliding Filament Model of Contraction.....	11
Fig.1.8	Kinesin-superfamily proteins (KIFs) transport various cargoes from the cell body to the synapse in axons.....	12
Fig.1.9	A proposed model for dynein function in cell spindle.....	13
Fig.1.10	Cosegregation of I892F, N890Y, and K1300X point mutations of MYO15 with deafness in three Bengkala nuclear families and two Indian families.....	15
Fig.1.11	Electron micrographs of cross sections through the sperm tail with dynein arms (A) ordinary tail with nine microtubular doublets: each doublet has two dynein arms; (B) the sperm tail of patient, devoid of the dynein arms.....	16
Fig.1.12	Unidirectional rotational movement of microtubules along circular tracks.....	18
Fig.1.13	Schematic illustration of single-molecule technique: (A) Surface	

List of Figures (continued)

assay in which the filament is held by a glass fiber, (B) Bead assay in which the bead is held in an optical trap.....	19
Fig.1.14 Making track on a polytetrafluoroethylene (PTFE)-deposited surface...	20
Fig.1.15 The movement of actin filament along fabricated tracks: a) along polytetra-fluoroethylene (PTFE) linear tracks, (b) along polymethylmethacrylate (PMMA) circle tracks.....	21
Fig.1.16 The rotating crossbridge model for myosin motor.....	26
Fig.1.17 Beginning and end of myosin's working stroke.....	27
Fig.1.18 A powerstroke model ($T=ATP$, $D=ADP$, $D^*=Strained\ ADP$, $P=P_i$).....	28
Fig.1.19 The drag coefficient of the filament under (a) unbounded solution, and (b) near a surface.....	30
Fig.1.20 Bending of a slender rod due to a bending moment.....	31
Fig.1.21 A schematic diagram of the video-enhanced DIC microscope with optical traps.....	33
Fig.1.22 The schedule of two states of molecule under external force.....	35
Fig.1.23 The schedule of the polymerization of filament under external force....	36
Fig.1.24 Schematic of the ATPase cycle involving myosin II and actin filament.	38
Fig.1.25 Hand-over-hand model for conventional kinesin: $D = ADP$, $T = ATP$, $DP = ADP+PI$	39
Fig.2.1 Structure of a microtubule: (a) a three-start helices structure, (b) a polymer chain structure used to model a microtubule.....	57

List of Figures (continued)

Fig.2.2 Forces exerted on a microtubule.....	59
Fig.2.3 The sketch of an attaching and detaching process.....	61
Fig.2.4 An attaching and detaching cycle for dynein c.....	62
Fig.2.5 Sketch of driving region of a dynien motor.....	63
Fig.2.6 A bending microtubule chain.....	65
Fig.3.1 The force system for DPD approach.....	73
Fig.3.2 Related conformational time correlation function against time.....	76
Fig.3.3 Sketch of a model system for unidirectional motion of a microtubule....	77
Fig.3.4 (a) The simulated displacement of a microtubule vs the time (different motor densities were used in the simulation, respectively); (b) Stepwise movement of a microtubule driven by a single dynein c.....	79
Fig.3.5 (a) The velocity of microtubule vs the density of motors; (b) The sliding velocity of microtubule vs the surface density of dynein c.....	81
Fig.3.6 (a) The simulated velocity of microtubule against its length(b) Experimentally observed sliding velocity of a microtubule against its length.....	83
Fig.3.7 F_{driv} , F_{drag} , F_{m_drag} , and F_{s_drag} vs the density of dynein c motors.....	85
Fig.3.8 Average F_{Total} and F_{m_Total} vs the time steps for different motor densities.....	88
Fig.3.9 The forces F_{driv} , F_{drag} , F_{m_drag} , and F_{s_drag} vs the length of microtubule.....	89
Fig.3.10 The velocity of microtubule vs the fraction of Dynein c.....	92

List of Figures (continued)

Fig.3.11 The average force, F_{driv} , F_{drag} , $F_{\text{m_drag}}$, and $F_{\text{s_drag}}$ vs the fraction of dynein c	93
Fig.4.1 Wall-attack patterns microfabricated on a glass surface A. fabrication process with the electron beam lithography. B. fabricated wall-attack-pattern system having three approach angles.....	104
Fig.4.2 Video sequences showing the movement of a microtubule after colliding with another one.....	107
Fig.4.3 Video sequences showing the movement of microtubules after bumping against constraint wall.....	109
Fig.4.4 A microtubule is constructed with a set of beads with a certain mass...	112
Fig.4.5 The viscous force of a microtubule segment.....	113
Fig.4.6 Sketches of two model systems: (a) for modeling microtubule-microtubule joining; (b) for modeling microtubule-wall interaction....	115
Fig.4.7 Microtubule-microtubule and microtubule-wall joining processes with a bumping angle = 45^0 for different microtubule length: (a) length = $8 \mu m$, (b) length = $12 \mu m$, (c) length = $16 \mu m$	117
Fig.4.8 Microtubule-microtubule and microtubule-wall joining processes with microtubule length = $12 \mu m$ for (a) bumping angle = 15^0 , and (b) bumping angle = 45^0	119
Fig.4.9 The bumping processes of microtubule with different length: (a) length = $16 \mu m$, (b) length = $24 \mu m$, and (c) length = $32 \mu m$	121

List of Figures (continued)

Fig.4.10 The bumping processes of microtubule with different bumping angles: (a) bumping angle = 45^0 , (b) bumping angle = 60^0 , and (c) bumping angle = 75^0	122
Fig.4.11 The sketch of microtubule bending.....	124
Fig.4.12 Sketch of a bended microtubule chain.....	125
Fig.4.13 Instant torque against time for two types of joining with microtubule length = $12 \mu m$ and bumping angle = 45^0	128
Fig.4.14 Bending distance against time for two joining processes with bumping angle = 45^0 and microtubule length = 8, 12, $16 \mu m$, respectively.....	129
Fig.4.15 A spring model for microtubule-motor system.....	130
Fig.4.16 Sketch of bending of rod.....	131
Fig.4.17 Bumping force against time for microtubule-microtubule and microtubule-wall joining with a bumping angle = 45^0 and a microtubule length = $12 \mu m$	132
Fig.5.1 Circular pattern of microtubules driven by dynein motors.....	141
Fig.5.2 Probability distributions of different joining events. a: anti-parallel joining, c: crossing, j: parallel joining, s: stopping.....	143
Fig.5.3 A nominal microtubule bias definition (a) Experimentally observed bias distribution of microtubule in solution (b) sketch of bias definition...	144
Fig.5.4 Different MT joining processes influenced by the microtubule bias under different joining condition (a) parallel joining;	

List of Figures (continued)

(b) anti-parallel joining.....	146
Fig.5.5 A multiple joining process.....	147
Fig.5.6 Joining condition of two microtubules.....	149
Fig.5.7 A cell list system.....	152
Fig.5.8 Simulated pattern formation from an initial state (a) initial state, (b) bias rate = 0, (c) bias rate = 0.006, (d) bias rate = 0.024, (e) bias rate = 0.048, (f) bias rate = 0.096.....	154
Fig.5.9 Self-organization process of microtubules with density = 10000/10000 μm^2 and bias rate = 0.024. (a) Initial state; (b) after 2000 steps; (c) after 4000 steps; and (d) after 8000 steps.....	155
Fig.5.10 Self-organization processes with different microtubule densities. (A) Density = 2500/10000 μm^2 ; (B) Density = 225000/10000 μm^2 ...	157
Fig.5.11 Self-organized patterns of microtubules with different joining probability distributions: (a) low, (b) middle, and (c) high.....	158
Fig.5.12 Joining frequency against time. Microtubule density = 10000/10000 μm^2 and bias rate = 0.024.....	160
Fig.5.13 The joining frequency against time with different microtubule bias: (a) bias rate = 0; (b) bias rate = 0.006; (c) bias rate = 0.048. (b) (Microtubule density = 2500/ μm^2).....	162
Fig.5.14 Joining frequency against time with different microtubule density: (a) density = 2500/10000 μm^2 ; (b) density = 22500/10000 μm^2	163
Fig.A.1 A flow chart of the simulation of the unidirectional movement of	

List of Figures (continued)

	microtubule driven by dynein motors.....	176
Fig.B.1	A flow chart of the simulation of microtubule-microtubule joining driven by dynein motors.....	177
Fig.B.2	A flow chart of the simulation of MT-Wall joining driven by dynein motors.....	178
Fig.C.1	A flow chart of Monte Carlo simulation of self-organization of microtubules driven by dynein motors.....	179
Fig.D.1	Sketch of beam deflection under a single load.....	180
Fig.D.2	Sketch of bending of rod.....	183
Fig.E.1	A bending microtubule chain.....	185

List of Symbols

ATP	adenosine triphosphate	(1.1)
ADP	adenosine diphosphate	(1.4)
F_d	drag force	(1. 4. 1)
γ	drag coefficient	(1. 4. 1)
V	velocity of the filament	(1. 4. 1)
I	shape moment of inertia of the cross-section	(1. 4. 1)
M	bending moment of the filament	(1. 4. 1)
R	curvature of the bent filament	(1. 4. 1)
U	average thermal energy	(1. 4. 2)
k	spring constant of microtubule	(1. 4. 2)
T	temperature	(1. 4. 2)
x	position	(1. 4. 2)
$C(x, t)$	concentration at position x and time t	(1. 4. 2)
D	diffusion coefficient	(1. 4. 2)
ΔG	difference in free energy	(1. 4. 3)
ΔG^0	corresponding change in the free energy relative to the state in the absence of tension	(1. 4. 3)
F	tension across the molecule due to the conformational change	(1. 4. 3)
Δx	length of molecule changes	(1. 4. 3)
F_{eq}	equilibrium force	(1. 4. 3)
K_c	critical concentration in the absence of external force.	(1. 4. 3)
$[A_1]$	monomer concentration	(1. 4. 3)
δ	increase in length due to the incorporation of one monomer	(1. 4. 3)
M_A	bending moment resulting from actively generated forces	(1. 5)
M_E	bending moment resulting from elastic bending resistance of the microtubule	(1. 5)
M_V	bending moment resulting from the viscous resistances of the surrounding medium	(1. 5)
m_i	mass of the bead i	(1. 5)
V_i	velocity of the bead i	(1. 5)
F_{iT}	a tension force associated with the resistance	(1. 5)

	of the filament to stretching	
\mathbf{F}_{iA}	an active bending force generated by the organism to induce movement	(1. 5)
\mathbf{F}_N	a viscous force exerted by the fluid on the filament	(1. 5)
\mathbf{F}_{iS}	a spring force between adjacent microtubule beads	(2. 2. 1)
\mathbf{F}_{iD}	a driving force generated by dynein	(2. 2. 1)
\mathbf{F}_{iB}	a bending force associated with filament bending	(2. 2. 1)
\mathbf{F}_{io}	a force from environment	(2. 2. 1)
α, β	subunits of microtubule	(2.2.2)
τ_{on}	total attachment period for motor protein	(2. 2. 2)
τ_{driv}	total driving period for motor protein	(2. 2. 2)
τ_{drag}	total drag period for motor protein	(2. 2. 2)
τ_{off}	total off-attach period for motor protein	(2. 2. 2)
k_d	spring constant of the molecular motor	(2. 2. 2)
$\Delta\delta_j$	stroke distance of dynein j	(2. 2. 2)
r_{ij}	spring length between adjacent beads	(2. 2. 3)
r_{eq}	stress-free spring length	(2. 2. 3)
L	length of microtubule	(2. 2. 3)
G	bending constant of microtubule	(2. 2. 4)
E	Young's modulus of microtubule	(2. 2. 4)
\vec{r}_i	vector represent microtubule segment i	(2. 2. 4)
$\vec{r}_i(t)$	positions of particle i at time t	(2. 3)
$V_i(t)$	velocity of the particle at time t	(2. 3)
$f_i(t)$	total forces on the particle at time t	(2. 3)
r_c	a cutoff radius	(3. 2. 2)

a_{AA}	particle A-particle A interaction coefficient	(3. 2. 2)
a_{AB}	particle A-particle B interaction coefficient	(3. 2. 2)
a_{ij}	repulsion coefficient	(3. 2. 2)
ξ	a friction coefficient	(3. 2. 2)
σ	amplitude of noise	(3. 2. 2)
ζ_{ij}	a random noise term with zero mean and unit variance	(3. 2. 2)
ρ	number density	(3. 2. 3)
λ	scale factor to maintain a constant system temperature	(3. 2. 3)
T_c	current kinetic temperature	(3. 2. 3)
t_T	present time constant	(3. 2. 3)
$C(t)$	a related conformational time correlation function	(3. 2. 3)
R_g^2	mean-square radius of gyration	(3. 2. 3)
$r_i(0), r_i(t)$	the original position and position in time t for bead i respectively	(3. 2. 3)
$R_{cm}(0)$	original center-of-mass of the chain and the	(3. 2. 3)
$R_{cm}(t)$	center-of-mass at time t.	
V_s	simulated microtubule velocity	(3. 3. 1)
V_{exp}	experimental microtubule velocity	(3. 3. 1)
F_{driv}	total driving force	(3. 3. 3)
F_{drag}	total drag force	(3. 3. 3)
F_{m_drag}	drag force from motor	(3. 3. 3)
F_{s_drag}	drag force from solution	(3. 3. 3)
F_{total}	total force on microtubule	(3. 3. 3)
F_{m_total}	total force from motor on microtubule	(3. 3. 3)
F_{iV}	a viscous force exerted by the fluid on the ith bead	(4. 3. 1)
F_{iM}	a collision force between two collided microtubule beads	(4. 3. 1)
F_{iL}, F_{iV}	viscous forces parallel and perpendicular to segment i respectively	(4. 3. 1)

C_{iL}, C_{iV}	parallel and perpendicular drag coefficients	(4. 3. 1)
V_{iL}, V_{iV}	velocity of segment i in parallel and vertical directions	(4. 3. 1)
h	vertical distance of the center of cylinder to the glass surface	(4. 3. 1)
r	radius of cross-section of cylinder	(4. 3. 1)
η	viscous coefficient of cylinder in solution	(4. 3. 1)
F_{iVX}, F_{iVY}	forces in x and y directions generated by viscous forces	(4. 3. 1)
β	collision coefficient	(4. 3. 1)
r_d	equilibrium distance without force	(4. 3. 1)
$F_{i,J,M}$	collision force from bead J on bead i another microtubule	(4. 3. 1)
X_c, Y_c	The mass center of the microtubule	(4. 4. 1)
Q	total instant torque	(4. 4. 1)
F_{iX}, F_{iY}	total force in x and y directions	(4. 4. 1)
v	rod deformation	(4. 4. 2)
θ_A	deformation angle of rod	(4. 4. 2)
$\Delta\theta$	angle change	(5. 2. 1. 2)
R	bias radius of microtubule	(5. 2. 1. 2)
r_θ	A bias rate is defined as the angle change per unit time	(5. 2. 1. 2)
$P(i, j, t)$	joining probability of microtubules i and j at time t	(5. 2. 3)
$P(\theta)$	joining probability with special bumping angle	(5. 2. 3)
$\theta(i, j, t)$	angle of two microtubule i and j at time t	(5. 2. 3)
$\delta(i, j, t)$	a indicator function to indicate the joining condition	(5. 2. 3)
$R(i, j, t)$	a uniformly distributed random number between 0 and 1	(5. 2. 3)
$\Delta\theta(i, t)$	the change in the moving direction of microtubule i at time t	(5. 2. 3)
$\Delta r(i, t)$	change in the bias rate	(5. 2. 3)

Chapter 1

Introduction and Literature Review

1.1 An introduction to protein motors

Motor proteins, such as myosin, kinesin, and dynein, are protein-based superamolecular conjugates, which have specific functions of converting the chemical energy from adenosine triphosphate (ATP) hydrolysis into mechanical energy, which is used to power cellular motility [1]. These motors are called molecular machines, which play essential roles in a wide variety of biological events or progresses related to the activities of cells, e.g., muscle contraction [2], axonal transport [3, 4], formation of spindle apparatus, and separation of chromosomes during mitosis and meiosis [5]. Defective motor proteins are responsible for many diseases when they fail to fulfill their functions. For example, kinesin deficiencies cause Charcot-Marie-Tooth disease [6] and some kidney diseases [7]. Dynein deficiencies can lead to chronic infections of the respiratory tract as cilia fails to function without dynein [8]. Defects in muscular myosin predictably cause myopathies [9].

In recent years, motor proteins have been extensively studied due to their potential to be used at the molecular scale for nano-bio-mechanical systems or devices [10-13]. By fabricating tracks on a surface in which motor proteins are immobilized, the motion of cytoskeleton filaments can be confined by the tracks and thus guided to move along desired directions or patterns [14-20]. The tracks are channels bordered by walls of a material that is coated on a glass surface, within which microtubules rarely climb up the walls, so that the microtubules can move only along the designed tracks. The success in controlling the moving

direction of microtubules using surface tracks has shortened the distance between the concept and reality for nanobiomachine development.

In order to better understand the interaction between cytoskeleton filaments and motor proteins for control of relevant biomedical processes as well as to develop molecular machines or nanobiomechanical systems using bio-filaments as the power transfer medium and motor proteins as biological engines, it is essential to understand the structures and functions of these molecular motors and cytoskeleton filaments, and the interaction between molecular motors and cytoskeleton filaments.

1.2 The structure of motor proteins and cytoskeletons

1.2.1 The structure of motor proteins

1.2.1.1 Myosin motors

Myosins are molecular motors that use the energy from adenosine triphosphate (ATP) hydrolysis to generate force to drive actin filaments. The motors are bound to actin filament to form actomyosins and walk unidirectionally along the filament [21, 22]. Myosin has one or two heavy chains (HCs) with a molecular mass of about 200kDa, and 1~6 light chains (LCs) with a molecular mass of about 20kDa. The light chains wrap around the neck region of the heavy chain just like a necklace. Based on functions of heavy chains, they can be divided into three domains. The relatively conserved N-terminal motor or head

domain has binding sites for both ATP and the actin filament. The second domain includes a tail, which positions the motor domains properly so that they can interact with actin filaments. The third domain joining the head and neck, which is called the converter domain, is responsible for producing the force required for movement. Fig.1.1 illustrates the structure of a myosin S1 fragment motor [23]. The greatest revelation of the myosin structure is that the head contains a large subdomain that might function as a molecular lever. The domain consisting of an 8-nm-long α -helix is wrapped with two calmodulin-like light chains. It extends from near the nucleotide-binding pocket to the distal end of the head to amplify small movement in the nucleotide-binding pocket into large nanometer-sized motion of the myosin tail.

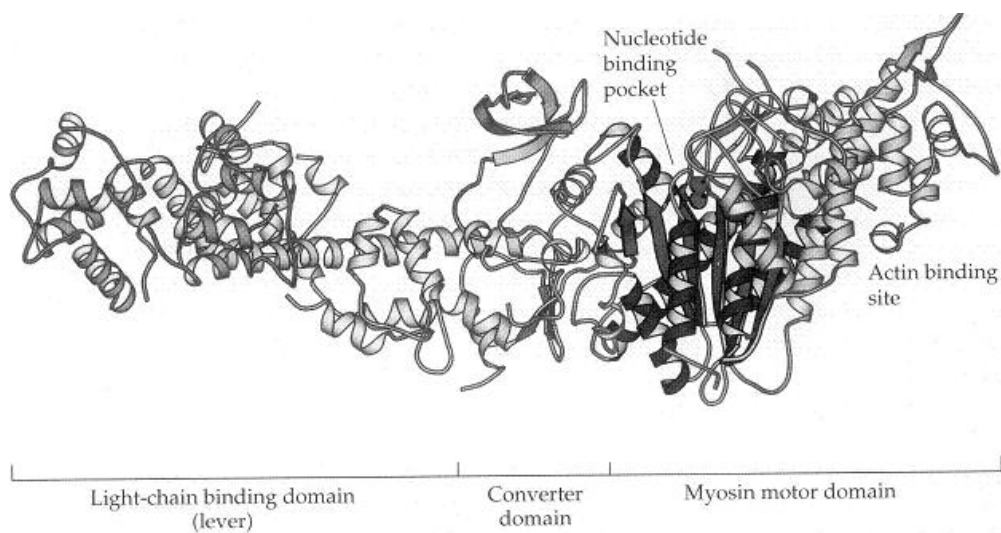


Fig.1.1 The structure of myosin S1 fragment motor [23]

1.2.1.2 Kinesin motors

Kinesins are molecular motors that direct the movement of microtubules by consuming the energy from ATP hydrolysis. They are involved in the intracellular transport of organelles, proteins, protein complexes, mRNA, and chromosomal, and spindle movements during mitosis and meiosis [24].

Kinesins are classified into three majors: N-terminal, middle motor domain, and C-terminal kinesins, defined by the topology of the motor domain. Conventional kinesin and kinesin heavy chain both belong to the N-1 class and have been extensively studied. Conventional kinesin consists of two 80nm-long heavy chains (about 120 kDa), which are connected at their C-termini to two light chains (about 64 kDa). Each heavy chain has a rod-like structure composed of two globular heads, a stalk, and fanlike ends, as Fig.1.2 illustrates [25, 26]. Different from myosin, kinesin lacks a light-chain binding domain. However, it is thought that kinesin undergoes a conformational change of 8nm as it steps along the microtubule. It is possible that kinesin's second head acts as a lever arm that amplifies smaller motions of the first head.

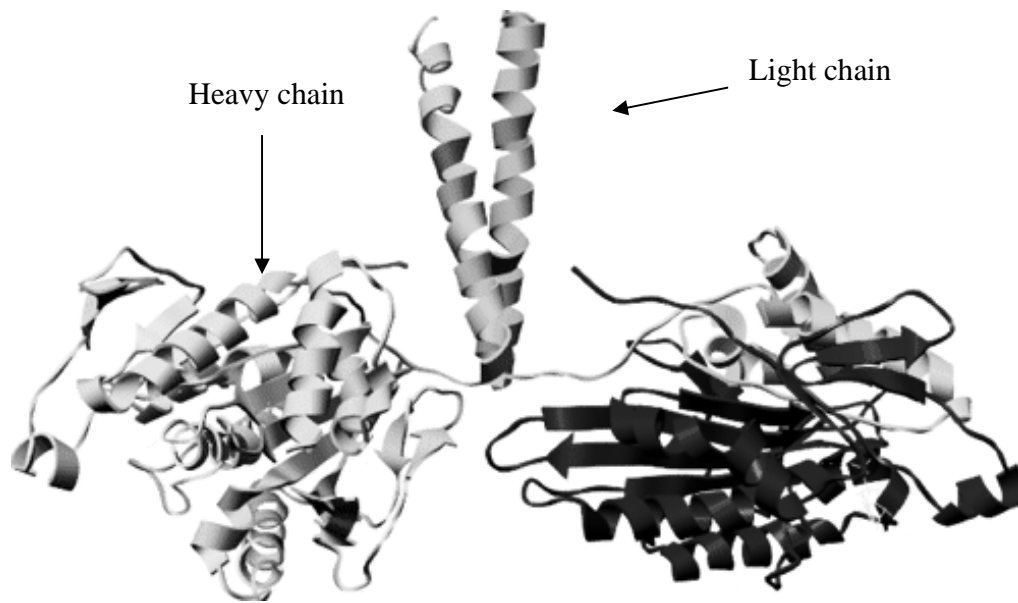


Fig.1.2 The crystal structure of the kinesin dimer^[25]

1.2.1.3 Dynein motors

Dyneins are multicomponent complexes, which participate in a wide range of fundamental cellular processes, such as mitosis, vesicular transport, and the assembly and motility of cilia and flagella [27].

In general, dyneins have very high molecular weights, and their structures have not been well established yet. Similar to kinesin and myosin, all dyneins are built around one or three heavy chains motor units (HCs, about 520 kDa, which are 10 times as large as those of conventional kinesin), which contain the ATPase and motor activities. Defined by the number of HCs and various HC-associated polypeptides, the dyneins can be divided into two major classes. The first class

includes cytoplasmic dynein, outer arm dynein, and the II type of inner arm dynein. These types of dyneins contain two or three heavy chains, at least two intermediate chains (ICs), and a series of light chains (LCs). Fig.1.3 illustrates a model of the Chlamydomonas outer dynein arm [28]. In the model, a series of ICs interact directly with the HCs and be involved in the regulation of motor activity.

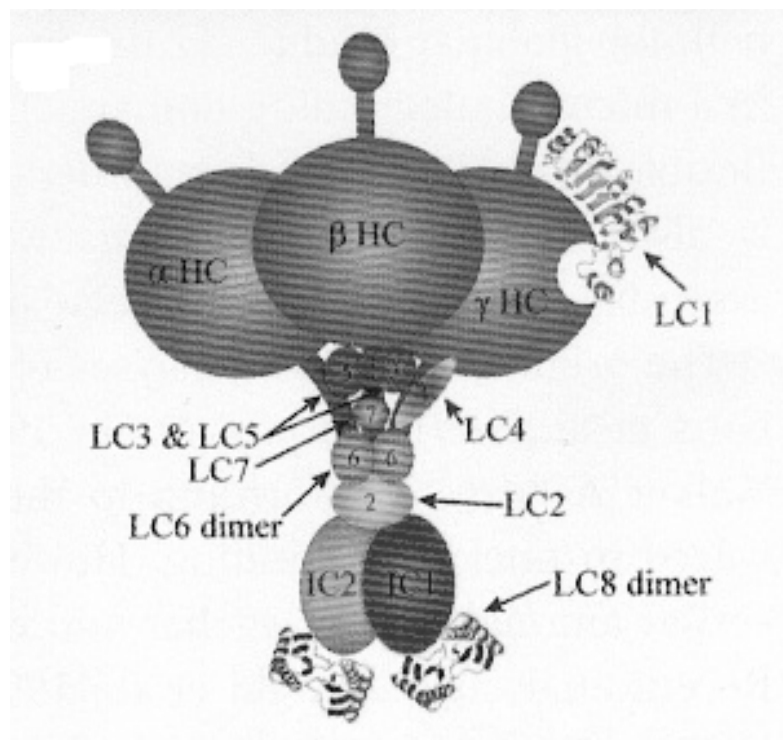


Fig.1.3 A model of the chlamydomonas outer dynein arm ^[28]

Different from kinesin and myosin, dynein motor domain is a member of the AAA+ class of ATPases [29, 30]. In dyneins, the six ATPase units are integrated in a single polypeptide chain to form a ring. There are two additional domains projecting out of the hexameric ring, which play an essential role in the motion function. One is called a stalk, which is 15 nm long and carries an ATP

sensitive microtubule-binding site at its tip. Another is called a stem, which is larger and connects to the N-terminal region of the hexameric ring of dynein. It is used for docking with a cargo. Fig.1.4 shows the structure of dynein (left) and crystal structure of the hexameric ring [30].

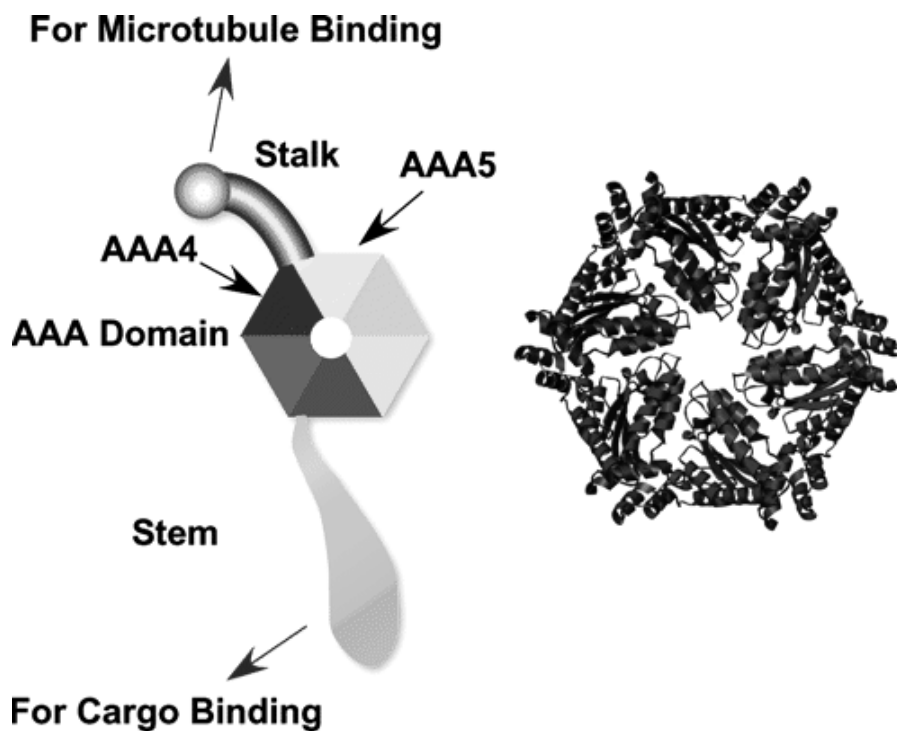


Fig.1.4 Schematic structure of dynein (left) and crystal structure of the ATPase domain of AAA protein (right) [30]

1.2.2 The structure of cytoskeleton filaments

1.2.2.1 Actin filament

Fig.1.5 illustrates the lattice structure of the actin filament [31]. An actin filament is a one-start, left-hand, double helical supramolecular polymer of actin

monomers (globular actin). The full period of the filament is 72 nm, which contains 26 actin monomers that make 12 turns. The rise is 2.77nm per subunit and rotation per monomer is 166 degree [32]. The actin monomers are asymmetrical, which leads to a polar structure of an actin filament. Due to this polar structural difference, the polymerization at one end is faster than the other. The fast-growing end is called a plus-end while the slow-growing end is called a minus-end. This polarity is the main reason for the unidirectional guide of motor proteins.

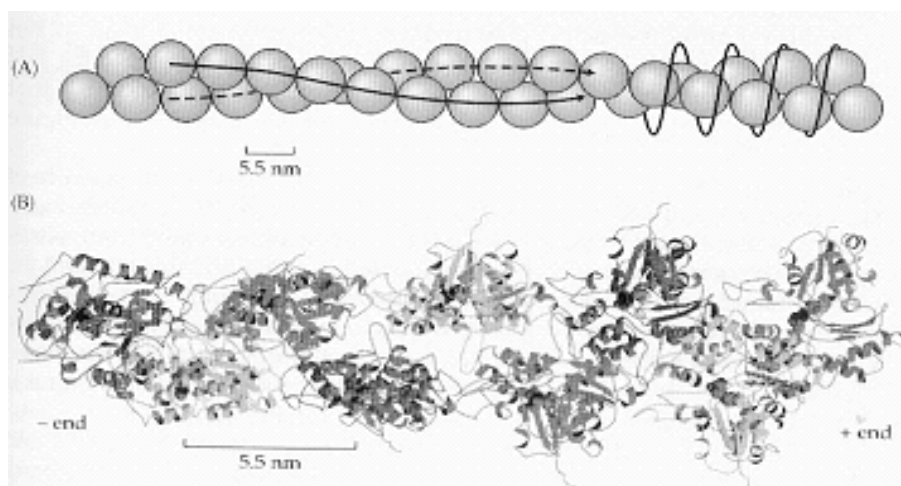


Fig.1.5 The lattice structure of the actin filament ^[31]

1.2.2.2 Microtubules

Fig.1.6 illustrates the lattice structure of the microtubule determined by electron microscopy [33]. The microtubule is composed of tubulin monomers. The building blocks, $\alpha\beta$ tubulin heterodimers, are the subunits of microtubule. As Fig.1.6 shows, the dimers are connected head-to-tail to form a protofilament.

The protofilaments are then connected laterally to form a cylindrical tube. The protofilaments run parallel to the axis of the microtubule, generating a three-start helical structure. Most of microtubules have 3 starts and 13 protofilaments. There is a small offset, $\sim 0.92\text{nm}$, between dimers of neighboring protofilaments, which accumulates a total offset equal to the length of three monomers, 12nm , after 13 protofilaments. Same as the actin monomer, the dimer is also asymmetric. Since the dimers associate head to tail and all the protofilaments are parallel, the microtubule is polar, which allows kinesins or dyneins to move unidirectionally using their motor domain attached to the microtubules [34].

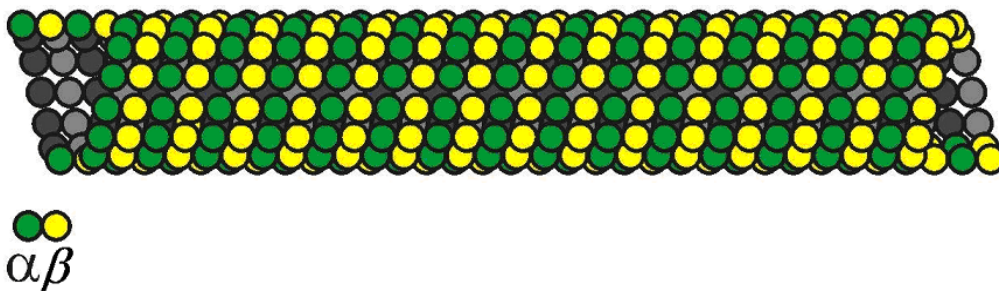


Fig.1.6 The lattice structure of microtubule ^[33]

1.3 Functions of motor proteins

1.3.1 Roles of motor protein in biological system

Myosin is an important muscle protein which "causes" the contraction of muscle fibers in animals and human beings. The sliding of filaments in muscle

fibers is the result of interactions between the myosin cross-bridges and thin (actin) filaments. The cross-bridges reversibly bind to actin and produce a mechanical impulse, resulting in force transmission along the filaments, which results in either force production at the tendons, or shortening, as Fig.1.7 illustrates [35].

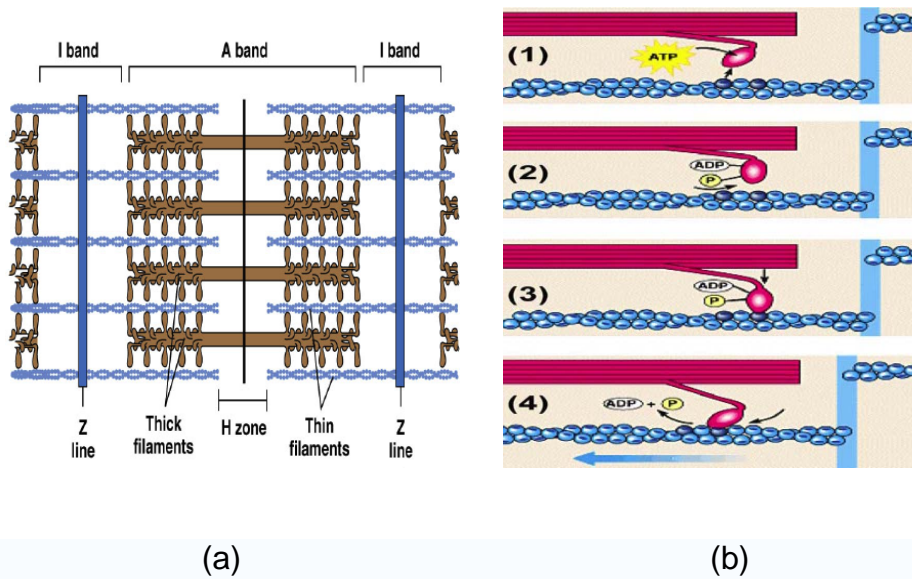


Fig.1.7 The mechanism of muscle contraction (a) the structure of muscle, (b) the Sliding Filament Model of Contraction [35]

Kinesins drive the transport of a wide variety of organelles and vesicular cargoes, including endoplasmic reticulum (ER), Golgi, endosomes, lysosomes, mitochondria and transport vesicles. The movement of these vesicles requires the action of molecular motor proteins that bind cargo vesicles and generate directed movement coupled to ATP hydrolysis along polarized microtubules or microfilaments. Fig.1.8 illustrates how kinesin transports “cargos” along

microtubules in neurons [36]. In axons, the microtubules are oriented in a longitudinal array. They are unipolar, and the plus-end points distally. However, in the proximal region of dendrites, microtubules have mixed polarity. Most proteins needed in axons and synapses have to be synthesized in cell bodies and are then transported along the axon. In axons, kinesin-superfamily proteins (KIFs) transport various cargoes from the cell body to the synapse.

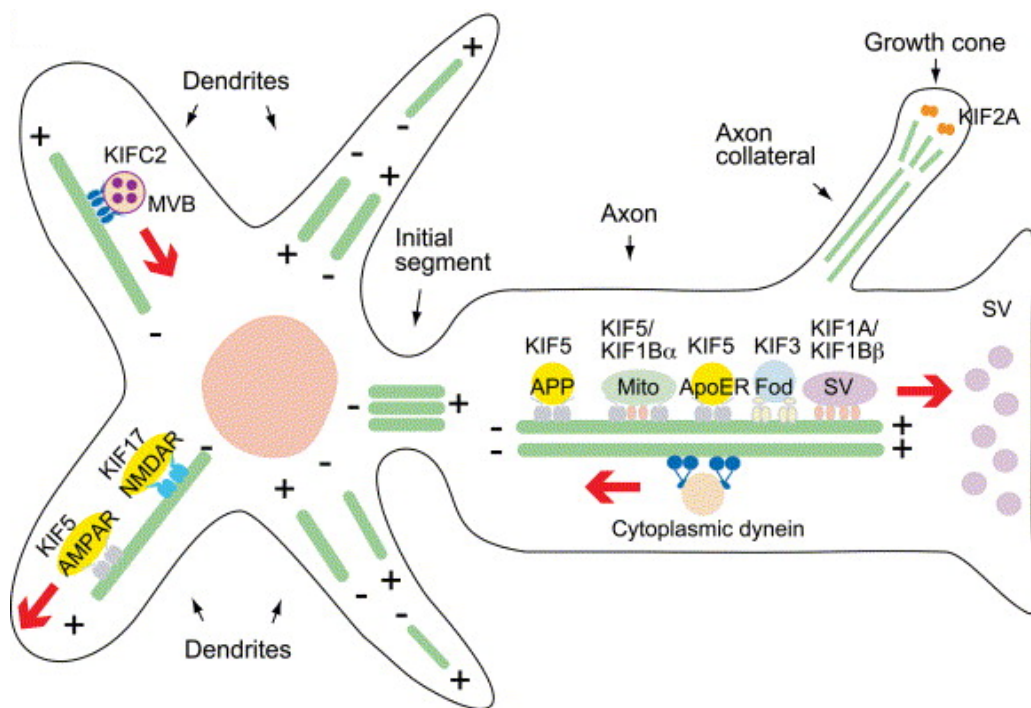


Fig.1.8 Kinesin-superfamily proteins (KIFs) transport various cargoes from the cell body to the synapse in axons [36]

Dyneins can be divided into two groups: cytoplasmic dyneins and axonemal dyneins. Axonemal dynein is the first discovered microtubule motor protein, which functions as a molecular engine for the movement of cilia and

flagella [37]. Dynein is responsible for the beating movement of cilia and sperm flagella, and is found only in cells with those structures. Cytoplasmic dynein, found in all animal cells and possibly plant cells as well, performs functions necessary for cell survival such as organelle transport and centrosome assembly in the cell. Dynein probably helps to position the Golgi complex and other organelles; it also helps transport cargo needed for cell functioning, such as vesicles made by the endoplasmic reticulum, endosomes, and lysosomes [38]. Dynein may be involved in the movement of chromosomes and positioning the mitotic spindles for cell division [39]. Fig.1.9 illustrates a model for dynein function in cell spindle. In the absence of dynein activity, poles are loose and splayed. By cross-linking microtubules and moving toward their minus ends, dynein functions to focus spindle poles. Dynein also carries organelles and microtubule fragments along the axons of neurons in a process called axoplasmic transport [40].

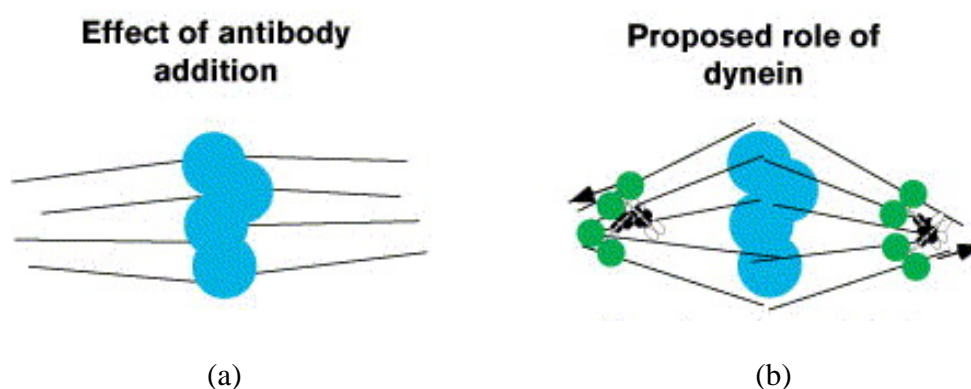


Fig.1.9 A proposed model for dynein function in a cell spindle

1.3.2 Roles of motor proteins in human diseases

Motor proteins also play a very important role in some processes related to diseases. The importance of motor proteins in cells becomes evident when they fail to fulfill their functions. Hypertrophic cardiomyopathy is characterized by robust thickening of left ventricular muscle due to enlargement of individual myocytes with disorganized fibers. Mutations in the gene encoding cardiac β -myosin heavy chains considerably contribute to the cause of the disease [41]. Myosins play a very important role in signal transduction. Myosin XV is linked to human nonsyndromic deafness, DFNB3, which displays severe inner-ear dysfunction involving both auditory and vestibular functions [42, 43]. Fig.1.10 illustrates point mutations of MYO15 with deafness in three Bengkala nuclear families and two Indian families [43]. A myosin VIIA defect results in a disorganized array of stereocilia and is responsible for human Usher syndrome IB and the corresponding mouse model shaker-1[44, 45]. In lacking myosin VIIA, the resting tension is absent, requiring non-physiologically large bundle deflections to open. Myosin VI is linked to human DFNA22 and mouse Snell's Waltzer deafness [46].

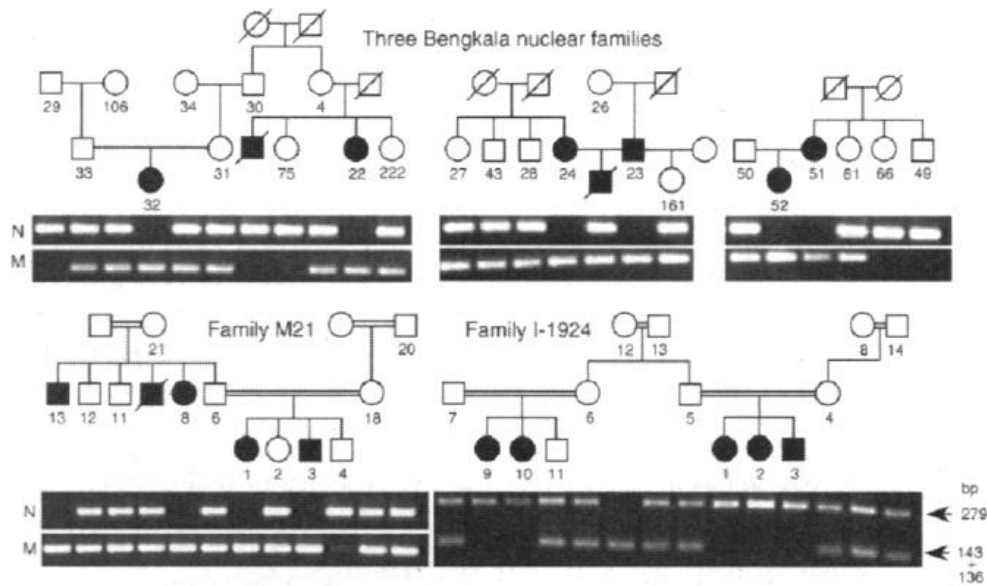


Fig.1.10 Cosegregation of I892F, N890Y, and K1300X point mutations of MYO15 with deafness in three Bengkala nuclear families and two Indian families [43]

In nerve axons, most proteins that are vital for the maintenance and function in the axon and synaptic regions need to be transported down the axon since protein synthetic machineries are absent. Kinesin plays an important role in transporting synaptic vesicle precursors in the axon from the cell body to the synapse. Zhao et al [6] reported that a mutation of KIF1Bb was the cause of Charcot-Marie-Tooth disease type 2A. CMT2A patients contain a loss-of-function mutation in the motor domain of the KIF1B gene, which indicates that defects in axonal transport due to a mutated motor protein could underlie human peripheral neuropathy. Reid, E. et al's [47] research demonstrated that KIF5 had been linked to the hereditary spastic paraplasia (SPG10) locus. Hereditary spastic paraplegias are a genetically heterogeneous group of nondegenerative disorders

that are characterized by progressive lower-limb spasticity and weakness. The gene encoding KIF5A is found in the SPG10 locus, and a mis-sense mutation in this gene has been identified in all affected members of the family.

Immotile cilia syndrome (primary ciliary dyskinesia) is a disorder characterized by a defect in the motility of cilia. Due to a structure defect, e.g., lacking dynein arms, mutational cilia and flagella may cause the Kartagener's syndrome, a chronic disease that occurs when cilia are unable to move [8, 48]. Fig.1.11 illustrates electron micrographs of cross sections through the sperm tail. Dynein protein is also responsible for some diseases related to roles in cell division or nucleokinesis. Recently, researchers have found that the interaction between cytoplasmic dynein and LIS1 might cause neuronal migration defects either by affecting cell division, which is crucial for determining the final destination of a cortical neuron, or by affecting the extension of leading processes and/or nucleokinesis [49, 50].

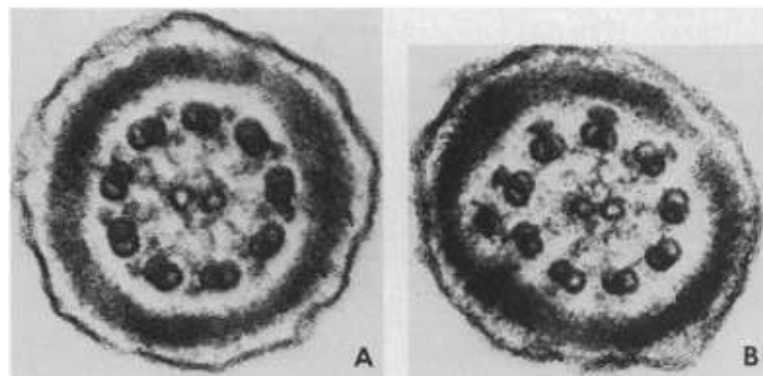


Fig.1.11 Electron micrographs of cross sections through the sperm tail with dynein arms (A) ordinary tail with nine microtubular doublets: each doublet has two dynein arms; (B) the sperm tail of patient, devoid of the dynein arms ^[8]

1.3.3 Motor proteins – A new power for nano machine design

In recent years, molecular motors have attracted wide interest and became one of the most exciting areas in nanotechnology since they are promising candidates for future nanobio machines. These molecular motors can move objects thousands of times as heavy as their own weight and transport specific cargos under controllable conditions. It was noticed that a molecular motor was able to attach to DNA at a specific location and then trans-locate the rest of the DNA molecule through the bound complex. Therefore, the motor acts as a nano-actuator and is able to move objects attached to the end of the DNA toward the bound motor. This ability may be used to link biological systems to silicon-based nanodevices [51]. Molecular motors transport intracellular cargo along actin filaments or microtubules, and provide a force to drive potential nano- and micro-bio-machines. To use the biological motors for microscale transport, the most common approach is to move filaments along surfaces functionalized with motor proteins. The filaments then become potential transport vehicles for sensors and lab-on-a-chip applications. Fig.1.12 illustrates controlled motility of bio motor-driven microtubules using a designed surface track pattern [52].

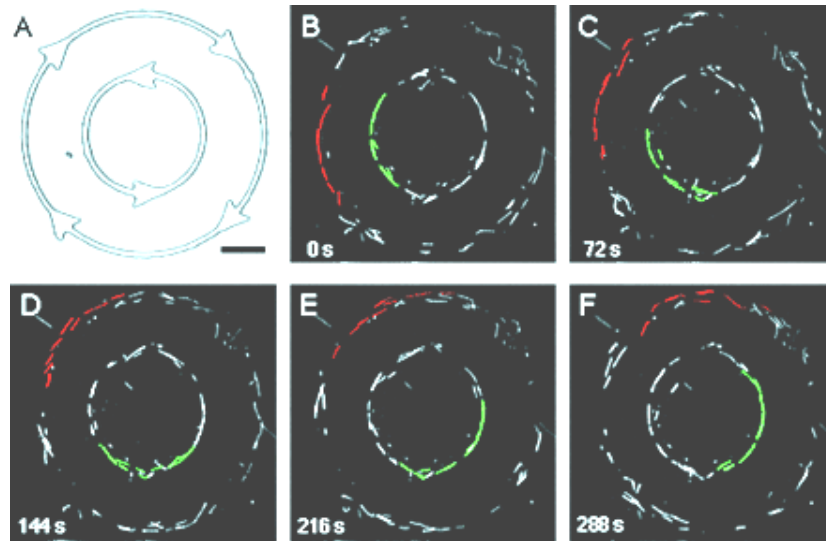


Fig.1.12 Unidirectional rotational movement of microtubules along circular tracks[52]

Studies of motor proteins were revolutionized by the development of *in vitro* motility assays. In such assays, the motility of purified motor proteins along purified cytoskeletal filaments (actin or microtubules) or of the filaments moving on protein-motor coated surfaces is reconstituted in cell-free conditions [53]. In 1985, a first completely reproduced assay was performed by Spudich, in which motor-coated beads were shown to move along oriented filaments made from purified actin that had been bound to the surface of a microscope slide [54]. Assays have been now extended to the single-molecule level and permit determination of dynamic properties, which cannot be studied by macroscopic ensemble-averaged measurements. The chemo-mechanical energy transduction processes in motor proteins are now being revealed by these technical developments.

In *in vitro* assays, there are two typical geometries: bead assays and surface assays. Fig.1.13 illustrates these two methods [55]. In the former, actin filament or microtubule is fixed to a substrate, such as a microscope slide, and motors are attached to small plastic beads of typical diameter 1 μm or to the tip of a fine glass needle. The motion of the beads or of the needle along the filaments in the presence of ATP is visualized using a light microscope. Position and movement of the beads or the needle are measured

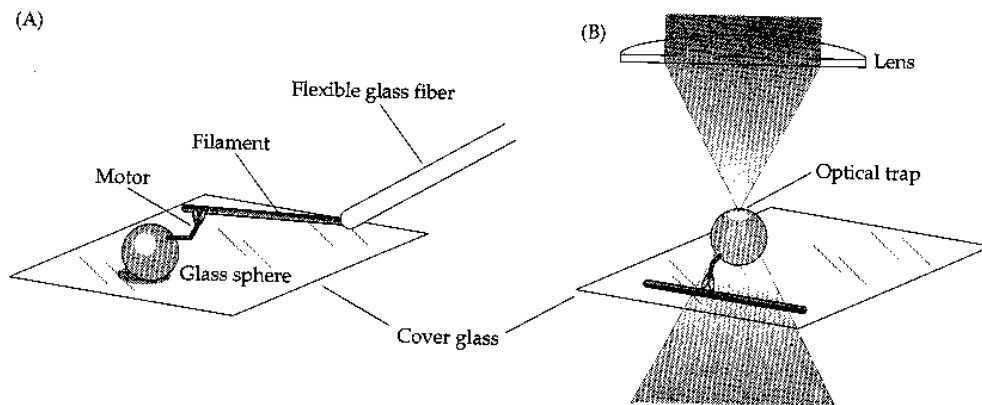


Fig.1.13 Schematic illustration of single-molecule technique: (A) Surface assay in which the filament is held by a glass fiber, (B) Bead assay in which the bead is held in an optical trap^[55]

photoelectrically and can be determined with a resolution on the order of nanometers with sub-millisecond time-response. In the surface assay, the motors themselves are fixed to the substrate. A filament is held in a force transducer. The filament is observed to diffuse down from solution and then be attached to and

glide over the motor-coated surface. Visualization of the filaments is readily accomplished using dark-field or fluorescence microscopy.

In vitro assay methods provide powerful tools for the development of nanometer devices using motor proteins. The general method of using motor machines for nanometer scale devices is conceptually simple. The motor proteins are deposited on a specific polymer surface and are aligned to form special tracks. The fabricated tracks will guide the movement of cytoskeleton filaments. This directed motion could be used for nano-devices. Fig.1.14 illustrates how to make tracks on polytetrafluoroethylene (PTFE)-deposited surfaces [56], in which motor proteins are aligned to drive filaments to move along the tracks. The PTFE thin films consist of many linear and parallel PTFE ridges, 10-100 nm wide, on the coverslip surface. Myosins are adsorbed on the ridges without losing activity; the actin filaments were observed moving on the ridges. Fig.1.15 shows the movement of actin filaments that is restricted to the well-defined fabricated tracks [57].

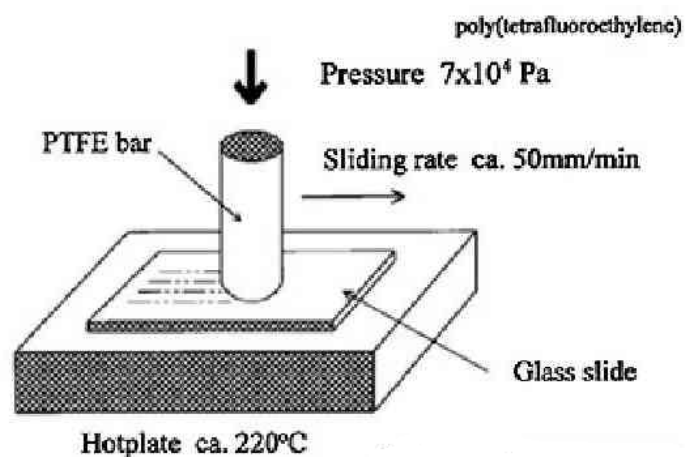


Fig.1.14 Making tracks on a polytetrafluoroethylene (PTFE)-deposited surface [56]

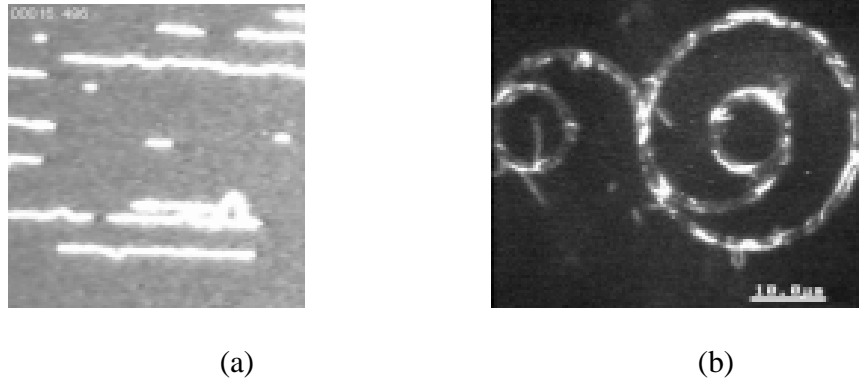


Fig.1.15 The movement of actin filaments along fabricated tracks: a) along polytetra-fluoroethylene (PTFE) linear tracks, (b) along polymethylmethacrylate (PMMA) circle tracks [57]

A lot of efforts have recently been made to advance this specific function of motor proteins. Suzuki and co-workers [17] reported directional motion of actin filaments driven by aligned and immobilized myosin molecules using microlithographically-patterned resist polymers. In the presence of detergent, kinesin can be selectively attached onto a glass surface, from which the photo-resist polymer has been removed, rather than on the photo-resist polymer itself [58]. The tracks are channels bordered by walls of the resist material, within which microtubules rarely climb up the walls, so that the microtubules can move only along the designed tracks. Controlled movement of microtubules along tracks can also be achieved using micrometer-scaled grooves fabricated lithographically on glass surfaces [19, 20]. Among different motor proteins,

dynein has attracted increasing interest due to the fact that it moves 10 times faster than kinesin [59]. Dynein is capable of moving cytoskeletal filaments, microtubules at a velocity of 10-20 $\mu\text{m/s}$, which makes dynein the fastest motor among microtubule motors reported so far. Such ability would render dynein the most promising motor protein for nano-bio-devices. By fabricating designed pattern tracks on NEB-22 deposited on a glass surface, Oiwa and his colleagues [60] immobilized subspecies of axonemal dyneins on the tracks to guide microtubules to move along specific trajectories; Changing the geometry of the track wall, they also successfully rectified random movement of microtubules into unidirectional movement. By designing track patterns of motor proteins with restricted walls on a well-defined surface, the motion of bio motor-driven cytoskeleton filaments could be arranged in defined directions or patterns. These efforts largely shorten the distance between the concept and reality for nanobiomachine development.

In order to drive a cytoskeleton filament, motor proteins must bind to the filament, hydrolyze ATP and then convert released chemical energy to mechanical energy, thus driving the filament to move. Understanding the mechanism responsible for this energy conversion and driving process is of importance to utilization of motor proteins in future molecular machines. Considerable experimental efforts have been made to investigate relevant issues, including the structure of motor proteins [61-63], elastic behavior of motors and cytoskeletal filaments [64-67], and the motility of motor proteins [68, 69], etc. In addition, the rapid progress in the development of advanced experimental

techniques, such as atomic force microscopy [70], optical trap nanometry [71] and fluorescence microscopy [72], has provided researchers effective tools to investigate the dynamics of single-molecule in situ with spatial and temporal resolutions down to Å and μs ranges, respectively. This allows direct observation of dynamic processes involving motor proteins, for which macroscopic ensemble-averaged measurements do not work. Two fundamental motor-protein parameters, coupling efficiency (duty ratio) and step-size, which can only be indirectly inferred from in vitro motility assays can now be studied by using single-molecule techniques that allow direct and simultaneous observation of ATP-turnover and force generation.

However, the process of controlling the motion of bio-filaments driven by motor proteins is very complex and multi-factorial, which makes it difficult to understand involved mechanisms from experimental observations alone. Great efforts in theoretical work have also been made to study the interaction between motor proteins and cytoskeleton filament.

1.4 Mechanics of motor proteins and the cytoskeleton

For the motility of cytoskeleton filaments driven by motor proteins, there are three main types of force acting on the filaments: mechanical, thermal, and chemical. The mechanical force can be divided into three subtypes: the driving

force from motor proteins, a viscous force from solution, and a bending force from filament bending.

1.4.1 The mechanical force

There are three mechanical forces generated on a cytoskeleton filament during its motion driven by motor proteins. The first one comes directly from motor proteins, which convert the chemical energy from ATP hydrolysis into mechanical energy. This force drives the filament to move. Since the filament moves in a solution, there is a viscous resistance to its motion. This force drags the movement of the filament (called viscous force). In addition, as a slender polymer, the filament can be folded or bent in the solution. A bending force is thus generated to resist the bending or folding (more explanation in chapter 1.4.1 C).

Among the three forces, the interactions between motor proteins and cytoskeleton filaments are most important and complicated since these are related to the energy conversion, ATP hydrolysis, and the complex structures of motor proteins and filaments. Significant efforts have been made to study the driving mechanism of motor proteins on cytoskeleton filament.

A. The interaction between protein motor and cytoskeletal filament

It is well known that the motor proteins can drive and direct actin filaments or microtubules by consuming the energy from ATP hydrolysis. How

does it happen and what is the mechanism involved? Understanding the driving mechanism of protein motor on cytoskeletal filaments is a key to study the motility of these filaments. In 1957, Huxley [73] proposed a rotational model, which provided a molecular basis for the contraction of a muscle. In the model, it was assumed that the bending or rotation of crossbridges causes the actin-containing thin filaments to slide relative to the myosin-containing thick filaments, which, in turn, leads to shortening of the muscle. Fig.1.16 illustrates the rotating crossbridge model for myosin. Firstly, the binding of myosin to the actin filament catalyzes the release of phosphate from the motor domain and induces the formation of a highly strained ADP state. Secondly, the resultant strain drives the converter domain to rotate, which is connected to a lever domain that amplifies the motion, moving the load through the working distance. Thirdly, following the ADP release, ATP binds to the motor domain and causes dissociation of myosin from the actin filament. Finally, during the dissociation process, the crossbridge recovers to its initial conformation, so that the motor is able to be attached to a next binding site on the filament.

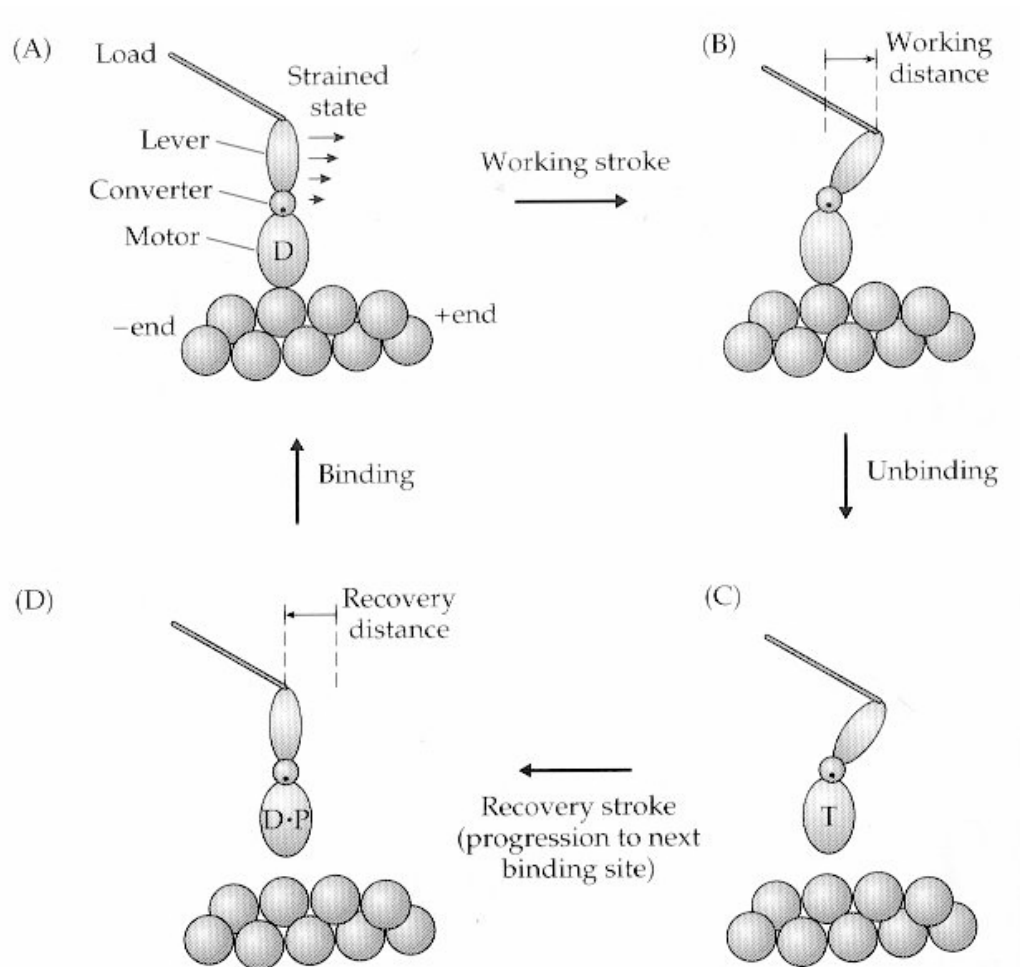


Fig.1.16 The rotating crossbridge model for myosin motor [73]

The rotating crossbridge has been proven to be a general mechanism responsible for the cell motility that is responsible for the beating of cilia and flagella, the movement of organelles, and the segregation of chromosomes. This mechanism is also applicable to dynein [74] and kinesin [75]. There is strong crystallographic evidence that the light-chain binding domain does rotate during each ATP hydrolysis cycle. The structure of the converter domain that forms the junction between the motor domain and the light-chain binding domain depends

on the nucleotide bound at the active site. Fig.1.17 illustrates the pre-powerstroke and post-powerstroke state of Dictyostelium myosin docked to actin. It has been demonstrated that the changes in the converter domain are expected to cause a rotation of the light-chain domain by about 70 degrees [76]. This model provides a framework including the structural, biochemical, and mechanical properties of motor molecules.

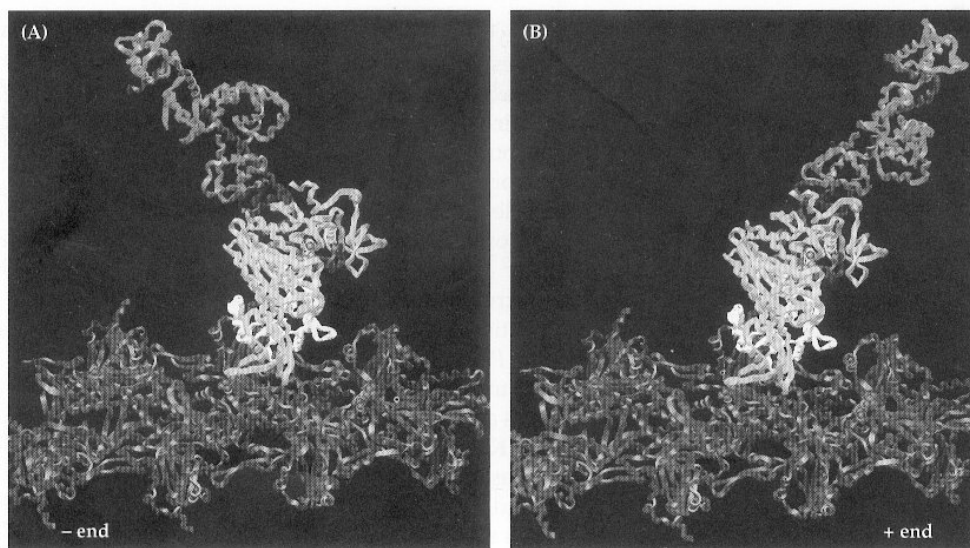


Fig.1.17 Beginning and end of myosin's working stroke [76]

In Huxley's model, a powerstroke model is proposed. In the model, it is assumed that a protein motor has an elastic element acting as a spring, which stores the mechanical energy. The conformational change of protein motor strains the spring for ATP hydrolysis, The driving force from the motor is a result of the release of the strain stored in the spring. Fig.1.18 illustrates the powerstroke process [73]. Firstly, associated with the ATP hydrolysis, a conformational change in the crossbridge produces strain in an elastic element. The strain

generates tension, which drives the filament to move. The maximum force is the product of powerstroke distance (δ_+) and the spring constant (κ). The crossbridge is then detached from the filament when the strain reaches zero.

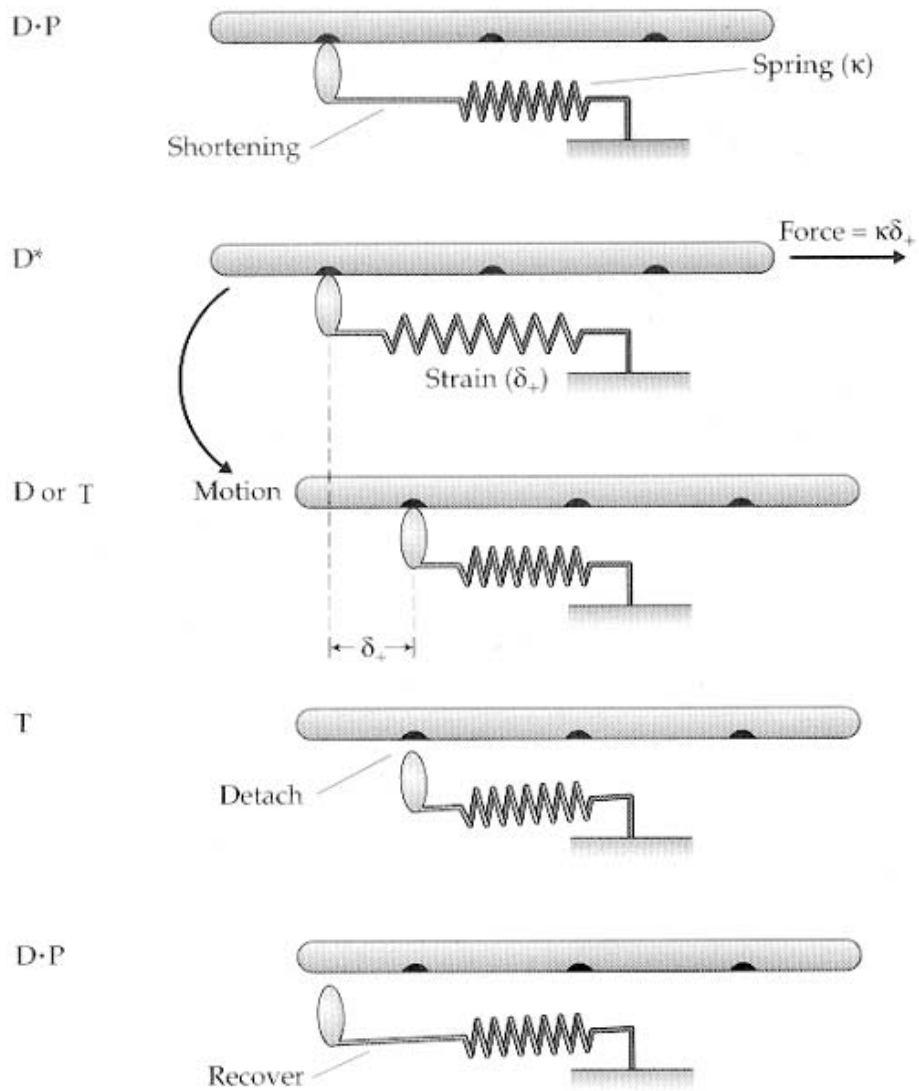


Fig.1.18 A powerstroke model (T = ATP, D = ADP, D* = Strained ADP, P = P_i)

[73]

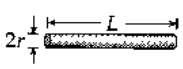
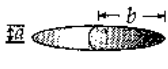
B. The viscous force

Viscous force plays a resisting role in the motion of a cytoskeleton filament. This force results from the friction between the filament and surrounding solution. The viscous force depends on the viscosity of the solution and the motion of the filament. This drag force can be expressed by the following equation:

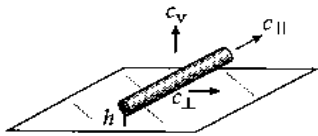
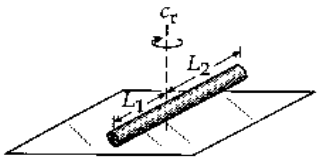
$$F_d = - \gamma \cdot V \quad (1.1)$$

Here γ is a drag coefficient, which is related to the viscosity of the solution and the shape of the filament, and V is the velocity of the filament along the direction of motion.

It is demonstrated that, for the filament, the drag coefficient is not a constant. It is much higher when the filament is near a substrate surface than that in the unbounded solution (i.e., that away from the substrate). In addition, the drag coefficient also depends on the moving direction of filament. Fig.1.19 illustrates the drag coefficient of the filament in unbounded solution and that near a surface [77].

Parameter	Direction	Cylinder ($L \gg r$)	Ellipsoid ($b \gg a$)	Sphere
				
γ_{\parallel}		$\frac{2\pi\eta L}{\ln(L/2r) - 0.20}$	$\frac{4\pi\eta b}{\ln(2b/a) - 0.5}$	$6\pi\eta r$
γ_{\perp}		$\frac{4\pi\eta L}{\ln(L/2r) + 0.84}$	$\frac{8\pi\eta b}{\ln(2b/a) + 0.5}$	$6\pi\eta r$
γ_r		$\frac{\frac{1}{3}\pi\eta L^3}{\ln(L/2r) - 0.66}$	$\frac{\frac{8}{3}\pi\eta b^3}{\ln(2b/a) - 0.5}$	$8\pi\eta r^3$
γ_a		$4\pi\eta r^2 L$	$\frac{16}{3}\pi\eta a^2 b$	$8\pi\eta r^3$

(a) unbounded solution

Definitions	Drag coefficient	Force or torque
	$c_{\parallel} = \frac{2\pi\eta}{\cosh^{-1}(h/r)} \equiv \frac{2\pi\eta}{\ln(2h/r)}$ $c_{\perp} = 2c_{\parallel}$	$F = c_{\parallel}Lv$ $F = c_{\perp}Lv$
	$c_v = 1 / (c_{\perp}^{-1} - c_a^{-1})$ $c_a = \frac{4\pi\eta}{[1 - (r/h)^2]^{1/2}}$	$F = c_vLv$ $T = c_a Lr^2\omega$
	$c_r = \frac{1}{3}c_{\perp}$	$T = c_r\omega(L_1^3 + L_2^3)$

(b) near surface

Fig.1.19 The drag coefficient of the filament under (a) unbounded solution, and (b) near a surface ^[77]

C. The bending force

As a slender filament, the cytoskeleton filament will be bent or folded in the solution during moving. This will generate an additional force to resist the bend trend. As Fig.1.20 illustrates, the bending moment of the filament is proportional to the curvature of the bent filament, $1/R$ (R is the radius of curvature) [55]. The equation can be expressed:

$$M = \frac{EI}{R} \quad (1.2)$$

where EI define as the flexural rigidity, which is a constant for a specific filament. I define as the shape moment of inertia of the cross-section, which is determined by the shape of the filament.

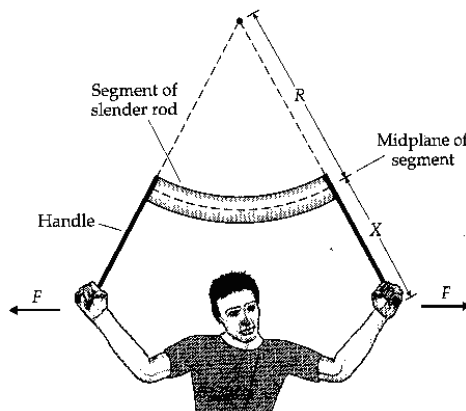


Fig.1.20 Bending of a slender rod due to a bending moment [55]

D. The mechanical behavior of cytoskeleton filaments

The study of the mechanical properties of cytoskeleton filaments will provide an insight into mechanical properties of cells, such as muscle cells or

sperm. Moreover, the mechanical properties of the filaments influence the motility of the filaments.

The most important property of the filaments is their flexural rigidity, which determines the bending of the filaments. There are four main methods to measure the filament's rigidity: 1) buckling force measurement using optical traps and beads [78, 79], 2) image analysis of the relaxation process following filament bending [80], 3) image analysis of filament bending via hydrodynamic flow [81], and 4) image analysis of thermal fluctuations of microtubule shapes in solution [82]. Fig.1.21 shows the apparatus for measuring the microtubule rigidity through the buckling force measured with the optical trap [79]. In the apparatus, the laser power is controlled by rotating the half-wave plate, HWP1, followed by a Glan-Laser polarizer. The ratio of the two beams is changed by rotating the half-wave plate, HWP2. Two laser beams are independently manipulated by changing the angles of the galvano mirrors X1, Y1 and X2, Y2.

Different measurement methods differ in many aspects, e.g., the type of force applied, the balance and direction of working forces. Thus the values of the flexural rigidity of microtubule determined using the four methods differ over a range of two orders of magnitudes, as Tuszynski indicated, from $2.9 \times 10^{-24} \text{ Nm}^2$ to $45 \times 10^{-24} \text{ Nm}^2$ [79]. Although the experimental results are scattered, compared with the actin filament, microtubule still has much higher flexural rigidity but similar young's moduli. This explains why microtubule is harder to be bent or folded than actin filament.

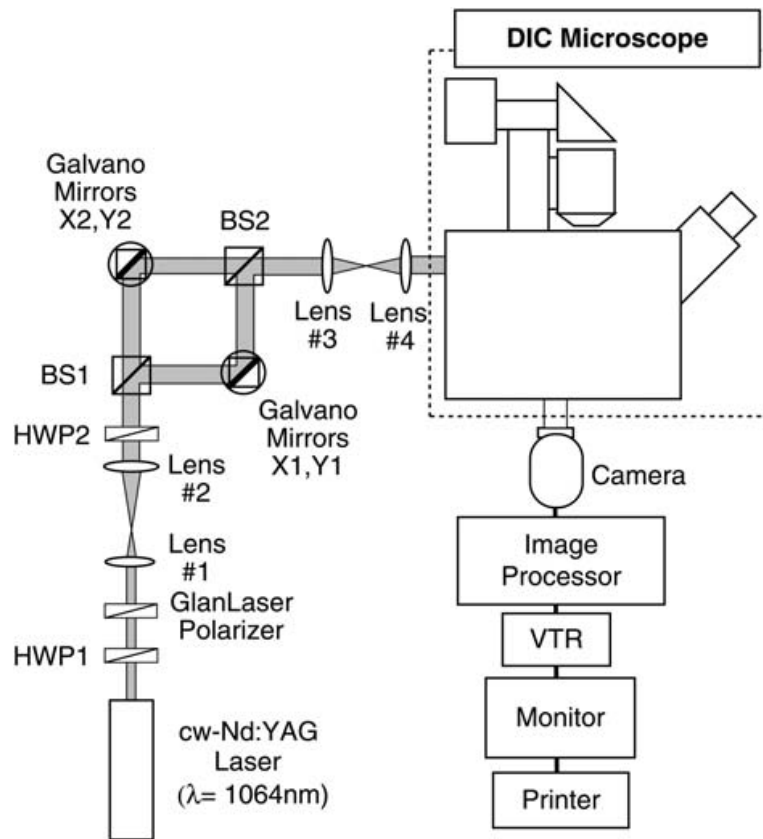


Fig.1.21 A schematic diagram of the video-enhanced DIC microscope with optical traps^[79]

1.4.2 The thermal force

In addition to the mechanical forces, cytoskeleton filaments and motor proteins are subject to thermal forces that arise from collisions with water and other molecules in the surrounding fluid. Each collision generates an impulsive force on the object that it strikes. The resulting motion is thermally generated. It is random and called Brownian motion.

Investigation of the thermal motion is crucial for understanding molecular and cellular mechanics, because the chemical reactions that drive biological processes produce energies that are only a little higher than the thermal energy. Therefore, the thermal motion or fluctuation is large and cannot be ignored.

For a molecule, the average thermal energy is [55]:

$$\langle U \rangle = \frac{1}{2} k \langle x^2 \rangle = \frac{1}{2} KT \quad (1.3)$$

where K is the Boltzmann's constant, T is the temperature.

The diffusion is a random walk and can be expressed by the following diffusion equation [55]:

$$\frac{\partial C(x,t)}{\partial t} = D \frac{\partial^2 C(x,t)}{\partial x^2} \quad (1.4)$$

where D is the diffusion coefficient, and C is the concentration.

1.4.3 The chemical forces

In addition to the mechanical and thermal forces, cytoskeleton filament and motor proteins are also subject to chemical forces that arise from the formation of intermolecular bonds. For example, the polymerization of actin filaments or microtubules causes the protein to move in one direction. To understand how the motor proteins work as a biological engine, it is important to understand how proteins move in response to these chemical forces. Δx

Forces can influence equilibrium and the rate of chemical reactions. If the length of molecule changes by $\Delta x = x_2 - x_1$ as a result of a conformational change, as Fig.1.22 shows, then the difference in free energy will be [55]:

$$\Delta G = \Delta G^0 - F \cdot \Delta x \quad (1.5)$$

where F is the tension across the molecule due to the conformational change and ΔG^0 is the corresponding change in the free energy relative to the state in the absence of tension.

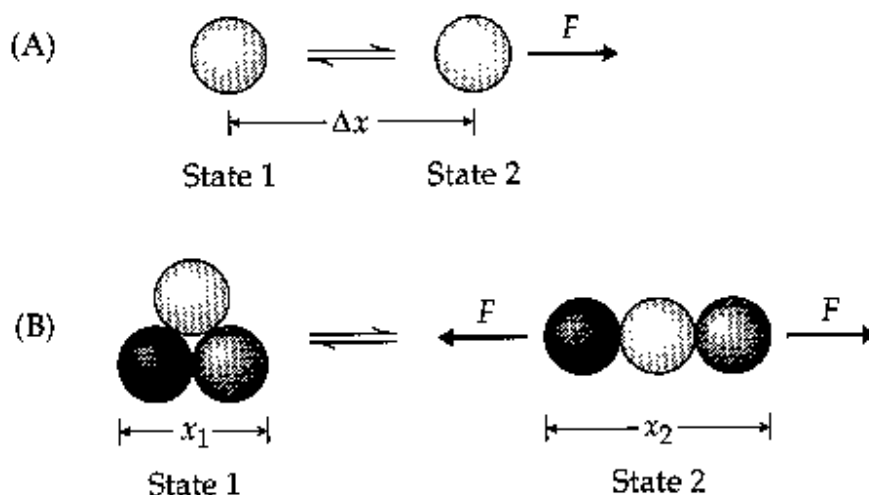


Fig.1.22 The schematic illustration of two states of molecule under external force ^[55]

It was discovered that the actin polymerization and microtubule depolymerization can generate force [83, 84]. In the case of microtubules, forces as large as 2 pN have been inferred from instances when a microtubule is inside a vesicle buckles [85]. Fig.1.23 illustrates an equilibrium polymer model for external force generation during polymerization. In the model, a compressive force F counters the polymerization. Then the mechanical energy of $(n+1)$ th monomer in the filament exceeds that of n th monomer by $F \cdot \delta$, where δ is the increase in length due to the incorporation of one monomer.

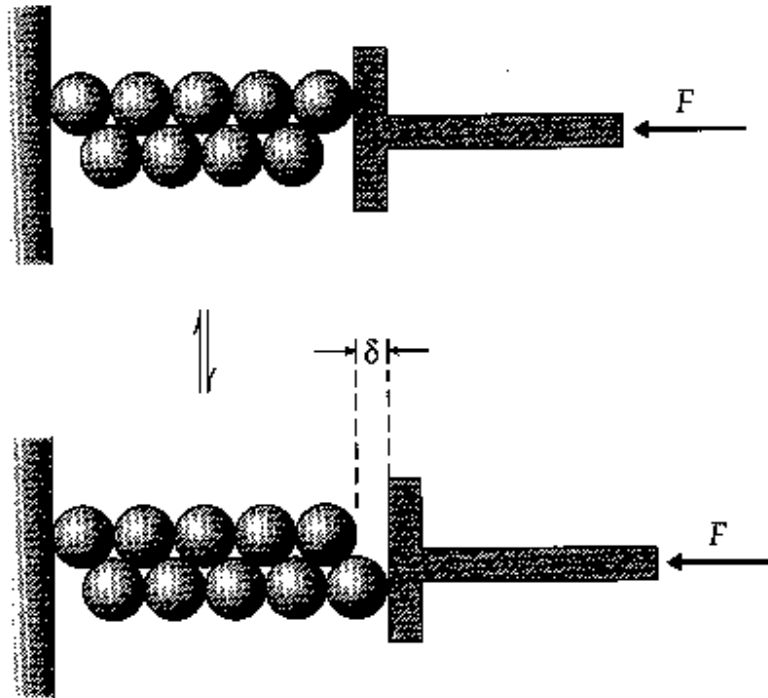


Fig.1.23 The schematic illustration of the polymerization of filament under external force ^[55]

For actin, it is equal to 2.75nm, while for a microtubule, it is about 8nm/13 = 0.6nm. The equilibrium force for a given monomer concentration in the system can then be expressed as [55]:

$$F_{eq} = \frac{kT}{\delta} \ln \frac{[A_1]}{K_c} \quad (1.6)$$

where $[A_1]$ is the monomer concentration, T is the temperature of system, K_c is the critical concentration in the absence of external force.

The theoretical work may provide us a better insight into the mechanics of motor proteins, e.g., what factors affect the motility of cytoskeleton? How is a specific force generated? How do molecular motors coordinate to drive

cytoskeleton? Computational modeling has provided an effective tool for studying the motility of cytoskeletons driven by molecular motors, which is described in the following section.

1.5 Computational modeling

In 1957, Huxley [73] proposed a model to treat a protein motor as an elastic spring storing mechanical energy. This approach establishes the basis of a powerstroke model. Details about this model are given in ref [73] and also mentioned earlier. Based on the powerstroke model, Holmes [86] proposed a swinging lever-arm model to explain the mechanism for the myosin and actin filament, which included a catalytic ATPase cycle consisting of four fundamental steps. As Fig.1.24 illustrates, myosin is firstly bound to an actin filament to form actomyosin. In the second step, binding of ATP takes place at an empty site located at the motor domain of actomyosin, lowering the affinity of the motor domain toward the actin filament. Consequently, actomyosin is dissociated into the ATP-myosin conjugate and the actin filament. The binding of ATP also triggers a conformational change of the neck domain, leading to a pivotal motion on the motor domain. In the third step, hydrolysis of the ATP-myosin conjugate gives out a complex of an ADP-myosin conjugate and phosphate Pi, which is then bound to the actin filament. This binding is weak and called a "weak-binding state". Finally, the binding conjugate releases ADP and Pi stepwise, resulting in a conformational change of the motor domain. This motion causes the contraction

of muscles, which is called the "power stroke". A different mechanism, so-called biased Brownian ratchet model, was proposed recently. In the model, the motion of myosin on actin filament was driven by a directionally biased Brownian motion [87, 88].

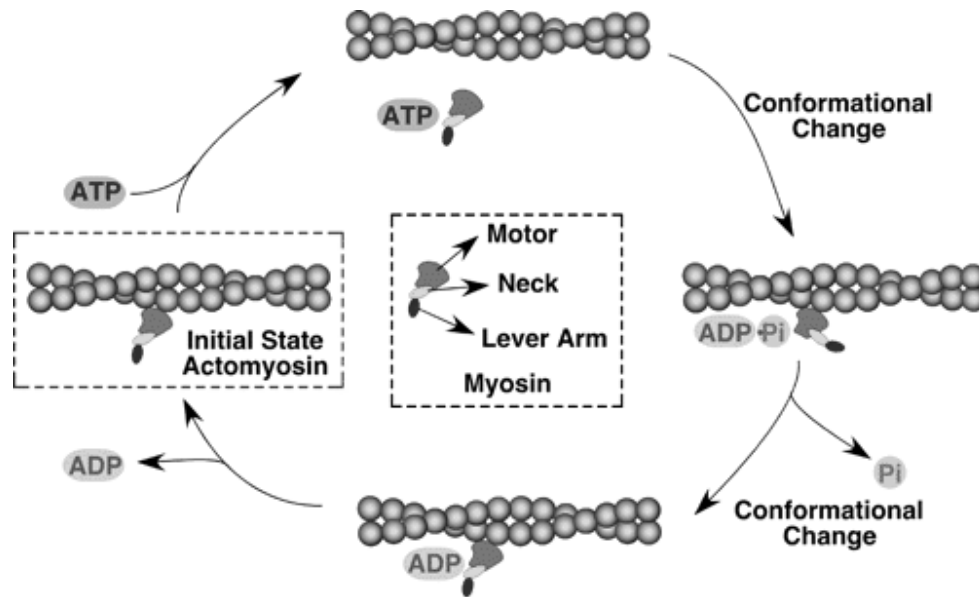


Fig.1.24 Schematic of the ATPase cycle involving myosin II and actin filament ^[86]

Howard [89] recommended a hand-over-hand and inchworm mechanisms to explain the walking motion of two-headed kinesins. The basis of hand-over-hand model is that the two heads are related by an axis of rotational symmetry and undergo identical, sequential motion. As Fig.1.25 illustrates, in (i) the trailing head is stippled, which indicates that it is incorrectly oriented to be bond to the microtubule (the symmetry axis bisects the heads). The transition (i) -> (ii) is hypothesized to entail a rotation of the distal part of the attached head to bring the trailing head forward. The symmetry breaking transition rotates this head so that it

can now be bond to the microtubule (iii). The unbinding of the now trailing head pulls the load forward (iv).

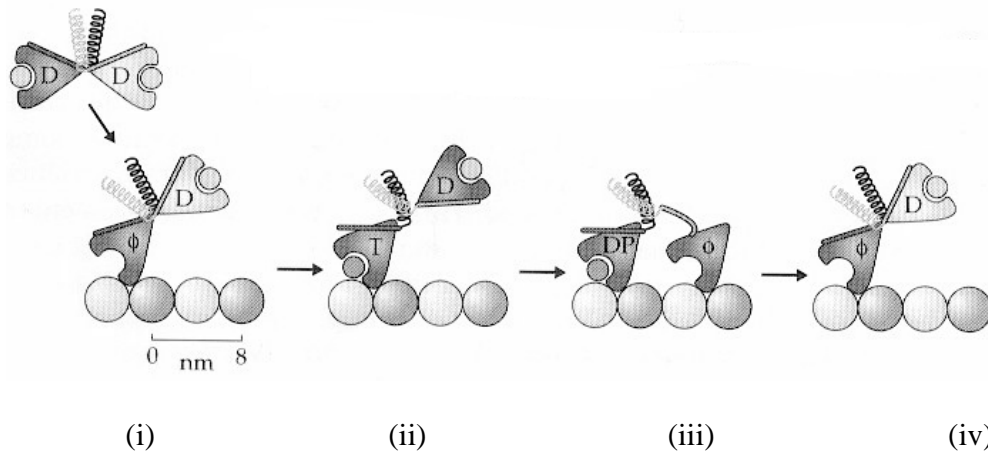


Fig.1.25 Hand-over-hand model for conventional kinesin: D = ADP, T = ATP, DP = ADP+PI. ^[89]

An alternative hypothesis is that kinesin head movement is coordinated through an “inchworm” mechanism in which the structure of the kinesin-microtubule complex is identical at the beginning of each cycle but the two heads do not swap places [90, 91]. Thus, there is no net neck rotation in each cycle. Such a mechanism differs fundamentally from the symmetric hand-over-hand type in that the two identical subunits of the kinesin homodimer are maintained in different environments and therefore have non-equivalent enzymatic cycles. In addition, Qian [92] studied force–velocity relationship and the stochastic stepping of single kinesin based on the theory of Markov processes. Gao et al. [93] proposed a molecular dynamics model based on free-energy simulations and

experimental binding constant measurements, which makes it possible to develop a kinetic scheme to understand the ATP hydrolysis by F1-ATPase.

These models have helped to successfully explain how a single motor binds and drives cytoskeleton to move during ATP hydrolysis. With the models, one could predict the driving force from a single protein motor attached on a cytoskeleton filament. However, when predicting the motility of cytoskeleton, one needs to develop a more complicate model since this motion involves the coordination of multiple motor proteins, the bending moment of microtubules, hydrodynamics and thermodynamics.

Bending is a very important characteristic of cytoskeleton filament. Brokaw [94] developed a bending model based on the balance of bending moments. In the model, the movement of an elastic filament in a viscous medium was computed using a fourth-order nonlinear partial differential equation obtained by balancing bending moments at all points along the length of the filament. The basic assumption of this analysis is that the following equation must be satisfied at every value of s :

$$M_A + M_E + M_V = 0 \quad (1.7)$$

where M_A represents the bending moment resulting from actively generated forces, M_E represents the bending moment resulting from elastic bending resistance of the microtubule, and M_V represents the bending moment resulting from the viscous resistances of the surrounding medium. This model has been used to simulate 2-dimensional and 3-dimensional bending-wave propagation of microtubules and flagella [95-97].

A hybrid particle/continuum model was proposed by Lowe to simulate the motility of micro-filaments, such as the microtubule [98, 99]. In the model, the flexible filament is considered as a set of N rigidly connected beads. The rigid connections between beads impose the condition that stretching of the filament is negligible. The force on one of the individual beads reflect the forces acting on a segment of length $\Delta l = l/N$ of real filament with a total length l . The forces on the i th bead include:

- a tension force, \mathbf{F}_T , associated with the resistance of the filament to stretching;
- a bending force, \mathbf{F}_B , associated with the resistance of the filament to bending;
- an active bending force, \mathbf{F}_A , generated by the organism to induce movement;
- a viscous force, \mathbf{F}_V , exerted by the fluid on the filament.

The governing equation of motion for the i th bead can thus be written as

$$m_i \frac{dV_i}{dt} = \mathbf{F}_T + \mathbf{F}_B + \mathbf{F}_A + \mathbf{F}_V \quad (1.8)$$

where the bead mass $m_i = m/N$, V_i is the velocity of the bead. The model has been used to investigate the sperm's swimming mechanism.

In both the bending moment model and hybrid particle/continuum model, the bending factor and hydrodynamics are considered. As continuum model, a large system can be simulated with a large time step. However, thermodynamics

is ignored in the models. Besides, the driving force from motor proteins is over simplified in the models. Hence, it is difficult to use these models to further investigate some factors involving the synergy of motors, such as the density of motors and the effects of coordination motor proteins on the dragging force and driving force, which may have great impact on the movement of biofilaments driven by the motor proteins.

Considering the advantages and disadvantages of various models, great efforts have continuously been made to develop more effective and realistic modeling approaches to simulate the kinetic behavior of cytoskeleton filaments driven by motor proteins. In the present work, a general model involving mechanical properties of dyneins and microtubules, the interaction between dyneins and microtubules, bending moments, and hydrodynamics, was proposed. This model has been applied to simulate unidirectional motion of a microtubule driven by dynein motors and joining of microtubules. Furthermore, a Monte Carlo approach was incorporated to study the self-organized movement of microtubules.

Reference

1. Schliwa, M.E. 2003. *Molecular Motors*. Wiley-VCH: Weinheim
2. Rayment, I., H.M. Holden, M. Whittaker, C.B. Yohn, M. Lorenz, K.C. Holmes, R.A. Milligan. 1993a. Structure of the actin-myosin complex and its implications of muscle contraction, *Science* 261: 58-65
3. Kamal A., L.S. Goldstein. 2000. Connecting vesicle transport to the cytoskeleton. *Curr. Opin. Cell Biol.* 12:503-508.
4. Kamal, A., L.S.B. Goldstein. 2002. Principles of cargo attachment to cytoplasmic motor proteins. *Current Opinion in Cell Biology* 14: 63-68
5. Hirokawa, N, R. Takemura. 2003. In *Kinesin superfamily proteins* In *Molecular Motors* (Schliwa, M., ed.), 79–109, Wiley-VCH
6. Zhao, C, J. Takita, Y. Tanaka, M. Setou, T. Nakagawa, S. Takeda, H.W. Yang, S. Terada, T. Nakata, Y. Takei, M. Saito, S. Tsuji, Y. Hayashi, N. Hirokawa. 2001. Charcot-Marie-Tooth disease type 2A caused by mutation in a microtubule motor KIF1Bb. *Cell* 105, 587–597
7. Pazour, G.J., B.L. Dickert, Y. Vucica, E.S. Seeley, J.L. Rosenbaum, G.B. Witman, D.G. Cole. 2000. *Chlamydomonas* IFT88 and its mouse homologue, polycystic kidney disease gene *tg737*, are required for assembly of cilia and flagella. *Journal of Cell Biology* 151: 709–718
8. Afzelius B.A. 1976. A human syndrome caused by immotile cilia. *Science*, 193: 317-319
9. Seidman, C.E. and J.G. Seidman. 2000. Hypertrophic cardiomyopathy. In

- Metabolic and Molecular Bases of Inherited Diseases (Scriver, C.R. et al., eds), 5433–5452, McGraw-Hill
10. Vallee, R.B., P. Hook. 2003. Molecular motors: A magnificent machine. *Nature* 421: 701-702
 11. Hess, H., G.D. Bachand, V. Vogel. 2004. Powering nanodevices with biomolecular motors. *Chemistry-A European Journal* 10: 2110-2116
 12. Carter, N.J., R.A. Cross. 2005. Mechanics of the kinesin step. *Nature* 435: 308-312
 13. Schmidt, J.J., C.D. Montemagno, Bionanomechanical systems, *Annual Review of Materials Research* 34: 315–337
 14. Kazushi K., A. Takuzo. 2005. Toward intelligent molecular machines: Directed motions of biological and artificial molecules and assemblies. *Chem. Rev.* 105: 1377-1400
 15. Suzuki, H., K. Oiwa, A. Yamada, H. Sakakibara, H. Nakayama and S. Mashiko. 1995. Linear arrangement of motor protein on a mechanically deposited fluoropolymer thin-film, *Japanese Journal of Applied Physics Part 1 – Regular Papers Short Notes & Review Papers* 34: 3937-3941
 16. Dennis, J.R., J. Howard and V. Vogel. 1999. Molecular shuttles: directed motion of microtubules along nanoscale kinesin tracks. *Nanotechnology* 10: 232-236
 17. Suzuki, H., A. Yamada, K. Oiwa, H. Nakayama, S. Mashiko. 1997. Control of actin moving trajectory by patterned polymethyl methacrylate tracks. *Biophysical Journal* 72: 1997-2001

18. Hiratsuka, Y., T. Tada, K. Oiwa, T. Kanayama and T.Q. Uyeda. 2001. Controlling the direction of kinesin-driven microtubule movements along microlithographic tracks. *Biophysical Journal* 81: 1555-1561
19. Clemmens, J., H. Hess, J. Howard and V. Vogel. 2003a. Analysis of microtubule guidance in open microfabricated channels coated with the motor protein kinesin. *Langmuir* 19: 1738-1744
20. Clemmens, J., H. Hess, R. Lipscomb, Y. Hanein, K.F. Bohringer, C.M. Matzke, G.D. Bachand, B.C. Bunker and V. Vogel. 2003b. Mechanisms of microtubule guiding on microfabricated kinesin-coated surfaces: Chemical and topographic surface patterns. *Langmuir* 19: 10967-10974.
21. Kabsch, W., H.G. Mannherz, D. Suck, E.F. Pai, K.C. Holmes. 1990. Atomic-structure of the actin – dnase-I complex. *Nature* 347: 37-44
22. Holmes, K.C., D. Popp, W. Gebhard, W. Kabsch. 1990. Atomic model of the actin filament. *Nature* 347: 44-49
23. Rayment, I., H.M. Holden, M. Whittaker, C.B. Yohn, M. Lorenz, K.C. Holmes, R.A. Milligan. 1993a. Structure of the actin-myosin complex and its implications of muscle contraction. *Science* 261: 58-65,
24. Vale, R. D., T. S. Reese, M. P. Sheetz. 1985. Identification of a novel force-generating protein, kinesin, involved in microtubule-based motility. *Cell* 42:39-50
25. Kozielski, F., S. Sack, A. Marx, M. Thormahlen, E. Schonbrunn, V. Biou, A. Thompson, E.M. Mandelkow, E. Mandelkow. 1997. Phe crystal structure of

- dimeric kinesin and implications for microtubule-dependent motility. *Cell* 91: 985-994
26. Kikkawa, M., Y. Okada, N. Hirokawa. 2000. 15 angstrom resolution model of the monomeric kinesin motor, KIF1A. *Cell* 100: 241-252
 27. King, S.M., 2000a. The dynein microtubule motor. *Biochimica et Biophysica Acta* 1496:60-75
 28. Dubella, L.M., S.M. King. 2001. Dynein motors of the chlamydomonas flagellum. *International Review of Cytology* 210:227-268
 29. Sakato, M., S. M. King. 2004. Design and regulation of the AAA plus microtubule motor dynein. *Journal of Structural Biology* 146:58-71
 30. Iyer, L. M., D. D. Leipe, E. V. Koonin, L. J. Aravind. 2004. Evolutionary history and higher order classification of AAA plus ATPases. *Journal of Structural Biology* 146:11-31
 31. Geeves, M.A., K.C. Holmes. 1999. Structural mechanism of muscle contraction. *Annu. Rev. Biochem.* 68:687-728
 32. Squire, J. 1981. *The structural basis of muscular contraction*. Plenum Press, New York.
 33. Nogales, E., M. Whittaker, R.A. Milligan, and K.H. Downing. 1999. High-resolution model of the microtubule. *Cell* 96:79-88
 34. Michison, T.J. 1993. Localization of an exchangeable GTP binding site at the plus end of microtubules. *Science* 261:1044-1047
 35. Becker, W.M., J. L. Kleinsmith, H. Hardin. 2006. *The world of the cell*. San Francisco: Pearson Benjamin Cummings, Inc.

36. Hirokawa, N., R. Takemura. 2004. Kinesin superfamily proteins and their various functions and dynamics. *Experimental Cell Research* 301: 50-59
37. Gibbons, I. R. 1963. Studies on the Protein Components of Cilia from *Tetrahymena pyriformis*. *Proceedings of the National Academy of Sciences of the United States of America* 50: 1002–1010
38. Schnapp, B. J., T. S. Reese. 1989. Dynein is the motor for retrograde axonal transport of organelles. *Proceedings of the National Academy of Sciences of the United States of America* 86: 1548–1552
39. Walczak, C. E., I. Vernos, T. J. Mitchison, E. Karsenti, R. Heald. 1998. A model for the proposed roles of different microtubule-based motor proteins in establishing spindle bipolarity. *Current Biology* 8: 903–913
40. Gibbons, I. R. 1996. The role of dynein in microtubule-based motility. *Cell Structure and Function* 21: 331-342
41. Seidman, J.G., C. Seidman. 2001. The genetic basis for cardiomyopathy: from mutation identification to mechanistic paradigms. *Cell* 104, 557–567
42. Probst, F.J., Fridell RA, Raphael Y, Saunders TL, Wang AH, Liang Y, Morell RJ, Touchman JW, Lyons RH, Noben-Trauth K, Friedman TB, Camper SA. 1998. Correction of deafness in shaker-2 mice by an unconventional myosin in a BAC transgene. *Science* 280: 1444–1447
43. Wang, A., Y. Liang, R.A. Fridell, F.J. Probst, E.R. Wilcox, J.W. Touchman, C.C. Morton, R.J. Morell, K. Noben-Trauth, S.A. Camper, T.B. Friedman. 1998. Association of unconventional myosin MYO15 mutations with human nonsyndromic deafness DFNB3. *Science* 280: 1447–1451

44. Gibson, F., J. Walsh, P. Mburu, A. Varela, K. A. Brown, M. Antonio, K. W. Beisel, K. P. Steel, S. D. M. Brown. 1995. A type VII myosin encoded by the mouse deafness gene shaker-1. *Nature* 374: 62–64
45. Weil, D., S. Blanchard, J. Kaplan, P. Guilford, F. Gibson, J. Walsh, P. Mburu, A. Varela, J. Levilliers, M.D. Weston, et al. 1995. Defective myosin VIIA gene responsible for Usher syndrome type 1B. *Nature* 374: 60–61
46. Avraham, K.B., T. HASSON, K. P. STEEL, D. M. KINGSLEY, and L. B. RUSSELL et al., 1995. The mouse Snell's waltzer deafness gene encodes an unconventional myosin required for structural integrity of inner ear hair cells. *Nature Genetics* 11: 369–375
47. Reid, E., M. Kloos M, A. Ashley-Koch, L. Hughes, A. Bevan, I.K. Svenson, F.L. Graham, P.C. Gaskell, A. Dearlove, M.A. Pericak-Vance, D.C. Rubinsztein DC, D.A. Marchuk. 2002. A kinesin heavy chain (KIF5A) mutation in hereditary spastic paraplegia (SPG10). *American Journal of Human Genetics* 71:1189–1194
48. Milisav T. 1998. Dynein and dynein-related genes. *Cell Motility Cytoskeleton*, 39: 261-272
49. Smith, D.S., M. Niethammer, R. Ayala, Y. Zhou, M.J. Gambello, A. Wynshaw-Boris, L.H. Tsai. 2000. Regulation of cytoplasmic dynein behaviour and microtubule organization by mammalian Lis1. *Nature cell biology* 2: 767–775

50. Tai, C.Y., D. L. Dujardin, N.E. Faulkner, R.B. Vallee. 2002. Role of dynein, dynactin, and CLIP-170 interactions in LIS1 kinetochore function. *Journal of Cell Biology* 156: 959–968
51. Robinson, T., A. Blundell, C.F. Dutta, and K. Firman. 2004. A molecular motor that links the biological and silicon worlds. *NSTI-Nanotech.* v1:106
52. Hiratsuka, Y., T. Tada, K. Oiwa, T. Kanayama, T.Q.P. Uyeda. 2001. Controlling the direction of kinesin-driven microtubule movements along microlithographic tracks. *Biophysical Journal* 81:1555-1561
53. Sheetz, M.P., and J.A. Spudich. 1983. Movement of myosin-coated fluorescent beads on actin cables in vitro. *Nature* 303:31-35
54. Spudich, J.A., S.J. Kron, and M.P. Sheetz. 1985. Movement of myosin-coated beads on oriented filaments reconstituted from purified actin. *Nature* 315:584-586
55. Howard, J. 2001. *Mechanics of motor proteins and the cytoskeleton.* Sinauer Associates, Inc. Sunderland, Massachusetts.
56. Suzuki, H., K. Oiwa, A. Yamada, H. Sakakibara, S. Mashiko, and H. Nakayama. 1995. Linear arrangement of motor protein on a mechanically deposited fluoropolymer thin-film. *Japanese Journal of Applied Physics* 34:3937-3941
57. Oiwa, K. 2003. Protein motors: their mechanical properties and application to nanometer-scale devices. *Materials Science Forum* 426-432: 2339

58. Hiratsuka, Y., T. Tada, L. Oiwa, T. Kanayama and T.Q. Uyeda. 2001. Controlling the direction of kinesin-driven microtubule movements along microlithographic tracks, *Biophysical Journal* 81: 1555-1561
59. Shingyoji, C., H. Higuchi, M. Yoshimura, E. Katayama and T. Yanagida. 1998. Dynein arms are oscillating force generators. *Nature* 393: 711-714
60. Oiwa K., D.Y. Li, Y. Shitaka, R. Nakamori and H. Sakakibara. 2007. Molecular and Nanometer-Scale Self-Organized System Generated by Protein Motor Functions. *Mater. Sci. Forum* 539: 3290-3296
61. Rayment, I., W.R. Rypniewski, K. Schmidt-Base, R. Smith, D.R. Tomchick, M.M Benning, D.A. Winkelmann, G. Wesenberg and H.M. Holden. 1993. Three-dimensional structure of myosin subfragment-1: a molecular motor. *Science* 261: 50-58.
62. Kull, F. J., E.P. Sablin, R. Lau, R.J. Fletterick and R.D. Vale. 1996. Crystal structure of the kinesin motor domain reveals a structural similarity to myosin, *Nature* 380: 550-555.
63. Burgess, S.A., M.L. Walker, H. Sakakibara, P.J. Knight and K. Oiwa. 2003. Dynein structure and power stroke. *Nature* 421: 715-718.
64. Gittes, F., B. Mickey, J. Nettleton and J. Howard. 1993. Flexural rigidity of microtubules and actin filaments measured from thermal fluctuations in shape. *Journal of Cell Biology* 120: 923-934
65. Nagashima, H., and S. Asakura. 1980. Dark-field light microscopic study of the flexibility of F-actin complexes. *Journal of Molecular Biology* 136: 169-182

66. Kojima, H., A. Ishijima and T. Yanagida. 1994. Direct measurement of stiffness of single actin filaments with and without tropomyosin by in vitro nanomanipulation. *Proceedings of the National Academy of Sciences of the U.S.A.* 91: 12962-12966.
67. Yasuda, R., H. Miyata and K.Jr. Kinoshita. 1996. Direct measurement of the torsional rigidity of single actin filaments, *Journal of Molecular Biology* 263: 227-236.
68. Sheetz, M.P. and J.A. Spudich. 1985. Movement of myosin-coated fluorescent beads on actin cables in vitro. *Nature* 303: 31-35
69. Howard, J., A.J. Hudspeth and R.D. Vale. 1989. Movement of microtubules by single kinesin molecules. *Nature* 342: 154-158
70. Viani, M.B., L.I. Pietrasanta, J.B. Thompson, A. Chand, I.C. Gebeshuber, J.H. Kindt, M. Richter, H.G. Hansma, P.K. Hansma. 2000. Probing protein-protein interactions in real time. *Nature Structural Biology* 7: 644-647
71. Kojima, H., M. Kikumoto, H. Sakakibara and K. Oiwa. 2002. Mechanical properties of a single-headed processive motor, inner-arm dynein subspecies-c of *Chlamydomonas* studied at the single molecule level. *Journal of Biological Physics* 28: 335-345
72. Wazawa, T. and M. Ueda. 2005. Total internal reflection fluorescence microscopy in single molecule nanobioscience. *Microscopy Techniques Advances in Biochemical Engineering/Biotechnology* 95: 77-106
73. Huxley, A.F. 1957. Muscle structure and theories of contraction. *Progress in Biophysics & Molecular Biology* 7: 255-318

74. Johnson, K.A. 1985. Pathway of the microtubule-dynein ATPase and the structure of dynein: a comparison with actomyosin. *Annu.Rev. Biophys. Biophys.Chem.* 14:161-188
75. Howard, J. 1996. The movement of kinesin along microtubules. *Annu. Rev. Physiol.*58:703-729
76. Holmes, J. 1997. Molecular motors: Structural adaptations to cellular functions. *Nature* 389:561-567
77. Hunt, A.J., F.Gittes, and J.Howard. 1994. The force exerted by a single kinesin molecule against a viscous load. *Biophysical Journal* 67:766-781
78. Kurachi, M., M. Hoshi, and H. Tashiro. 1995. Buckling of a single microtubule by optical trapping force: direct measurement of microtubule rigidity. *Cell Motil. Cytoskeleton.* 30:221–228
79. Tuszynski J.A., T. Luchko, S. Portet, and J.M. Dixon. 2005. Anisotropic elastic properties of microtubules. *Europe Physical Journal* 17: 29-35
80. Felgner, H., R. Frank, J. Biernat, E.-M. Mandelkow, E. Mandelkow, B. Ludin, A. Matus, and M. Schliwa. 1997. Domains of neuronal microtubule-associated proteins and flexural rigidity of microtubules. *Journal of Cell Biology* 138:1067–1075
81. Venier, P., A. C. Maggs, M.-F. Carlier, and D. Pantaloni. 1994. Analysis of microtubule rigidity using hydrodynamic flow and thermal fluctuations. *J. Biol. Chem.* 269:13353–13360

82. Gittes, F., B. Mickey, J. Nettleton, and J. Howard. 1993. Flexural rigidity of microtubules and actin filaments measured from thermal fluctuations in shape. *Journal of Cell Biology* 120:923–934
83. Ingber, D.E. 1997. Tensegrity: The architectural basis of cellular mechanotransduction. *Annu. Rev. Physiol.* 59:575-599
84. Ingber, D.E. 1998. The architecture of life. *Sci. Am.* 278:48-57
85. Fygenson, D.K., E. Braun, and A. Libchaber. 1997. Mechanics of microtubule-based membrane extension. *Physical review Letters* 79:4497-4500
86. Holmes, K.C. 1997. The swinging lever-arm hypothesis of muscle contraction. *Current Biology* 7 (2): 112-118
87. Ait-Haddou, R., W. Herzog. 2003. Brownian ratchet models of molecular motors. *Cell Biochemistry and Biophysics* 38:191-213
88. Yanagida, T., K. Kitamura, H. Tanaka, A.H. Iwane, S. Esaki. 2000. *Curr. Opin. Cell Biol.* 12:20.
89. Howard, J. 1996. The movement of kinesin along microtubules. *Annu. Rev. Physiol.* 1996 58:703-729
90. Hua, W., J. Chung, J. Gelles. 2002. Distinguishing inchworm and hand-over-hand processive kinesin movement by neck rotation measurements. *Science* 295:844-848
91. Asbury, C. L., A. N. Fehr, S. M. Block. 2003. Kinesin moves by an asymmetric hand-over-hand mechanism. *Science* 302:2130-2134

92. Qian, H. 1997. A simple theory of motor protein kinetics and energetics. *Biophysical Chemistry* 67: 263-267
93. Gao, Y.Q., W. Yang, R.A. Marcus, M. Karplus. 2003. A model for the cooperative free energy transduction and kinetics of ATP hydrolysis by F1-ATPase. *Proceedings of the National Academy of Sciences of the United States of America* 100: 11339-11344
94. Brokaw, C.J. 1972. Computer simulation of flagellar movement I. Demonstration of stable bend propagation and bend initiation by the sliding filament model" *Biophysical Journal* 12: 564-586
95. Brokaw, C.J. and D. R. Rintala. 1975. Computer simulation of flagellar movement III. Models incorporating cross-bridge kinetic. *J. Mechanochem. Cell Motil.* 3: 77-86
96. Brokaw, C.J. 1986. Computer simulation of flagellar movement VI. Simple curvature-controlled models are incompletely specified. *Biophysical Journal* 48: 633-642
97. Brokaw, C.J. 2002. Computer simulation of flagellar movement VIII: Coordination of dynein by local curvature control can generate helical bending waves. *Cell Motil. Cytoskel.* 53:103-124
98. Lowe, C. P. 2001. A hybrid particle/continuum model for microorganism motility. *Future Gen. Comp. Sys.* 17: 853–862
99. Lowe, C. P. 2003. Dynamics of filaments: modeling the dynamics of driven microfilaments. *Phil. Trans. R. Soc. Lond. B* 358: 1543–1550

Chapter 2

**A general model system for studying the
kinetic behaviour of microtubules driven by
dynein C**

2.1 Introduction

The motion of a microtubule driven by a number of dynein motors is a very complex process, involving ATP hydrolysis, energy conversion, driving and drag actions from the dynein motors, viscous and thermal forces from solution, density of dynein motors and so on, which are greatly influenced by the coordination among the motors. Because of experimental limitation, it is not easy to experimentally determine the roles that the individual factors play in the entire process. The previously proposed models are primarily used to explore the driving mechanism for a single motor on a cytoskeleton filament, and the resistance of surrounding liquid to the filament's motion, etc. The existing models are therefore not very suitable for investigating the effects of these factors on the filament's movement.

In order to elucidate experimental observations and understand mechanisms involved, especially the coordination functions of motor proteins on the motion of a microtubule, in this work, a general model system was developed, which takes into account the influence of dynein motors, viscous drag from the solution, bending and extending of microtubule during its movement.

2.2 Model description

2.2.1 A general model for motor proteins and microtubule system

As Fig.1.15 illustrates, there are several types of microtubules and their structures are complicated. In order to simplify the model, a microtubule is treated as a polymer chain composed of N segments, as Fig.2.1 shows [1]. The mass of each segment concentrates on its center. These centers are treated as beads connected by strings.

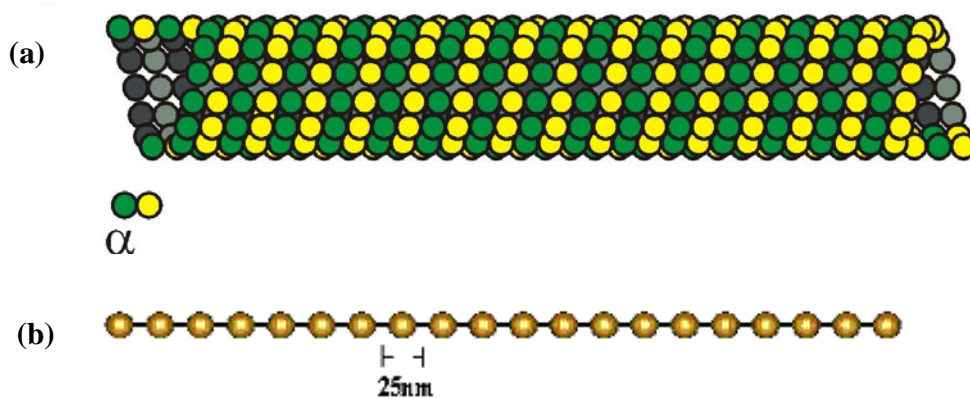


Fig.2.1 Structure of a microtubule: (a) a three-start helices structure ^[1],
(b) a polymer chain structure used to model a microtubule

Each bead represents a segment of filament (25nm). The strings between beads may extend or contract under the external or internal stress.

When a microtubule moves in the solution with dynein motors and ATP, its motion is influenced by many factors: the density and activity of dynein motors, the concentration of ATP in solution, viscosity of solution, distortion of the microtubule, polymerization and de-polymerization. Thus, simulating the motion of a microtubule driven by dynein motors is a very complex process,

which needs to consider the mechanical force from dynein motors, energy conversion from chemical energy to mechanical energy due to ATP hydrolysis, thermal force of Brownian motion, viscous force from the solution, bending energy, strain energy and torsion due to the movement and structural change of microtubule, and chemical force from polymerization and depolymerisation. Table 2.1 shows the levels of these forces [2].

Table 2.1 Examples of forces acting on molecules [2]

Type of force	Approximate magnitude
Elastic	1-100 pN
Covalent	10,000 pN
Viscous	1-1000 pN
Collisional	10^{-12} - 10^{-9} pN per collision/s
Thermal	100-1000 pN
Gravity	10^{-9} pN
Electrostatic and van der Waals	1-1000 pN

As a two-dimensional model, the torsion of microtubule is ignored. In addition, the polymerization and de-polymerisation of microtubules are ignored in the model. It is also assumed that there is sufficient ATP hydrolysis in the solution, which supplies enough energy for dynein to drive the microtubule.

Hence, in the system, the equation that governs the microtubule's motion for the i th microtubule bead can thus be written as:

$$m_i \frac{d^2 s_i}{dt^2} = F_i = F_{iS} + F_{iB} + F_{iD} + F_{iO} \quad (2.1)$$

where F_{iS} is a spring force associated with the stretching of spring connecting adjacent beads; F_{iD} is a driving force generated by dynein; F_{iB} is a bending force associated with the resistance of the filament to bend; F_{iO} is an force from environment, including viscous and thermal forces from solution, and collision force from other microtubules, which depends on system conditions. Fig.2.2 illustrates a sketch of force system.

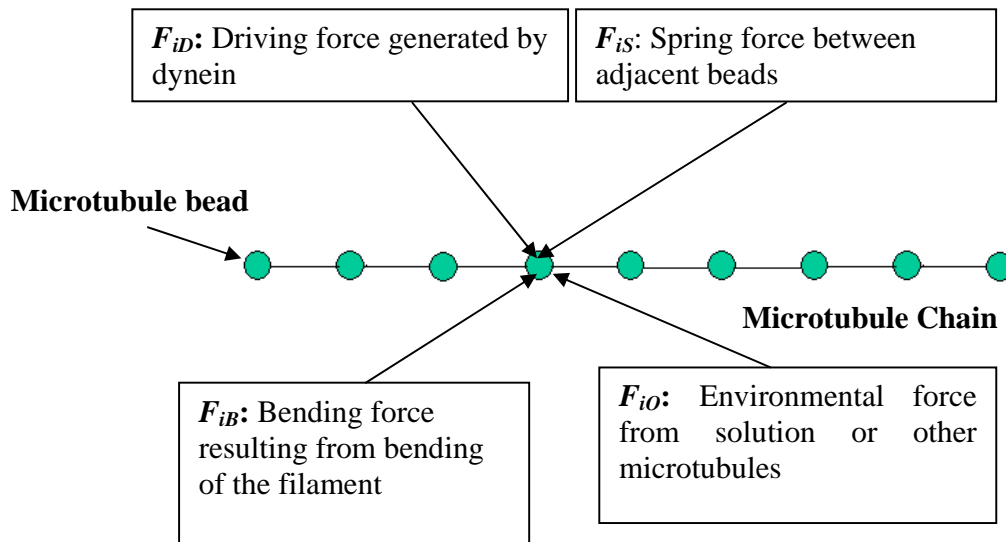


Fig.2.2 Forces exerted on a microtubule

2.2.2 The driving force from dyneins

According to the power stroke model [3], a motor protein was treated as a strained elastic string after receiving energy from ATP hydrolysis. The strained spring generated a driving force on a microtubule to which it was attached. When attached to the microtubule, the motor released its strain energy and thus drove the microtubule to move. For a single motor of dynein c, each power-stroke resulted in a displacement of about 8nm as determined experimentally [4].

Hence, for each stroke, the driving force from a motor on a microtubule may be expressed as:

$$F_d = k_d \cdot \Delta\delta \quad (2.2)$$

where k_d is the spring constant of the motor and $\Delta\delta$ is the stroke distance for dynein c.

In the model, two springs are used to represent the power stroke action as shown in Fig.2.3: spring 1 is used to drive a microtubule to move forward, and spring 2, which represents the stalk of dynein, is used to capture the microtubule. The motor is attached to a glass surface by its stem, which is assumed to be rigid and can only wave around the fixed position. The stress-free length of the stalk is 15nm and that of the stem is 13nm. The diameter of the motor is about 15nm [5]. When a motor is attached to a microtubule, spring 1 is full of strain energy given by ATP hydrolysis and it drives the microtubule to move (The driving period is defined as τ_{active}). After the displacement (8nm) is accomplished and the strain energy in spring 1 is consumed, spring 2 starts to drag the bead. The drag force is

kept for a certain period (τ_{drag}) until the motor is detached from the microtubule. During the following period of detachment (τ_{off}), the motor would obtain another energy unit from ATP hydrolysis and then grab the microtubule again, followed by another cycle, as Fig.2.3 illustrates.

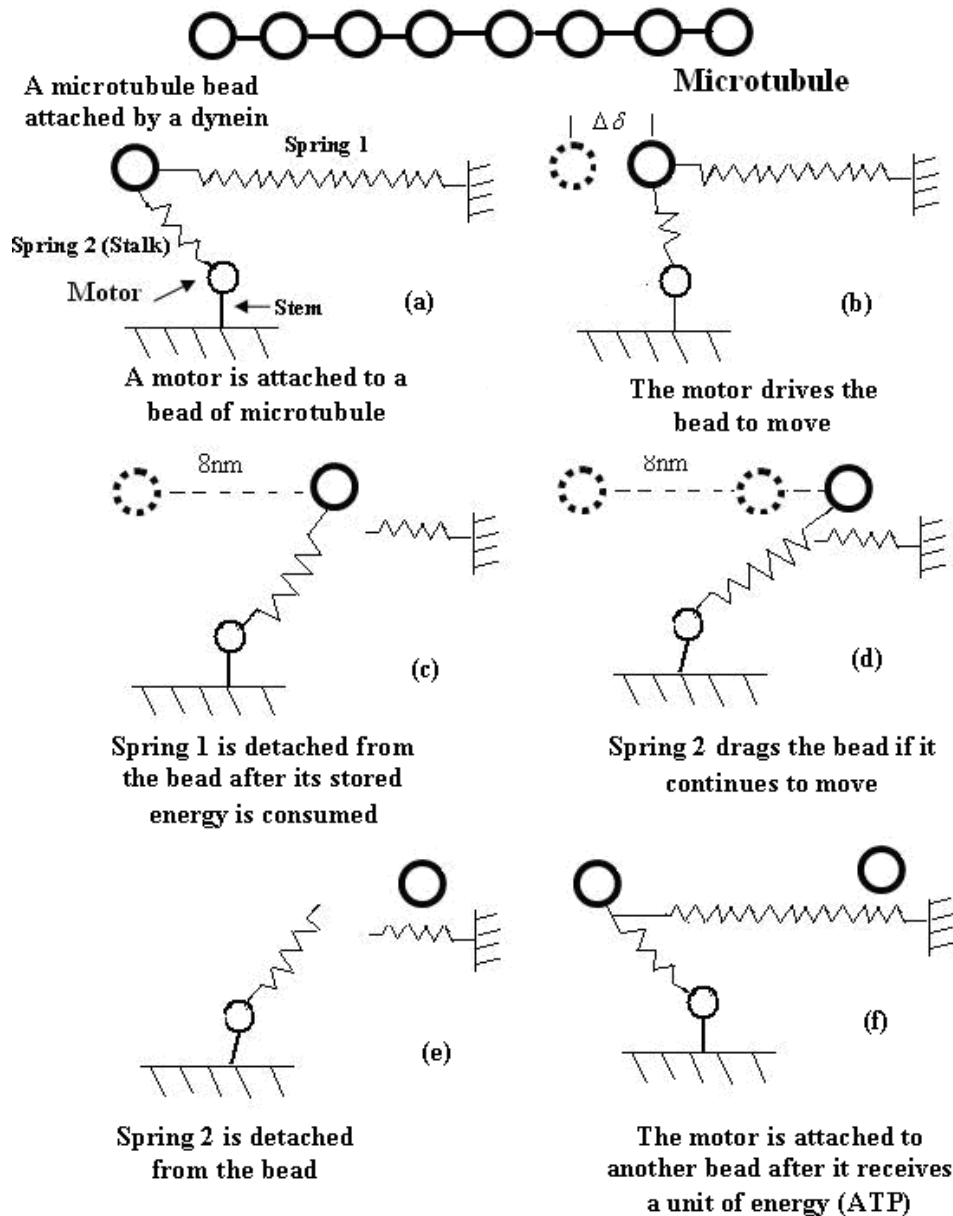


Fig.2.3 The sketch of an attaching and detaching process

The total attachment period τ_{on} is the sum of τ_{active} and τ_{drag} , $\tau_{on} = \tau_{active} + \tau_{drag}$. The cycle period time of dynein c is about 10 milliseconds. The duty ratio for dynein c is 0.14 [4]. Hence for dynein c, τ_{off} is about 6 times as long as τ_{on} .

In the model, the driving period (τ_{active}) of dynein c was assumed to be the same as τ_{drag} , which can, of course, be adjusted to match experimental observations. Such an assumption should not lead to misleading information when studying the mechanism for motor-microtubule interaction, rather than intending to obtain accurate quantitative data. Fig.2.4 schematically illustrates the three periods of an attaching and detaching cycle for a dynein c.

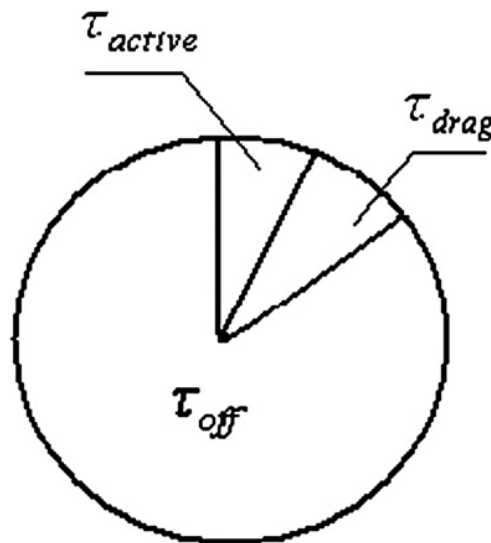


Fig. 2.4. An attaching and detaching cycle for dynein c.

The total driving force of motors on a microtubule bead i may be expressed as:

$$F_{iD} = \sum_{j=1}^n k \cdot \Delta\delta_j \quad (2.3)$$

where k is the spring constant of the molecular motor and $\Delta\delta_j$ is the stroke distance of dynein j and n is the total number of dyneins attached to the bead.

As Fig.2.5 illustrates, for a dynein c in the circle center, all the microtubule beads in the cycle region have opportunity to be attached by the dynein motor. The radius of cycle is equal to the sum of the lengths of stem and stalk. Since each dynein motor has its specific driving direction, only microtubule beads in the shaded region can be driven by the dynein motor if they are attached by it. Therefore, the opportunity for a microtubule bead to be driven is determined by the attaching probability of the dynein motor on the microtubule bead and driving region of the dynein motor.

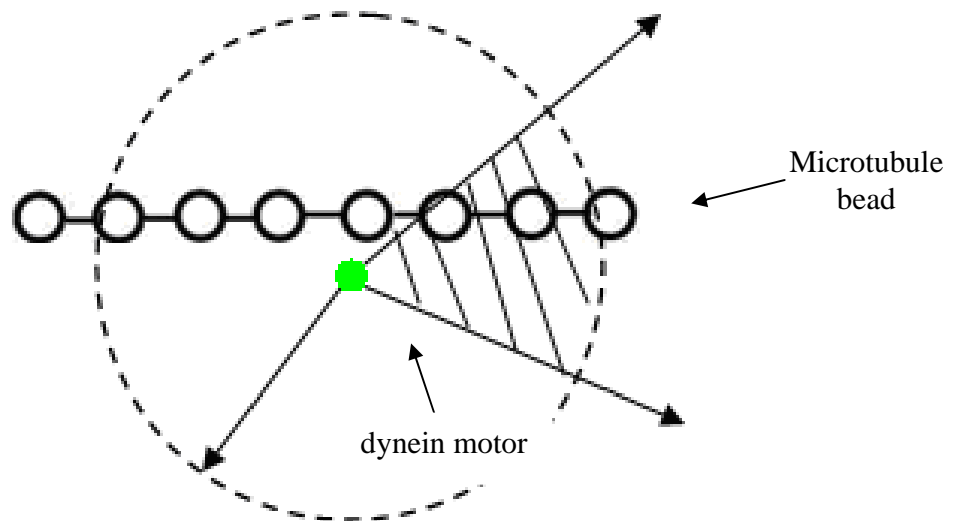


Fig.2.5 Sketch of driving region of a dynien motor

2.2.3 The spring force between adjacent beads

In this model, two adjacent beads are connected by a spring (Fig.2.1) and the force between neighbour beads i and j is expressed as [6]: r_{ij} , r_{eq}

$$F_{ij}^S = K_B (r_{ij} - r_{eq}) \hat{r}_{ij} \quad (2.4)$$

here K_B is the spring constant of connecting spring and r_{eq} is the stress-free spring length. For a microtubule, the spring constant of microtubule is expressed as:

$$K_B = \frac{EA}{L} \quad (2.5)$$

where E is the Young's modulus of the microtubule, which is determined experimentally, A is the cross-sectional area of the microtubule and L is the length of the microtubule.

The total string force on bead i can be expressed as:

$$F_{iS} = \sum_{j=1}^n F_{ij}^S \quad (2.6)$$

where n is the number of strings attached to the bead.

2.2.4 Bending Force

As Fig.2.6 illustrates, in a microtubule chain, two strings connects three consecutive beads, $i-1$, i and $i+1$. A bending angle, θ_i , is defined as the angle between vector r_{i-1} and r_i . For a short segment i , its bending potential can

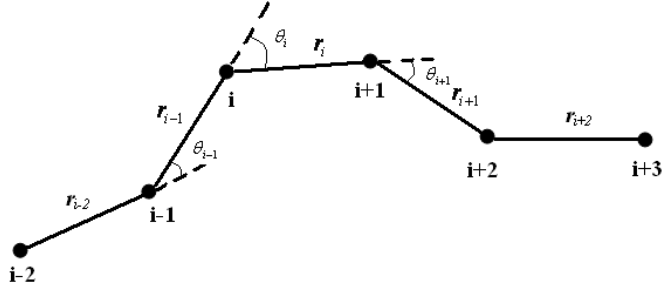


Fig.2.6 A bending microtubule chain

be expressed as [7]:

$$U_B(i) = \frac{G}{2} \cdot \frac{1}{R_i^2} \cdot \Delta l \quad (2.7)$$

where G is the bending constant of microtubule, R_i is the radius of curvature for segment i , Δl is the length of segment, which can be expressed as following [7]

$$G = \frac{\pi}{4} E r^4$$

$$\frac{1}{R_i^2} = \frac{1 - \cos(\theta_i)}{\Delta l^2} \quad (2.8)$$

where r is the radius of cross-section of the microtubule rod.

Therefore, the bending potential can be rewritten as

$$U_B(i) = \frac{\pi E r^4 [1 - \cos(\theta_i)]}{8 \Delta l} \quad (2.9)$$

The bending force on bead i results from three bending energies between groups of three connected beads, $i-1$, i , and $i+1$ [8]:

$$F_{iB} = - \sum_{j=i-1}^{i+1} \nabla(U_B(j)) = - \sum_{j=i-1}^{i+1} \left(\frac{dU_B(j)}{d \cos(\theta_j)} \right) \cdot \nabla(\cos(\theta_j)) \quad (2.10)$$

Details for calculating F_{iB} are described in Appendix E.

2.2.5 Environmental Forces

F_{i0} mainly comes from the interactions between microtubule and its environment, such as the solution and other microtubules. They are treated differently in various situations, which will be discussed in following context.

2.3 The simulation process

Once the force on a liquid particle is given, its velocity and trajectory can be determined using a modified Velocity-Verlet algorithm [8]:

$$\begin{aligned}\vec{r}_i(t + \Delta t) &= \vec{r}_i(t) + \Delta t \cdot \vec{v}_i(t) + \frac{1}{2}(\Delta t)^2 \frac{\vec{f}_i(t)}{m_i} \\ \vec{v}_i(t + \Delta t / 2) &= \vec{v}_i(t) + \frac{1}{2m_i} \Delta t \cdot \vec{f}_i(t) \\ \vec{f}_i(t + \Delta t) &= \vec{f}_i(\vec{r}_i(t + \Delta t) + \vec{v}_i(t + \Delta t / 2)) \\ \vec{v}_i(t + \Delta t) &= \vec{v}_i(t + \Delta t / 2) + \frac{1}{2m_i} \Delta t \cdot \vec{f}_i(t + \Delta t)\end{aligned}\quad (2.11)$$

where $\vec{r}_i(t)$ and $\vec{r}_i(t + \Delta t)$ are the positions of particle i at time t and time $t + \Delta t$, respectively. $\vec{v}_i(t)$, $\vec{v}_i(t + \Delta t / 2)$, and $\vec{v}_i(t + \Delta t)$ are the velocity of the particle at t , $t + \Delta t / 2$ and $t + \Delta t$, respectively. $\vec{f}_i(t)$ and $\vec{f}_i(t + \Delta t)$ are respectively the total forces on the particle at t and $t + \Delta t$.

2.4 Summary

In this chapter, a proposed general model system is described, which is used to simulate the kinetic behaviour of microtubules driven by dynein motors. In the model, microtubule is treated as a polymer chain connected by microtubule beads. Forces from its extension and bending, driving or drag force from dynein motors, and environmental forces are taken into account in the model to determine the movement of a microtubule.

The model is developed based on a driving mechanism that is schematically illustrated in Fig.2.3. This stochastic driving mechanism and various forces involved are discussed in this chapter.

Extension force and bending force are calculated based on the elastic spring force between adjacent beads and bending potential of microtubule segment, respectively. Environmental Force depending on system conditions will be discussed in following chapters.

References

1. Amos, L., A. Klug. 1974. Arrangement of subunits on flagellar microtubules. *Journal of Cell Science* 14: 523-549
2. Joward, J. 2001. *Mechanics of motor proteins and the cytoskeleton*, Sinauer Associates, Inc., Sunderland, Massachusetts
3. Huxley, A.F. 1957. Muscle structure and theories of contraction, *Progress in Biophysics and Molecular Biology* 7: 255–318.
4. Sakakibara, H., H. Kojima, Y. Sakai, E. Katayama, K. Oiwa. 1999. Inner-arm dynein c of *Chlamydomonas* flagella is a single-headed processive motor. *Nature* 400: 586-591
5. Burgess, S.A., M.L. Walker, H. Sakakibara, P.J. Knight, and K. Oiwa. 2003. Dynein structure and power stroke, *Nature* 421: 715
6. Curtiss, B.R.B.C.F., R.C. Armstrong, O. Hassager. 1987. *Dynamics of polymeric liquids*. Wiley, New York
7. Landau, L. D., and E.M. Lifshitz. 1986. *Theory of elasticity*. Boston, MA: Butterworth-Heinemann.
8. Allen, M.P., D.J. Tildesley. 1987. *Computer simulation of liquids*. Oxford University Press, New York.

Chapter 3

Dynamic modeling of unidirectional motion of single microtubule driven by linearly distributed dynein c

3.1 Introduction

As described in chapter 1, previous research work has demonstrated that microtubule can be guided to move unidirectionally driven by motor proteins. For instance, using a highly oriented polymer film functionalized with myosin subfragments [1] or kinesin [2], the success in driving actin filaments or microtubules in straight lines has been demonstrated. Suzuki and co-workers [3] reported the directional motion of actin filaments driven by aligned and immobilized myosin molecules using microlithographically-patterned resist polymers. In the presence of detergent, kinesin can be electively attached onto a glass surface, from which the photo-resist polymer has been removed, rather than on the photo-resist polymer itself [4]. In recent decades, the rapid development of advanced experimental techniques, such as atomic force microscopy, optical trap nanometry, and fluorescence microscopy, has made it possible to investigate the dynamics of proteins at single-molecule level with different time scales from millisecond to second. The high resolution of the experimental techniques permits probing conformational changes and functions of motor proteins, such as myosins, kinesins and dyneins. However, the coordination mechanism of motor proteins is still not clear. In this work, the general model was applied to simulate unidirectional movement of microtubule driven by dynein motors to analyze the effect of coordination of dynein motors on the motion of microtubule.

In this work, the general model described in Chapter 2 was applied to simulate unidirectional movement of microtubule driven by dynein motors with focus on the coordination function of dynein motors.

3.2 Model description

3.2.1 A modified model for unidirectional movement

When a microtubule move unidirectionally, it is hard to bend, thus bending force can be ignored in the model. Therefore, derived from equation (2.1), the controlled equation for microtubule bead i can be modified as:

$$\mathbf{F}_i = \mathbf{F}_{iS} + \mathbf{F}_{iD} + \mathbf{F}_{iO} \quad (3.1)$$

where \mathbf{F}_{iS} is a spring force associated with the stretching of spring connecting adjacent beads; \mathbf{F}_{iD} is a driving force generated by dynein; \mathbf{F}_{iO} is an force from environment, including viscous and thermal forces.

In the equation (3.1), as mentioned in Chapter 2, \mathbf{F}_{iD} and \mathbf{F}_{iS} can be calculated using equation (2.3) and equation (2.6). However, the environment force \mathbf{F}_{iO} is unknown in the model.

In recent years, the dissipative particle dynamics (DPD) technique [5] attracted interest due to its large time steps that markedly decrease the computing time so that the powering process of motor proteins involving many factors could be investigated. In 1992, Hoogerbrugge and Koelman proposed a simulation model based on the dissipative particle dynamics (DPD) to study the

hydrodynamic behavior of motor proteins [5, 6]. In this model, a liquid phase is modeled using dissipative particles and their motion is simulated based on some collision rules. Thermal and hydrodynamic effects could be included in the model, which are of importance to studies on the fluctuation of a microtubule. The DPD method has demonstrated its advantages in simulation of complex fluids and soft materials [7-12]. This method can provide more details of the motor protein's behavior than the stochastic model [13] or the ratchet model [14]. It should be indicated that, compared to the molecular dynamics model used by Gao, et al [15], the DPD model may be limited for qualitative prediction and explanation due to its non-conservation of energy. Since the objective of this study is to improve the understanding of the driving mechanism of dyneins on microtubule, especially to study the coordination functions of motor protein, rather than quantitative prediction, the DPD appears to be a suitable approach for the present study.

In this work, the dissipative particle dynamics (DPD) approach was adopted to represent the interaction between microtubule and surrounding environment. Thermal and hydrodynamic effects are introduced into the model. Hence, local forces and their fluctuations can be analyzed, which is of importance to understand the coordination of dynein motors during driving microtubules.

3.2.2 The DPD approach

DPD is a particle-based method [5], in which a fluid is treated as a group of interacting particles. Each particle represents a fluid element containing a

number of molecules. The interaction between two particles is a sum of conservative force, dissipative force and random force:

$$F_{iS} = \sum_{j \neq i} (F_{ij}^C + F_{ij}^D + F_{ij}^R) \quad (3.1)$$

F_{ij}^C is a intermolecular force (conservative), which is a function of the distance between two particles. F_{ij}^D is a damping force (dissipative) that is primarily responsible for the viscous effect affected by the relative velocity between a pair of particles. F_{ij}^R is a stochastic force caused by the thermal motion of molecules.

Fig.3.1 illustrates the DPD force system.

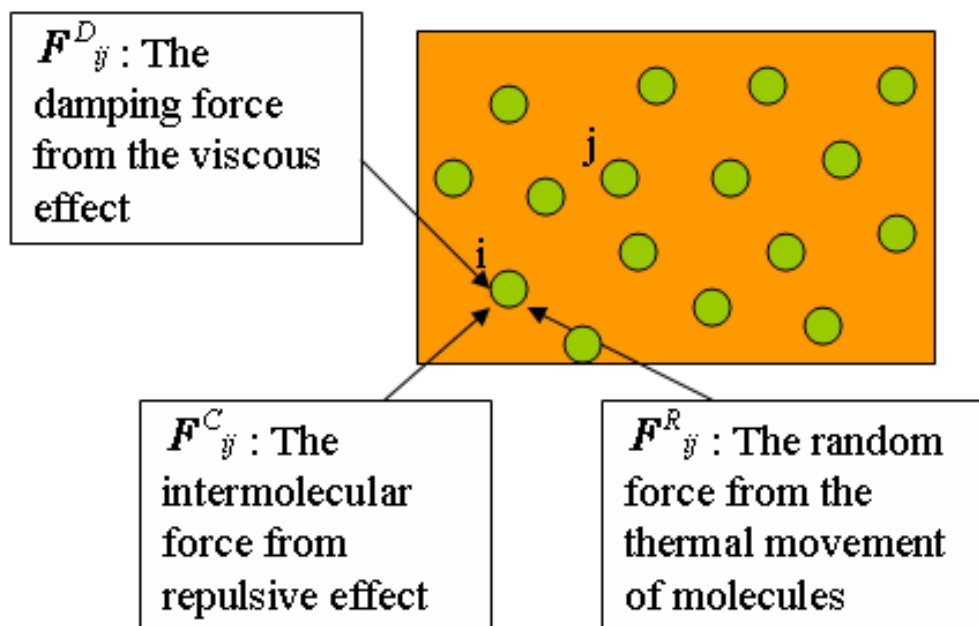


Fig.3.1 The force system for DPD approach

Since the forces are pairwise, the momentum of the entire system is conserved and its macroscopic behavior directly depends on Navier-Stokes hydrodynamics [5]. The conservative force is expressed :

$$F^C_{ij} = \begin{cases} a_{ij}(r_c - r_{ij})\hat{r}_{ij}, & r_{ij} < r_c \\ 0, & r_{ij} \geq r_c \end{cases} \quad (3.2)$$

where a_{ij} is the maximum repulsive coefficient between particles i and j, which can be determined from the liquid's compressibility; $r_{ij} = |r_i - r_j|$, r_c is a cutoff radius, and \hat{r}_{ij} is the unit vector from particle i to particle j.

For a liquid phase consisting of two different types of particles, A and B, the particle-particle interaction is approximated by letting

$$\begin{aligned} a_{AA} &= a_{BB} = a_0 \\ a_{AB} &= a_0(1 + \xi) \end{aligned} \quad (3.3)$$

A positive ξ results in a larger repulsive force between A and B, while a negative ξ leads to smaller repulsion so that species A and B can be mixed more easily. The value of ξ ranges from -0.5 to 0.5 [8].

The dissipative force and random force can be written as :

$$F^D_{ij} = -\gamma w^D(r_{ij})(\hat{r}_{ij} \cdot v_{ij})\hat{r}_{ij}$$

$$F^R_{ij} = \sigma w^R(r_{ij})\zeta_{ij}\Delta t^{1/2}\hat{r}_{ij} \quad (3.4)$$

$$\sigma^2 = 2\gamma k_B T \quad (3.5)$$

where σ is the amplitude of noise, and ζ_{ij} is a random noise term with zero mean and unit variance. γ is a friction coefficient, which is related to σ , as equation (3.5) describes. $\sigma = 3$ is recommended based on previous work [12].

It needs to be indicated that F_{ij}^D and F_{ij}^R are mutually related through w^D and w^R :

$$w^D(r) = [w^R(r)]^2 = \begin{cases} (r_c - r)^2, & (r \leq r_c) \\ 0, & (r > r_c) \end{cases} \quad (3.6)$$

For a system in equilibrium, its temperature may be determined from the velocity of particles driven by thermal force:

$$3KT = \langle mv^2 \rangle \quad (3.7)$$

3.2.3 Modeling Process

Dimensionless simulation was conducted in the study. We set $\hat{m} = \hat{r}_c = \hat{T} = 1$, where \hat{r}_c is the corresponding dimensionless diameter of a solution particle at $r_c = 100nm$, \hat{m} is the dimensionless mass of a solution particle, and \hat{T} is the dimensionless temperature at $T = 298K$. According to previous work [16], for water, $a_{ij} = 75KT / \rho$, in which ρ is a number density. $\rho \geq 3$, $\sigma = 3$ and time step $\Delta t = 0.04$ are adequate choices. Period boundary condition was applied to both vertical and horizontal dimensions.

The dynein motors were initially randomly but linearly distributed in the surface in a row and solution particles were placed at random. The initial velocities of solution particles were chosen randomly from a Boltzmann Distribution with initial system temperature at $T=298$. At each time step, velocities are scaled by a factor to maintain a constant system temperature:

$$\lambda = [1 + \frac{\delta t}{t_T} (\frac{T}{T_c} - 1)] \quad (3.8)$$

where T_c is the current kinetic temperature; t_T is a present time constant.

To test the influence of thermal force on the structure of microtubule, the system was relaxed and monitored by a related conformational time correlation function:

$$C(t) = \frac{1}{NR_g^2} \sum_1^N \langle [r_i(t) - R_{cm}(t)] \cdot [r_i(0) - R_{cm}(0)] \rangle \quad (3.9)$$

R_g^2 is mean-square radius of gyration, $r_i(0)$ and $r_i(t)$ are the original position and position in time t for bead i respectively. $R_{cm}(0)$ and $R_{cm}(t)$ are original center-of-mass of the chain and the center-of-mass in the time t .

Fig 3.2 shows the change of related conformational time correlation function with time. Only a very small change was observed, which means that the structure of microtubule was very stable during moving in the solution driven by dynein motors. Therefore, it is reasonable to treat microtubule as a straight rod without bending effect.

Since the attachment of motor proteins onto a microtubule is statistically random, the coordination among motor proteins should therefore largely affect the motion of a microtubule driven by the motors. The coordination among motor proteins is dependent on the number of motor proteins, which can affect the driving and drag forces on the microtubule and thus its mobility. In order to gain an insight into this issue, the movement of a microtubule driven by dynein c with different motor densities was simulated. The system for modeling was set

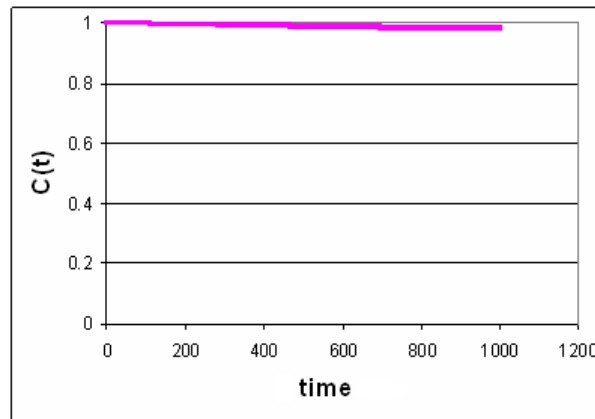


Fig 3.2 Related conformational time correlation function against time as 200×40 as shown in Fig.3.3. The length of a microtubule was set as 100, consisting of 100 beads. In order to study how the density of motor protein affected the microtubule's movement, different motor densities, which represent the number of dynein c motors per micrometer along the longitudinal direction of the system, were used in the simulation. Motors were randomly distributed in the longitudinal direction, along which the microtubule moved.

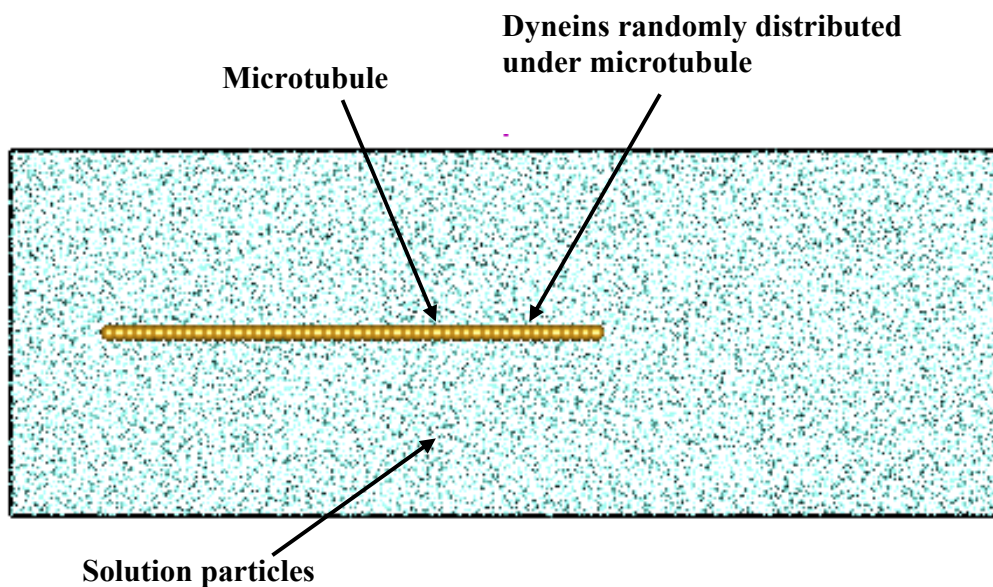
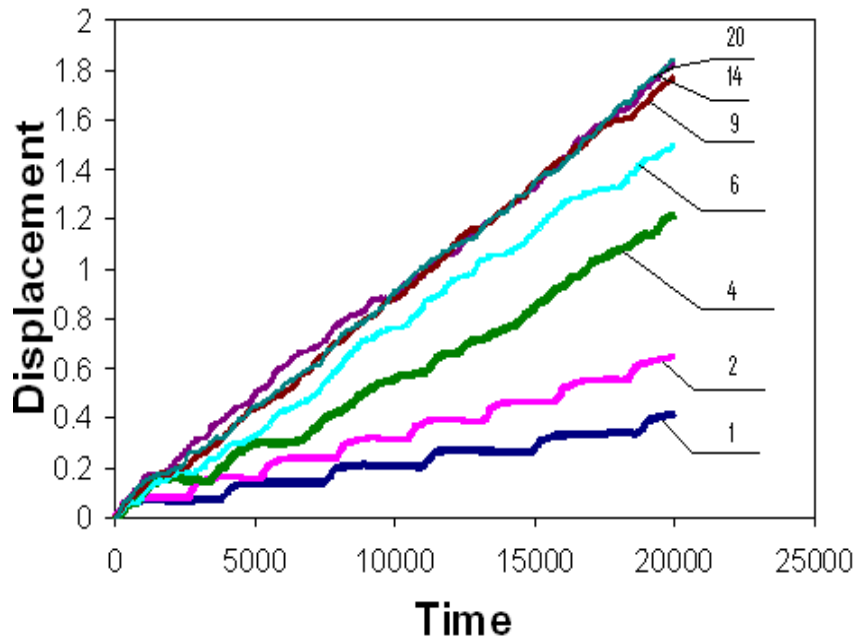


Fig 3.3 Sketch of a model system for unidirectional motion of a microtubule

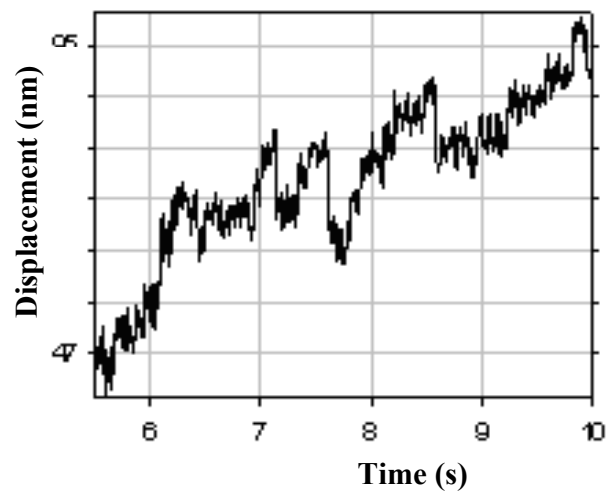
3.3 Results and discussion

3.3.1 The effect of motor density on the microtubule motility

Fig.3.4 illustrates the displacement of a microtubule along the longitudinal direction against time or time steps for different densities of dynein c (the number of dynein c motors per micrometer along the longitudinal direction of the system). As shown, when the microtubule was driven by a motor, a stepwise-curve was observed. In this case, as the motor was attached to the microtubule, it drove the microtubule to move over one step (δ) with releasing its stored energy. The motor then dragged the microtubule before it was completely detached from the microtubule. As a result, the microtubule stopped to move due to the drag from both the motor and the surrounding liquid. After an off-attaching period τ_{off} , the motor was attached to the microtubule again (in another position) and another attaching-driving-detaching cycle began. This stepwise curve was observed experimentally, as Fig.3.4 (b) illustrates [17]. Such a stepwise curve was also observed when more motors were involved; however, the curve became less stepwise. As shown in Fig.3.4 (a), the movement of microtubule becomes continuous with an increase in the motor density and the displacement \sim time curve eventually tends to be a line.



(a)

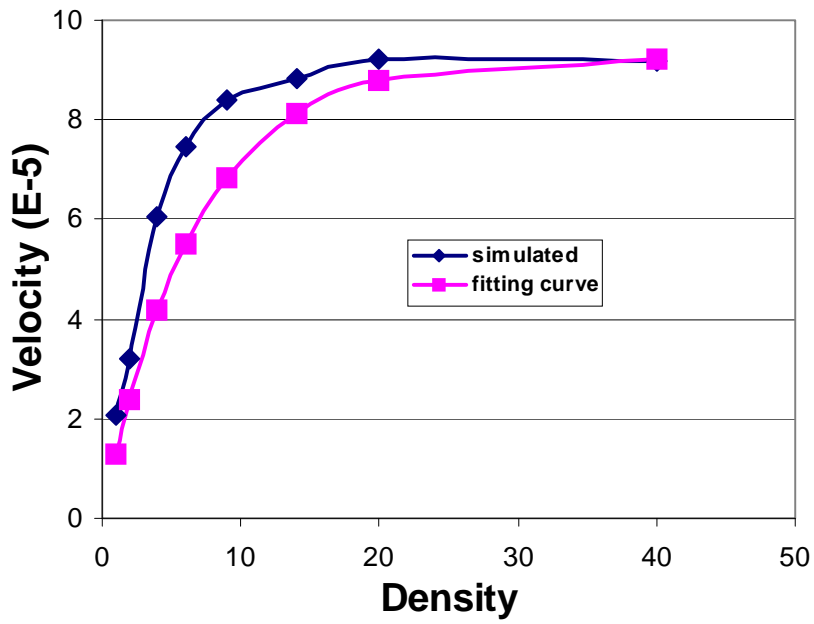


(b)

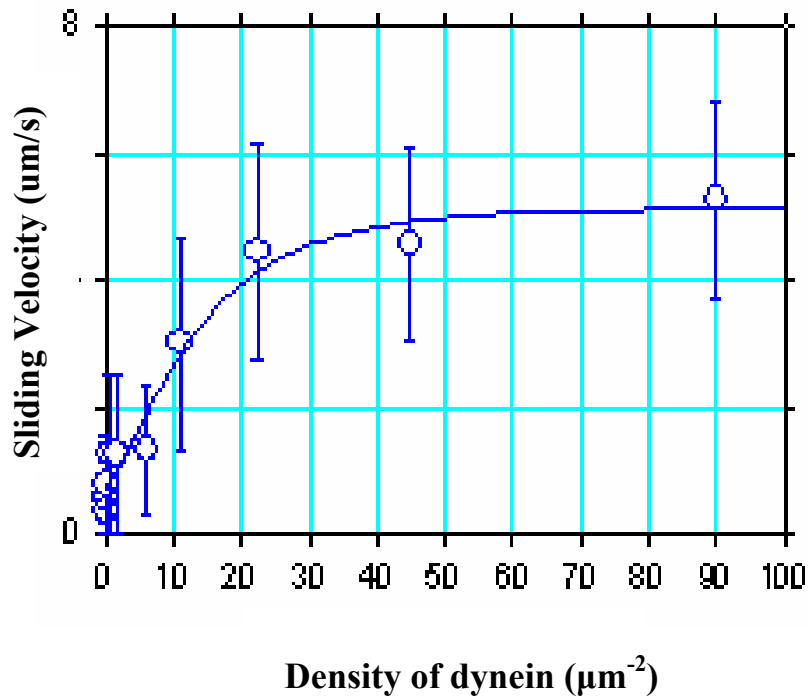
Fig.3.4 (a) The simulated displacement of a microtubule vs the time (different motor densities were used in the simulation, respectively); (b) Stepwise movement of a microtubule driven by a single dynein c [17]

The velocity of microtubule increases as the density of dyneins (the number of dynein c motors per micrometer) increases, since the time interval during which the microtubule stops to move decreases as Fig.3.4 (a) illustrates. As a result, the average velocity increases, i.e., the average slope of the curve increases. Fig.3.5 (a) illustrates the increase in velocity against the motor density. As shown, the velocity increases rapidly with an increase in the density of molecular motors until saturation when the motor density reaches a certain level. The saturation of velocity is attributed to an increase in the drag from the motors as the motor density increases, which renders the coordination among motors poor. A balance between driving and drag may eventually be reached, leading to a stable velocity when the motor density reaches a certain value, as Fig.3.5 (a) illustrates.

The relation between the velocity V_s and motor density D may be approximately represented using the following equation: $V_s = V_{s0} * (1 - (1 - 0.14)^D)$, where $V_{s0} = 9.225E-5$. Experimentally, a similar relationship was observed between the velocity and motor density: $V_{exp} = V_0 (1 - (1 - f)^N)$, where f is the duty ratio = 0.14 for dynein c and N is proportional to the motor density [17]. Fig.3.5 (b) illustrates the experimental result, which is consistent with the modeling result. The only difference is that in the experiment the motor density must reach a certain level before a microtubule starts to move. This difference between experimental observation and modeling could be attributed to the difference in scaling, bearing in mind that the modeling is dimensionless.



(a)



(b)

Fig.3.5 (a) The velocity of microtubule vs the density of motors; (b) The sliding velocity of microtubule vs the surface density of dynein c [17]

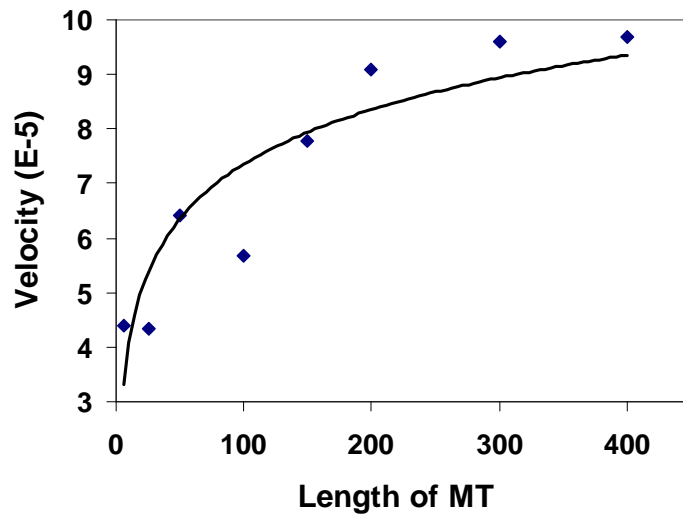
3.3.2 The length of microtubule and sliding velocity

Previous work demonstrated that the motility of microtubules was affected by its length [18], which should also influence the coordination among motor proteins. For a fixed motor density, the longer a microtubule, the lower degree should be the motor coordination. This consequently affects the microtubule's velocity. In order to elucidate the relation between the microtubule length and velocity, the motion of microtubules having different lengths driven by motors with the same density was simulated. In the model, the average motor density was fixed as 10 dynein c motors per micrometer along the longitudinal moving direction. Motors were randomly distributed in the system. In the model, microtubules having different lengths, 6, 12, 25, 50, 100, 150, 200, 300, 400, respectively (dimensionless in the simulation), were studied.

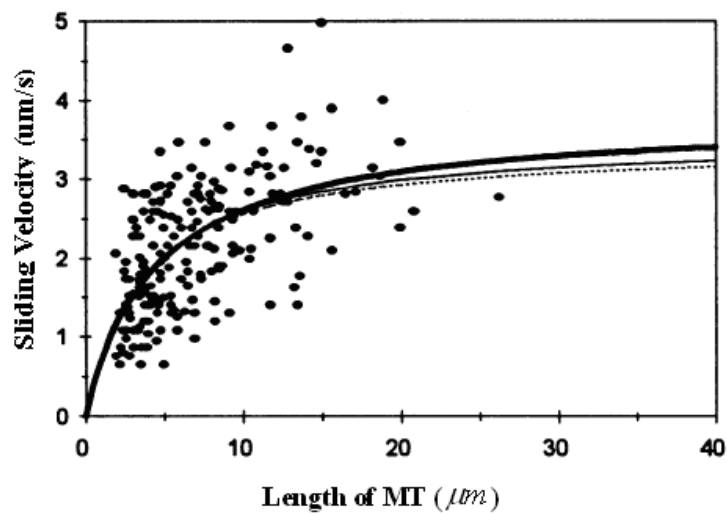
Fig.3.6 (a) illustrates the longitudinal velocity of a microtubule against its length. The velocity increased initially with an increase in the length, which became stable after reaching a critical length. Similar trend was observed in reported experiments [18] as shown in Fig.3.6 (b).

For a short microtubule, motors have low probability to attach and drive it. Hence, the microtubule should move slowly as the total driving force from motors is smaller. With an increase in the length of microtubule, more motors have the opportunity to attach and drive it with more local acceleration events associated with motor attachment, thus resulting in an increase in the velocity of microtubule. However, along with the increase in the driving force, the drag force from motors also increases, accompanied with poor motor coordination as indicated earlier.

Meanwhile, the drag force from solution increases as well due to the increased velocity and length of a microtubule. As a result, the velocity of microtubule eventually becomes saturated as the microtubule's length reaches a certain value.



(a)



(b)

Fig.3.6 (a) The simulated velocity of microtubule against its length (b) Experimentally observed sliding velocity of a microtubule against its length. (Cited from ref [18])

3.3.3 Force analysis

As indicated earlier, a microtubule may exhibit very different kinetic behaviors when driven by a single motor and a group of more motors, respectively. The higher the motor density, or the longer the microtubule, the more motors attached to the microtubule simultaneously. Therefore, understanding how motors work coordinately to drive microtubule is of importance to gain better understanding of the effect of motor density on microtubule's kinetic behavior, which is crucial to future nano-bio-mechanical systems. Obviously, the coordination of motors directly affects the driving and drag forces to a microtubule. In this study, we investigated effects of the motor density on drag force (F_{drag}) and driving force (F_{driv}). There are two net drag

forces: one from motors, $F_{\text{m_drag}} = \sum_{i=1}^{N_0} F_{\text{m_drag}}^i$ ($F_{\text{m_drag}}^i \neq 0$ when the motor i is in its period of τ_{drag}) and the other from the interaction between the microtubule and

solution particles, $F_{\text{s_drag}} = \sum_{i=1}^{N_1} \sum_{j=1}^{N_2} F_{ij}^D$. N_0 is the total number of motors, N_1 is the

number of beads within a microtubule, and N_2 is the number of solution particles.

The driving force is the total force from all motors that are attached to the

microtubule, $F_{\text{driv}} = F_{\text{m_driv}} = \sum_{i=1}^{N_0} F_{\text{m_driv}}^i \cdot F_{\text{m_drag}}^i$ and $F_{\text{m_driv}}^i$ are the drag force and

driving force from motor i . The total force (F_{total}) on microtubule is the sum of

$F_{\text{m_drag}} + F_{\text{s_drag}} + F_{\text{driv}}$.

Fig.3.7 illustrates average F_{driv} , F_{drag} , $F_{\text{m_drag}}$, and $F_{\text{s_drag}}$ with respect to the density of dynein c motors (the number of dynein c motors per micrometer). With an increase in the motor density, F_{driv} , F_{drag} , $F_{\text{m_drag}}$, and $F_{\text{s_drag}}$ increased. It is understandable that the first three forces are proportional to the motor density, since they are directly contributed by individual motors and affected by their coordination. Regarding the drag force from solution, although increased initially, it reached a stable value when the density exceeded 20. Since $F_{\text{s_drag}}$ is related to the velocity of microtubule beads relative to solution particles, it is mainly influenced by the velocity of the microtubule. As demonstrated earlier, the velocity of microtubule increased initially with an increase in motor density, associated with a corresponding increase in drag force from solution. However, the velocity of microtubule became stable when the density exceeded 20 (see Fig.3.5 (a)). Hence, $F_{\text{s_drag}}$ should also become stable when the motor density exceeds this value as Fig.3.7 illustrates.

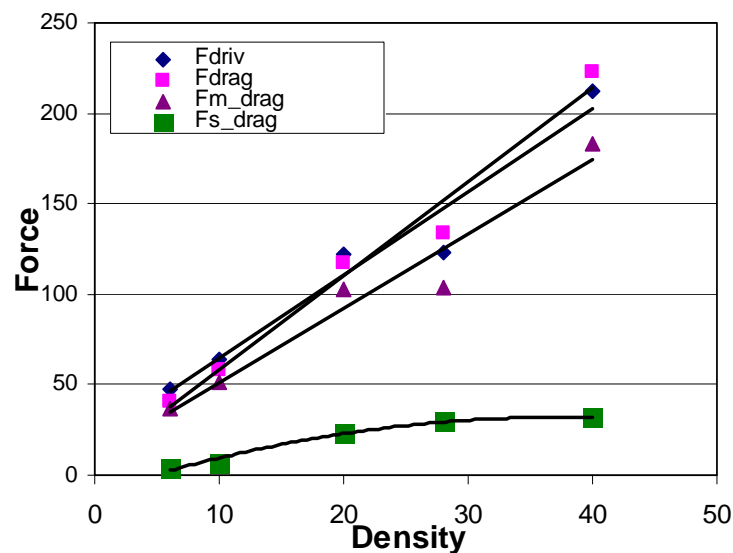


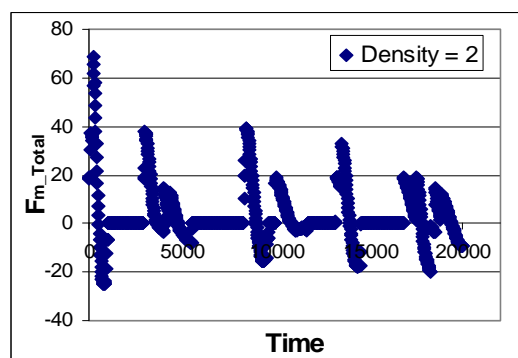
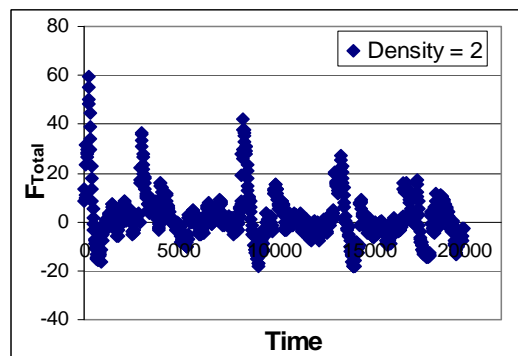
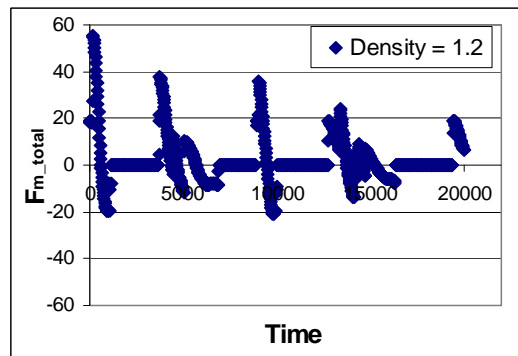
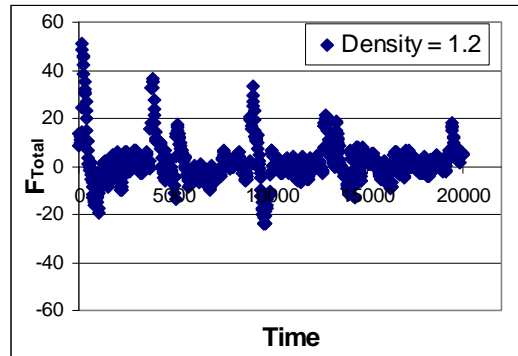
Fig.3.7 F_{driv} , F_{drag} , $F_{\text{m_drag}}$, and $F_{\text{s_drag}}$ vs the density of dynein c motors

Comparing to the drag force from solution (F_{s_drag}), the drag force from motors (F_{m_drag}), was about 8 times as large as F_{s_drag} . This implies that motors strongly affect drag force, to which the coordination among motors makes a large contribution, since the motors do not drive the microtubule harmonically. When comparing the total drag force to the total driving force, though they both increased with an increase in the density of motors, one may see that the ratio of these two forces is close to 1. This may make the microtubule moves at a constant speed.

Fig.3.8 illustrates the total force on a microtubule, F_{total} , and the total force from motors, F_{m_total} , against the time step for different densities of dynein motor. As illustrated, the total force on the microtubule fluctuated with time. With an increase in the motor density, the fluctuation frequency increased. However, the average total force for a long period was zero. This indicates that statistically a microtubule moves at a constant average speed but acceleration exists once a motor is attached to the microtubule. Such acceleration becomes less visible with an increase in the motor density.

The total force from motors, F_{m_total} , showed similar fluctuation but its average was non-zero, since the average force from motor should be non-zero in order to overcome the resistance from the solution as well as that from motor's drag when the microtubule is moving. The positive value corresponded to the driving force provided by the motor when it was attached to the microtubule, while the negative value corresponded to the drag force from the motor during the

detaching period (τ_{drag}). The fluctuation frequency became higher as the motor density increased, leading to more stable motion of the microtubule.



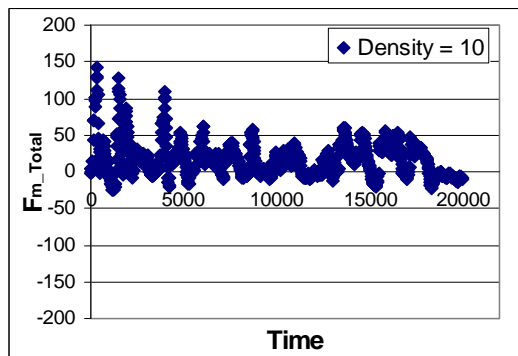
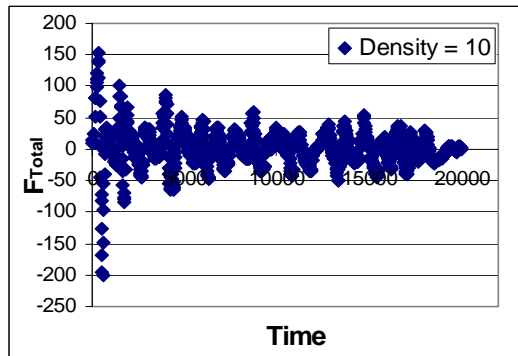
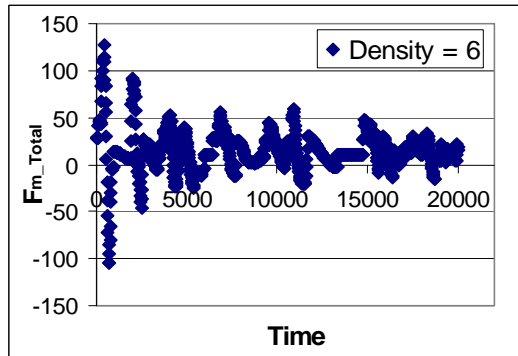
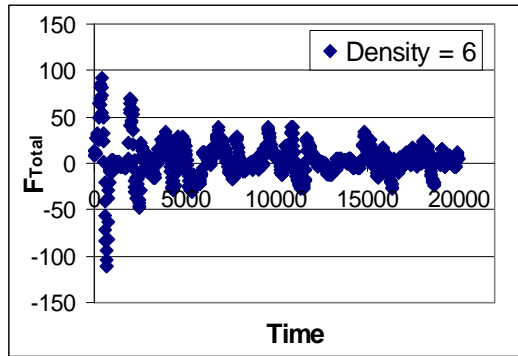


Fig.3.8 Average F_{Total} and F_{m_Total} vs the time steps for different motor densities

Effect of the coordination among motors and its influences on the driving and drag forces, average F_{driv} , F_{drag} , $F_{\text{m_drag}}$, and $F_{\text{s_drag}}$ against the length of microtubule were also investigated. As shown in Fig.3.9, with an increase in the microtubule's length, F_{drag} , F_{driv} , and $F_{\text{m_drag}}$ continuously increased. The increases in the forces are attributed to the fact that a longer microtubule can be attached by more motors that result in not only a larger average driving force but also a larger drag force due to inharmonic attachment by an increased number of motors. Besides, the resultant increase in microtubule's velocity also increased the drag force from solution.

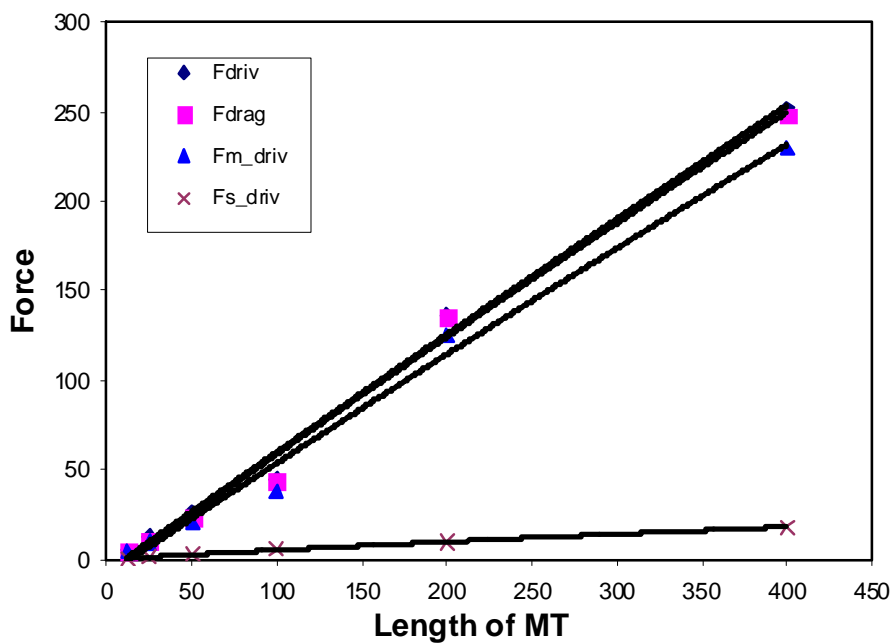


Fig.3.9 The forces F_{driv} , F_{drag} , $F_{\text{m_drag}}$, and $F_{\text{s_drag}}$ vs the length of microtubule

In summary, the present modeling study has demonstrated effects of motor density and microtubule's length on the microtubule's velocity, driving and drag forces. The coordination of motors certainly has strong influences on these parameters, which have been qualitatively demonstrated in this modeling study. It should be pointed out that in the present study, it is not attempted to establish quantitative relationships between the motor coordination and the kinetic behavior of a bio-filament driven by multiple motor proteins. To do so, it is necessary to define an adequate statistical parameter to describe the motor coordination and further quantitative investigations and statistic analysis are needed.

3.4 Movement of microtubule driven by mixed fast and slow motors

The work presented earlier was focused on the movement of microtubule driven by only one type of motors, dyneins c. What will happen if two types of molecular motor, such as dynein c and dynein f, are used to drive a microtubule? How will the microtubule's velocity and involved forces change with respect to the fractions of the two types of motor? Information on some properties of these two types of motor can be found in the literature. The attaching time (τ_{on}) of the two types of motors are similar: 1.2ms for dynein c and 1.4ms for dynein f. The two type motors have the same driving distance of a single stroke equal to 8nm. However, dynein c can drive a microtubule to move at a velocity up to $10 \mu m / s$, while dynein f can only drive it up to $2 \mu m / s$ due to a lower duty ratio of dynein f

(~0.02), compared to a much higher duty ratio of dynein c (0.14). Here the duty ratio is defined as: $\frac{\tau_{on}}{\tau_{on} + \tau_{drag} + \tau_{off}}$, which is the ratio of the attaching period to a total cycle period consisting of attaching, detaching, and off-attaching (the period that motor is detached from the bio-filament) processes.

This difference in duty ratio greatly affects the movement of a microtubule if it is driven by mixed dynein c and dynein f motors. In this work, different fractions of dynein c and dynein f were used to study the coordination among the motors with a fixed total number of motors that were randomly distributed. The observed interaction would be useful for velocity control in future nano-bio-devices.

Fig.3.10 illustrates the velocity of a microtubule with respect to the fraction of dynein c. Since the $\frac{\tau_{on}}{\tau_{off}}$ ratio of dynein f is much smaller than that of dynein c, increasing the fraction of dynein c resulted in an increase in the driving period. Hence, the velocity of microtubule increased, as shown in Fig.13. When the fraction of dynein c was higher enough, the velocity became saturated.

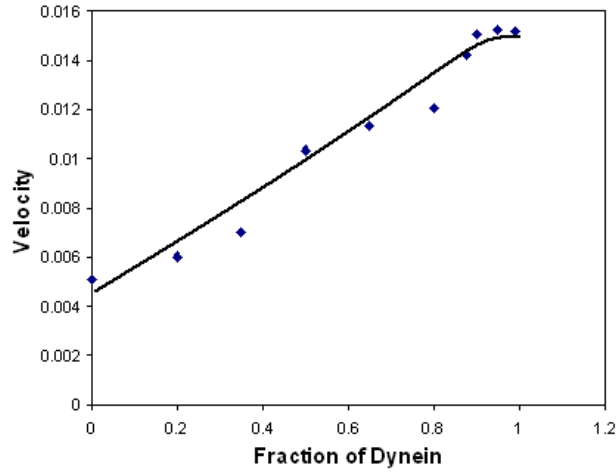


Fig.3. 10 The velocity of microtubule vs the fraction of Dynein c

In order to obtain more information related to the synergic function between the two types of motor, the driving force and drag force with respect to the fraction of dynein c were calculated. Fig.3.11 illustrates average F_{drag} , F_{driv} , and F_{m_drag} against the fraction of dynein c . As shown, with an increase in the fraction of dynein c , F_{drag} , F_{driv} , and F_{m_drag} increased and their increases gradually slowed down. F_{s_drag} also increased with the fraction of dynein c due to the increase in velocity as shown in Fig.3.11.

Since dynein c and dynein f have similar attaching time (τ_{on}) but former has a much higher duty ratio, an increase in dynein c fraction led to an increase in the total driving period. Hence, the driving force from motors increased. Meanwhile, the total drag period and thus the drag force from motors also increased with the fraction of dynein c , corresponding to the increase in the driving force on the assumption that τ_{drag} is proportional to τ_{on} ($\tau_{drag} = \tau_{on}$ was assumed in the present simulation).

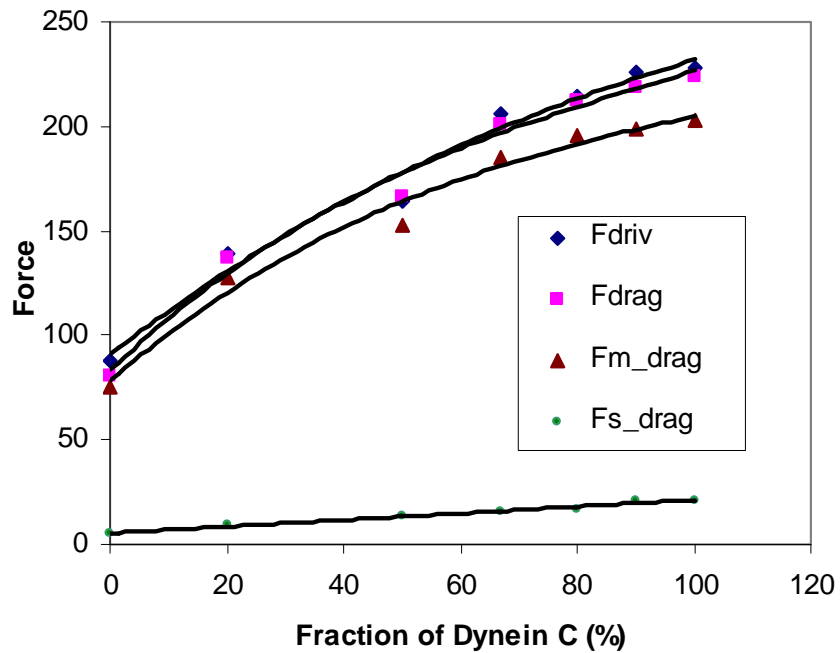


Fig.3. 11 The average force, F_{driv} , F_{drag} , F_{m_drag} , and F_{s_drag} vs the fraction of dynein c

3.5 Summary

In this chapter, the general model described in chapter 2 was extended and modified to simulate unidirectional movement of a single microtubule driven by dynein c. A dynamic method -- dissipative particle dynamic method was applied to calculate the environmental force on a microtubule, which took account of the thermodynamic and hydrodynamic behaviours of solution and microtubule. By combining with this dynamic method, the general model proposed in Chapter 2 was extended to study the driving mechanism for molecular motors attached to a

microtubule. Effects of motor's density, the length of microtubule, and the mixture of slow and fast motors on the motion of a single microtubule were studied, with the aim of demonstrating the correlation between the observed phenomena and the coordination among motor proteins.

The simulation study demonstrated that with an increase in the motor's density, the average velocity of a microtubule increased and became saturated when the motor's density was high enough. The microtubule showed a stepwise movement under the stroke of a single motor while the corresponding stair-like velocity-time curve approached a linear line with an increase in the density of motors. The microtubule's length showed a similar influence on the velocity. The computational results are in agreement with experimental observations reported in literature. The observed phenomena are greatly related to the coordination among motor proteins.

Detailed information on changes in the driving and drag forces with respect to the motor density and microtubule's length was also obtained from the modeling study. The force analysis indicated that, the average force (mean of $F_{\text{driv}} - F_{\text{drag}}$) on microtubule was approximately zero regardless of the motor density or the powerstroke frequency, which led to a macroscopically constant speed of a microtubule when it moved. However, instant acceleration existed when a motor was attached to the microtubule with a generated force to drive the microtubule. In addition, the average force from the molecular motors (average of $F_{\text{driv}} - F_{\text{m_drag}}$) was positive, which drove the microtubule to move in the solution that provided resistance to the microtubule's movement.

It was also demonstrated that when a microtubule was driven by mixed fast dynein c and slow dynein f, the microtubule's velocity showed an approximately linear increase with an increase in the fraction of dynein c; the velocity eventually reached a stable value as the fraction of dynein was above 90%.

References

1. Suzuki, H., K. Oiwa, A. Yamada, H. Sakakibara, H. Nakayama and S. Mashiko. 1995. Linear arrangement of motor protein on a mechanically deposited fluoropolymer thin-film, Japanese Journal of Applied Physics Part 1 – Regular Papers Short Notes & Review Papers 34: 3937-3941.
2. Dennis, J.R., J. Howard and V. Vogel. 1999. Molecular shuttles: directed motion of microtubules along nanoscale kinesin tracks, Nanotechnology 10: 232-236.
3. Suzuki, H., A. Yamada, K. Oiwa, H. Nakayama H and S. Mashiko. 1997. Control of actin moving trajectory by patterned poly(methyl methacrylate) tracks, Biophysical Journal 72: 1997-2001
4. Hiratsuka, Y., T. Tada, L. Oiwa, T. Kanayama and T.Q. Uyeda. 2001. Controlling the direction of kinesin-driven microtubule movements along microlithographic tracks, Biophysical Journal 81: 1555-1561
5. Hoogerbrugge, P.J., J.M.V.A. Koelman. 1992. Simulation microscopic hydrodynamic phenomena with dissipative particle dynamics, Europhysics Letters 19: 155-160
6. Koelman, J.M.V.A., P.J. Hoogerbrugge. 1993. Dynamic simulation of hard-sphere suspensions under steady shear, Europhysics Letters 21: 363-368
7. Schlijper, A.G., P.J. Hoogerbrugge and C.W. Manke. 1995. Computer simulation of dilute polymer solutions with the dissipative particle dynamics method, Journal of Rheology 39: 567-579

8. Kong, Y., C.W. Manke and W.G. Madden. 1997. Effect of solvent quality on the conformation and relaxation of polymers via dissipative particle dynamics, *Journal of Chemical Physics* 107: 592-602
9. Gibson, J.B., K. Chen and S. Chynoweth. 1998. Simulation of particle adsorption onto a polymer-coated surface using the dissipative particle dynamics method, *Journal of Colloid and Interface Science* 206: 464-474
10. Wijmans, C.M., B. Smit and R.D. Groot. 2001. Phase behavior of monomeric mixtures and polymer solutions with soft interaction potentials, *Journal of Chemical Physics* 114: 7644-7654
11. Soddemann, T., B. Duinweg and K. Kremer. 2003. Dissipative particle dynamics: A useful thermostat for equilibrium and nonequilibrium molecular dynamics simulations, *Physical Review E*. 68: 046702-2
12. Satoh, A. and T. Majima. 2005. Comparison between theoretical values and simulation results of viscosity for the dissipative particle dynamics method, *Journal of Colloid and Interface Science* 283: 251-266
13. Qian, H. 1997. A simple theory of motor protein kinetics and energetics, *Biophysical Chemistry* 67: 263-267
14. Astumian, R.D., M. Bier. 1994. Fluctuation driven ratchets: molecular motors, *Physical Review Letters* 72: 1766-1769
15. Gao, Y.Q., W. Yang, R.A. Marcus, M. Karplus. 2003. A model for the cooperative free energy transduction and kinetics of ATP hydrolysis by F1-ATPase, *Proceedings of the National Academy of Sciences of the United States of America* 100: 11339-11344

16. Groot, R.D., P.B. Warren. 1997. Dissipative particle dynamics: bridging the gap between atomistic and mesoscopic simulation, *Journal of Chemical Physics* 107: 4423-4435.
17. Sakakibara, H., H. Kojima, Y. Sakai, E. Katayama and K. Oiwa. 1999. Inner-arm dynein c of chlamydomonas flagella is a single-headed processive motor, *Nature* 400: 586-591
18. Hamasaki, T., M.E.J. Holwill, K. Barkalow, P. Satir. 1995. Mechanochemical aspects of axonemal dynein activity studied by in vitro microtubule translocation, *Biophysical Journal* 69: 2569–2579

Chapter 4

Microtubule-microtubule interactions and microtubule's collisions against micro- fabricated tracks

4.1 Introduction

As mentioned in previous chapters, *In vitro* motility assays have been frequently used to study the function of motor proteins [1-4]. In the assays, purified motor proteins are attached and immobilized on the surface of a substrate (e.g. glass surface) and counterpart cytoskeletal filaments are added onto the surface in the presence of ATP. Under a fluorescence or dark-field microscope, the movement of cytoskeletal filaments is observed and their velocities are measured to evaluate motor proteins' functions. In combination with micro-fabrication techniques, the *in vitro* motility assays have been extended to explore the application of the motor protein – biofilament system in the development of potential nano-bio-devices [5-6].

Several requirements should be fulfilled in order for motor proteins to be used in nano-bio-technological applications. For example, motor proteins or cytoskeletal filaments need to be immobilized on surfaces while keeping their activities and arranging the output of motor proteins, force and movement in one direction. In order to achieve these, one has to characterize physico-chemical properties of the surfaces for immobilization and use appropriate topography of boundaries to guide the movement of cytoskeletal filaments. The motion of cytoskeletal filaments can be confined by micro-fabricated tracks and thus guided in desired directions or patterns [4, 7-9]. When channels bordered by walls of a few hundred nanometers in height were used to confine the cytoskeletal filament movements, these filaments rarely climb up the walls. In consequence, the

cytoskeletal filaments move only in the designed channels. In fact, the success in controlling the direction of microtubule movement using simply-patterned tracks/channels [8, 9] has shortened the distance between the concept and reality for nano-bio-machine development.

Using the patterned tracks has been demonstrated to be effective in guiding all or most MTs move in one direction (rather than in both directions), which makes it possible to use the one-direction MT flow to drive components in potential nano-bio-machines, e.g., nano gears. The microtubule movement could be well controlled by optimizing the geometry of micro-fabricated patterns, which influences the bumping force, bending or rotation of microtubules when they collide with the rigid wall. Therefore, investigating the MT's collision with track wall would generate useful information for the design of optimal wall curvatures or geometry in order to guide MT movement effectively. Transport processes involving the microtubule-kinesin motility were previously modeled using a Monte Carlo simulation approach [10]. However, the mechanism for the guided MT movement has not been well characterized with sufficient detail. Besides, it was recently noticed that in *in vitro* motility assays, when two microtubules driven by axonemal dynein subspecies c (dynein c) met, they joined and moved together (either along the same direction or in opposite directions, depending on their initial moving directions) [11]. Such interaction would influence the formation of MT bundles that affects their coordinated motion and resultant driving force on nano-compounds such as nano-gears in potential nano-bio-machines, thus affecting the overall dynamic processes in the systems. However,

it remains unclear why and how two microtubules may join together. Understanding the responses of microtubules when colliding with obstacles is, therefore, of importance to the design or development of potential nano-bio-mechanical machines.

In this work, microtubule-microtubule and microtubule-wall interactions, in which microtubules were driven by axonemal dynein c, were systematically studied. The general model was modified to analyze involved mechanisms related to these two interactions. Some mechanical properties of dynein molecules and microtubules were incorporated into this hydrodynamic simulation, with which we could simulate dynamic motion of a microtubule during the collision with another microtubule or a micro-fabricated track wall. This model provides a tool to analyze the bumping force, bending moment, torque generation involved in the collision processes and associated dynamic behavior of microtubules. The obtained information is helpful for designing nano-bio-devices or systems with micro-fabricated tracks.

4.2 Experimental Analysis

The simulation study was conducted, inspired by recent experimental observations of the MT-MT collision processes. In order to conduct meaningful modeling studies, some relevant experiments were performed to provide more information for the simulation investigation, including the MT-wall collision.

4.2.1 Protein preparation

Inner-arm dynein ϵ was isolated from the outer-armless mutant of *Chlamydomonas reinhardtii* (strain *oda1*) as described in literature [12, 13]. Porcine brain tubulin, purified basically according to Vallee [14], as polymerized into microtubules in assembly buffer (80mM PIPES/KOH, 1mM MgCl₂, 1mM EGTA, 1mM GTP, 10% (v/v) dimethyl sulfoxide, pH 6.9) at 37 °C, and was subsequently stabilized by adding 10 μ M taxol. Cy5-labeled fluorescent microtubules were prepared, using the method of Howard and Hyman [15]. Dynein ϵ and tubulin concentrations were measured using the Bradford dye-binding assay.

4.2.2 Preparation of wall patterns by microfabrication techniques

In order to investigate the interaction between microtubules and a rigid wall, a wall-attack-pattern system was fabricated on glass slides (72mm \times 18mm) with electron beam lithography as shown in Fig. 4.1A. First, we deposited Nb on glass-slide surfaces by vacuum metallic deposition in order to prevent them from charging up in following processes. The SAL601-SR7 (negative electron-beam resist) layer was added by spin-coating at 4000 rpm for 90 seconds and pre-baked for 2 min on a hotplate at 85 °C for 2 minutes. We drew the wall-attack-pattern with the electron beam lithography. The patterned sample was then baked at 105°C for 2 minutes and etched with CF₄ and Ar. The wall-attack-pattern was

composed of four walls and three guiding tracks (Fig. 4.1B). The height of wall was 500 nm, which was high enough to prevent the climb-over of microtubules having their diameter of ca. 25 nm. Approach angles of the attack patterns were designed to be 15, 45, and 75 degrees.

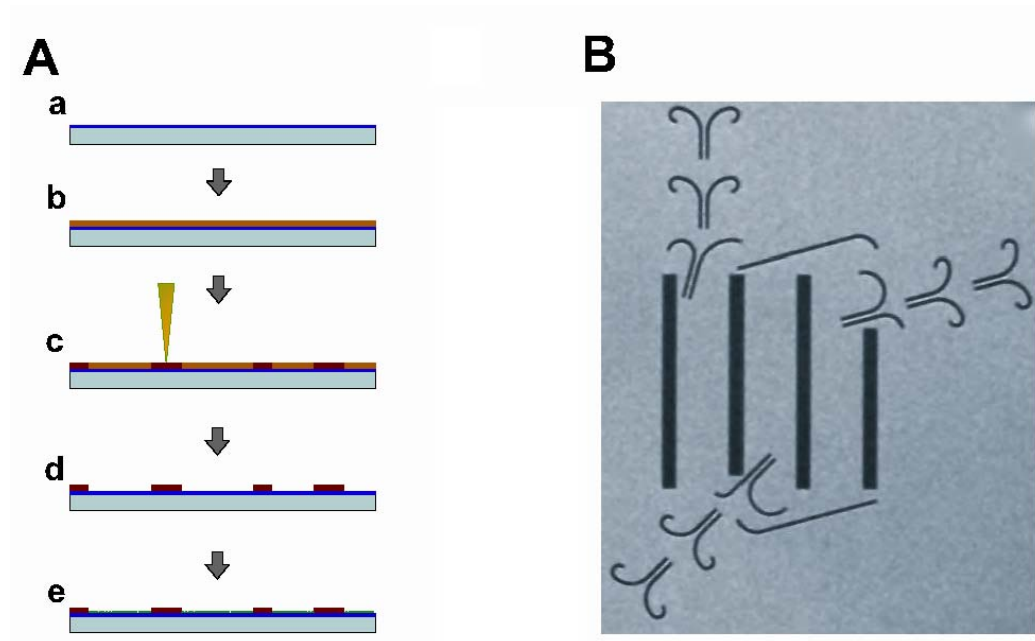


Fig 4.1 Wall-attack patterns microfabricated on a glass surface **A.** fabrication process with the electron beam lithography. **B.** fabricated wall-attack-pattern system having three approach angles

4.2.3 In vitro motility assays

For comparison with previous experimental studies [13], *in vitro* motility assays were carried out at 20-22 °C. A flow cell was made of a fabricated glass

slide or a non-fabricated glass slide (72 mm × 18 mm), and a cover slip (18 mm × 18 mm) cleaned with non-ionic detergent and rinsed with de-ionized water. Two slivers of a polycarbonate film with 50 μm in thickness were used as spacers of the flow cell (10 μl in volume). Dynein c (100 μg/ml) was diluted in a buffer solution containing 30 mM HEPES/KOH (pH 7.4), 5 mM MgSO₄, 1 mM DTT, 1 mM EGTA, and 0.5 mg/ml bovine serum albumin. The flow cell was flushed with 10 μl of the diluted dynein solution, incubated for 5 min and then washed. Solution (20 μl) containing 40 μg/ml Cy5-labelled microtubules, 0.5 mM ATP, and 1 mM DTT was introduced into the flow cell. The densities of dyneins were calculated from the concentration of dynein (molecular weight = 540kD for dynein c) and the geometry of the flow cell. We assumed that subspecies distributed evenly on the glass surface. Microtubules were visualized under an Olympus epi-fluorescence microscope using a 100 W mercury light source. The image was projected onto an EM-CCD camera (C9100, Hamamatsu Photonics) and processed by the contrast enhancement and offset controls. Images were directly stored on a hard disc for subsequent image analysis.

4.2.4 Experimental observation

A. The behavior of microtubules at collision against another microtubule

In our experimental condition, the surface density of dynein molecules was estimated to be 2000 molecules/μm², which is the saturated density. At this

density, the movement of microtubules driven by dynein c was observed all over the surface, which was constant and smooth. The measured velocity of a sliding microtubule was $6.7 \pm 1.1 \mu\text{m/s}$ ($n = 16$), which is comparable to those measured in previous studies [12]. No significant difference between motilities on both surfaces was observed.

Microtubules on the dynein-c-coated surface randomly moved in various directions and collided with each other when met. The behavior of the microtubules after collision can be categorized into four types: a microtubule 1) changed its moving direction, joined the other and then moved together in the same direction (Fig. 4.2A), 2) changed its direction of movement, joined side by side and then moved in opposite direction (Fig. 4.2B), 3) paused (Fig. 4.2 C), and 4) crossed over the other (Fig. 4.2 D). The joining, pausing and crossing occurred at the probabilities of 70%, 10% and 20%, respectively, of the total collision events (Total 393 observations). These probabilities depend upon the surface densities of dynein molecules (data not shown). In a rare case, two microtubules collided at both tips and changed both directions and traveled side by side. This case should be categorized into the case 1.

In the microtubule joining process, the tip of a microtubule (MT1) hits another microtubule (MT2) laterally and MT1 gradually changes its direction and finally moves along with MT2. The trailing part of the microtubule does not follow the trajectory drawn by the leading tip but shows lateral shift.

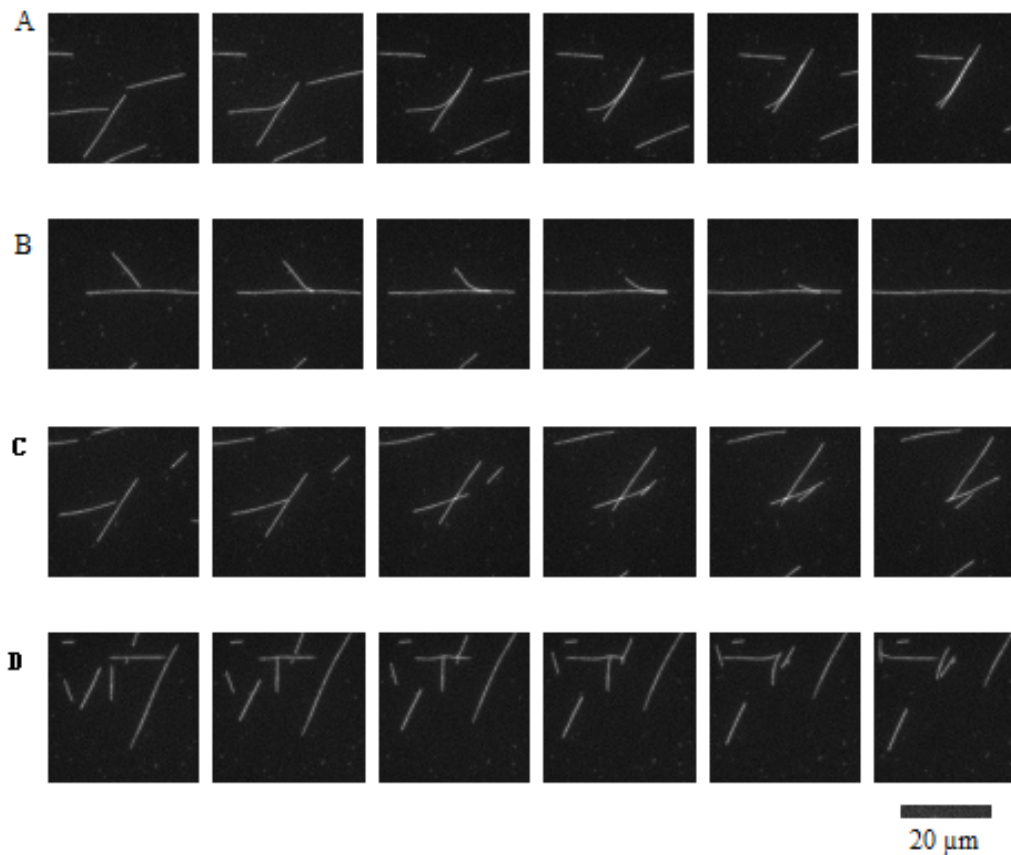


Fig 4.2 Video sequences showing the movement of a microtubule after colliding with another one. Time interval of the successive video images is $2/8$ sec. Microtubules moved on dynein-c coated glass surface at the surface density of $3300 \text{ molecules}/\mu\text{m}^2$ in the presence of $500 \mu\text{M}$ ATP at 20°C . The surface density was estimated by assuming all dynein molecules introduced into a flow cell bound to the glass surface of the flow cell. **A.** A microtubule bumped against another, joined to the latter and moved in parallel. **B.** A microtubule bumping against another joined and moved in the opposite direction. **C.** A microtubule intersected another without changing the direction of motion. **D.** A microtubule bumped against another and stopped. Scale bar is $20 \mu\text{m}$.

B. The behavior of microtubules at collision against a rigid wall

Fig. 4.3 illustrates the microtubule-wall joining processes for long (~20 μm) and short (~10 μm) microtubules with an approach angle of 45°. Different from microtubule-microtubule joining, microtubules at collision against a rigid wall always joined with the wall (20 events observed). In movement of a short microtubule at the 45° collision, the tip of the microtubule moved along the wall but the rest of the microtubule did not follow the trail. In consequence, the microtubules rotated around a point on the surface during the microtubule-wall joining process. For short microtubules, bending was rarely observed and rotation played a dominant role in this process (Fig. 4.3 A). For longer microtubules, bending was clearly observed (Fig. 4.3 B).

In microtubule-wall collision or joining processes with the larger approach angle of 75°, microtubules sometimes show a certain degree of buckling. The collision point of the microtubule seems free to pivot but does not move along the wall. The force generated by dynein molecules compressed the microtubule and exceeded the c (not necessary to show this figure, since buckling cannot be seen anyway). This buckling changes the angle between the microtubule tip and the wall, and then allows the microtubule to move its tip along the wall and finally the buckling was released.

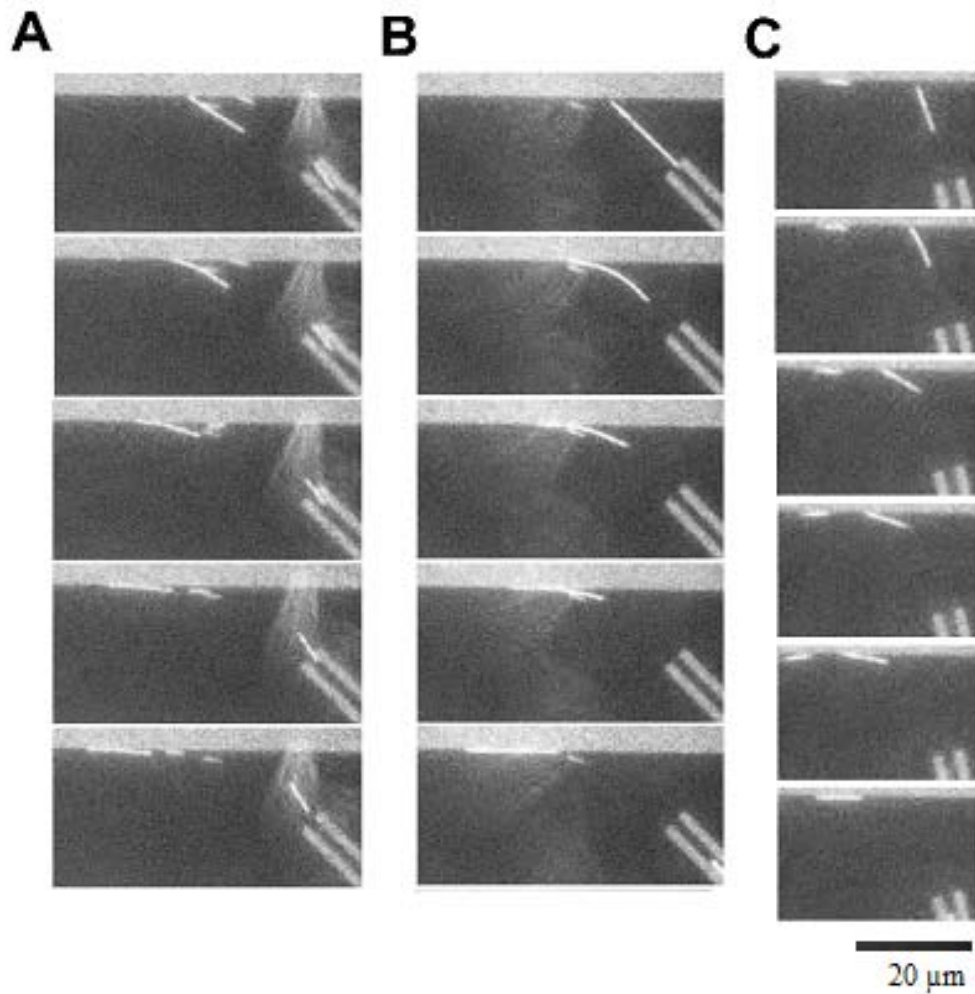


Fig. 4.3 Video sequences showing the movement of microtubules after bumping against a constraint wall. Time interval of the successive video images is $3/8$ sec. Microtubules moved on dynein-c coated glass surface at the surface density of $2400 \text{ molecules}/\mu\text{m}^2$ in the presence of $500 \mu\text{M}$ ATP at 20°C . The surface density was estimated by assuming all dynein molecules introduced into a flow cell bound to the glass surface of the flow cell. The illustrated microtubule-wall joining processes include: **A.** a bumping process of a short microtubule with a 45° bumping angle; **B.** a bumping process of a longer microtubule with a 45° bumping angle; **C.** a bumping process of a microtubule with a 75° bumping angle. Scale bar is $20 \mu\text{m}$.

4.3 Theoretical Study

4.3.1 Theoretical modeling of the behavior of microtubules

Microtubule joining is a complex process, which is influenced by many factors, e.g., drag force from solution, flexural rigidity of the microtubule, surface density of dynein molecules and the approach angle. The mutual influences of these factors make it difficult to determine the roles that the factors play in the joining process. Computer modeling allows performing “computational experiments” under controlled conditions. The effect of each parameter on a joining process could thus be tested and studied separately. Thus, the computer modeling provides an effective method complementary to experimental studies for fundamental understanding of possible mechanisms for the microtubule joining and provides guidelines for designing nano-bio-devices.

In the study reported in chapter 3, we incorporated a DPD technique with the general model system proposed in chapter 2, to analyze the function of motor proteins on the unidirectional movement of a single microtubule. The DPD technique has its advantage in local force analysis. The thermal force is taken into account in the model system. However, it takes too much time to compute the trajectories of solution particles, which limits its application in simulating larger systems with multiple microtubules and thousands of dynein motors. Therefore, in the present modeling, a more applicable approach was incorporated with the general modeling system to simulate the joining process between two microtubules and that between a microtubule and a rigid wall.

Different from unidirectional movement of a microtubule, the bending of a microtubule plays a key role in microtubule joining. Therefore, bending force should be considered in the model. The solution was treated as a continuous fluid; the viscosity force was averaged and thermal force was ignored in the model. In the model, the collision force between two microtubules is considered. A microtubule is constructed with a set of beads with a certain mass (Fig. 4.4). Each bead is the center of a segment of the microtubule and is connected with adjacent beads by elastic springs or bars that may extend, contract and rotate under external or internal forces. The motion of microtubule is driven by dyneins and influenced by surrounding solution. As a two-dimensional model, the torsion of microtubule is ignored. The motion-controlled equation for *ith* bead is expressed as:

$$m_i \frac{d^2 s_i}{dt^2} = F_{iT} = F_{iS} + F_{iB} + F_{iD} + F_{iV} + F_{iM} \quad (4.1)$$

where F_{iT} is the total force exerted on bead *i* at time *t*; F_{iS} is a force associated with the stretching of the elastic bar connecting adjacent beads; F_{iB} is a bending force on the segment represented by the *ith* bead; F_{iD} is a driving force generated by the motor proteins; F_{iV} is a viscous force exerted by the fluid on the *ith* bead; F_{iM} is a collision force between the microtubule bead and the beads of another microtubule when the two microtubules bump each other.

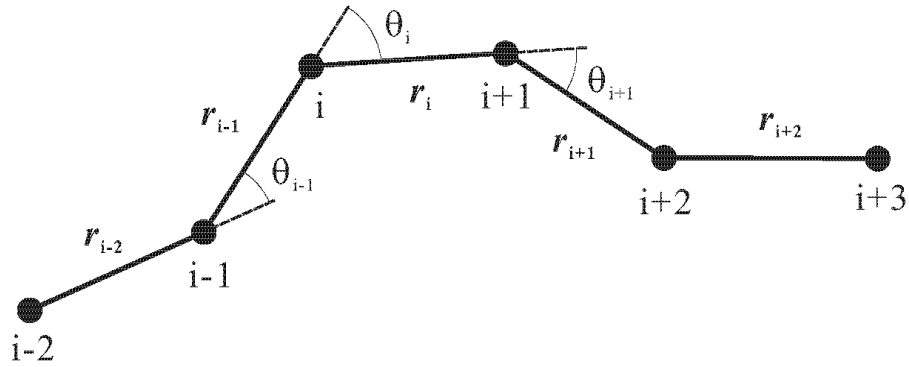


Fig. 4.4 A microtubule is constructed with a set of beads with a certain mass

In Chapter 2, the calculation of the longitudinal spring force between two microtubule beads connected by an elastic bar, F_{iS} , the bending force of microtubule, F_{iB} , and the driving force from dynein motors, F_{iD} , has been described in details. However, the viscous drag force and collision force involved in the present modeling need to be determined, details of which are provided below.

A. Viscous drag force

When a microtubule moves in a solution, there is a resistant force from the solution. The viscous force from the solution depends on the structure of a microtubule, its velocity and properties of the solution. For each segment of microtubule, it is treated as a cylinder. Fig. 4.5 illustrates viscous forces on a microtubule segment. The drag force (or viscous force) on microtubule bead i may be expressed as:

$$F_{iL} = C_{iL} \cdot L_i \cdot V_{iL}$$

$$F_{iV} = C_{iV} \cdot L_i \cdot V_{iV} \quad (4.2)$$

where F_{iL} and F_{iV} are viscous forces parallel and perpendicular to segment i , respectively; C_{iL} and C_{iV} are corresponding parallel and perpendicular drag coefficients, respectively; L_i is the length of segment i ; V_{iL} and V_{iV} are velocity of segment i in parallel and vertical directions, respectively.

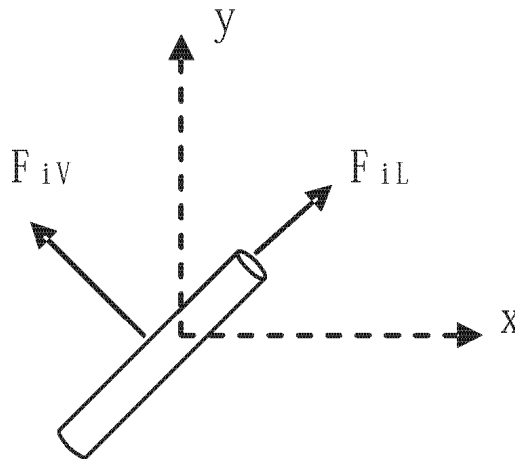


Fig. 4.5 The viscous force of a microtubule segment

Since microtubule moves in the vicinity of the glass surface, the drag coefficient for a cylinder in a solution near a plane surface is much larger than that in an unbounded solution or in a region that is far away from the surface. According to Hunt et al [16], the drag coefficients of segment in its parallel and vertical directions may be expressed as:

$$C_{iL} = \frac{2\pi\eta}{\cosh^{-1}(h/r)} \approx \frac{2\pi\eta}{\ln(2h/r)}$$

$$C_{iV} = 2C_{iL} \quad (4.3)$$

where h is the vertical distance of the center of cylinder to the glass surface; r is the radius of cross-section of cylinder; η is the viscous coefficient of cylinder in solution.

By transforming back to original (x, y) coordination, the forces in x and y directions generated by viscous forces are:

$$\begin{aligned} F_{iVX} &= F_{iL} \cdot \cos(\theta_i) - F_{iV} \cdot \sin(\theta_i) \\ F_{iVY} &= F_{iV} \cdot \cos(\theta_i) + F_{iL} \cdot \sin(\theta_i) \end{aligned} \quad (4.4)$$

B. Collision force

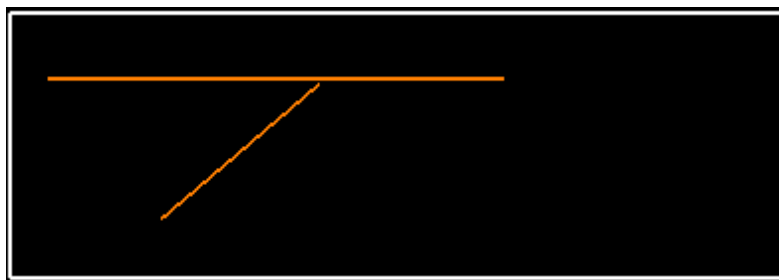
When two microtubules meet each other, a collision force is generated. In the model, the collision force between two beads respectively on the two contacting microtubules depends on the distance between the two beads. For bead i on a microtubule, the collision force from bead J on another microtubule may be expressed as:

$$\begin{aligned} F_{i,J,M} &= \beta \cdot (r_d - r_{ij}) \quad \text{if } r_{ij} < r_d \\ F_{i,J,M} &= 0 \quad \text{if } r_{ij} > r_d \end{aligned} \quad (4.5)$$

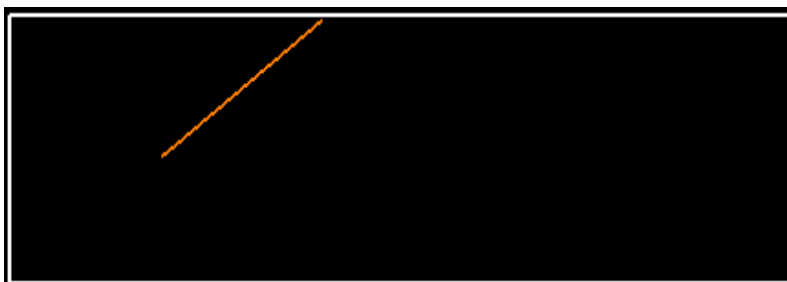
where r_{ij} is the distance between bead i and J , r_d is a equilibrium distance, which is a distance between the bead i and J without force. The collision force is equal to zero when $r_{ij} > r_d$. β is a collision coefficient, which is related to the physical properties of microtubule. In the model, we set $r_d = 25$ nm and $\beta = 100$ N/m.

4.3.2 Simulation process

The system for modeling microtubule-microtubule joining consisted of two microtubules, one moved horizontally while another moved with a specific angle to join it (Fig. 4.6 a). For microtubule-wall joining, the model system included a microtubule and a rigid wall (Fig. 4.6 b). The system size was $40\mu\text{m} \times 20\mu\text{m}$. The density of motor protein dynein c was $2500/\mu\text{m}^2$. For simplicity without losing physical significance, water was used as the solution and dyneins were randomly distributed on the bottom surface. A segment of microtubule was set as 400nm.



(a)

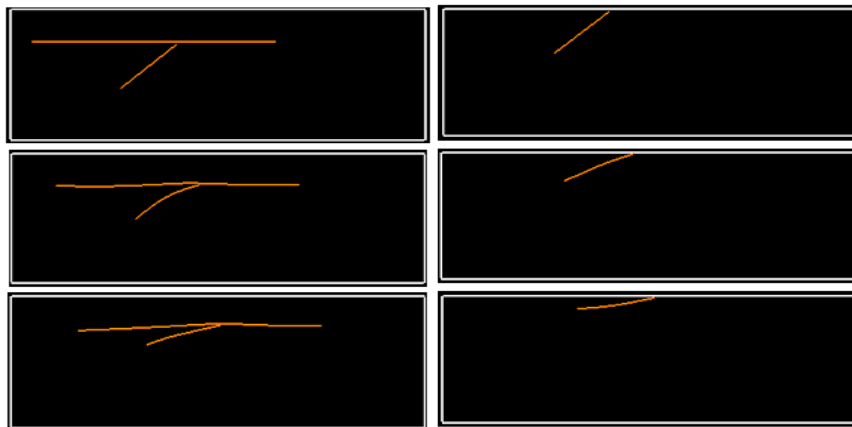


(b)

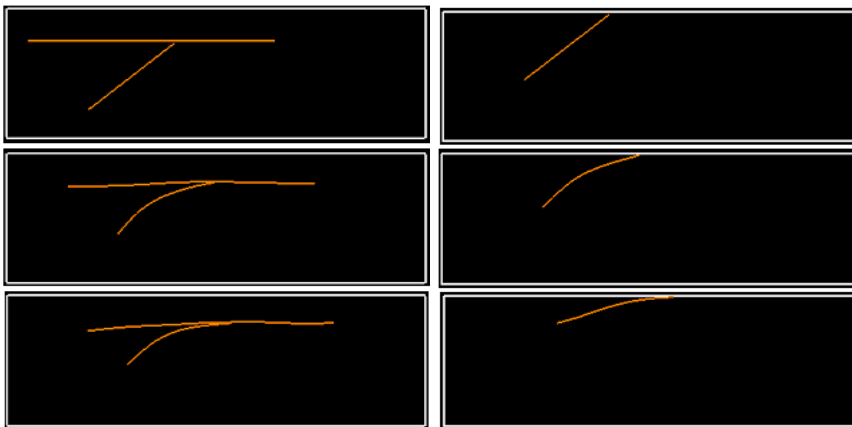
Fig. 4.6 Sketches of two model systems: (a) for modeling microtubule-microtubule joining; (b) for modeling microtubule-wall interaction

4.3.3 Simulation result analysis

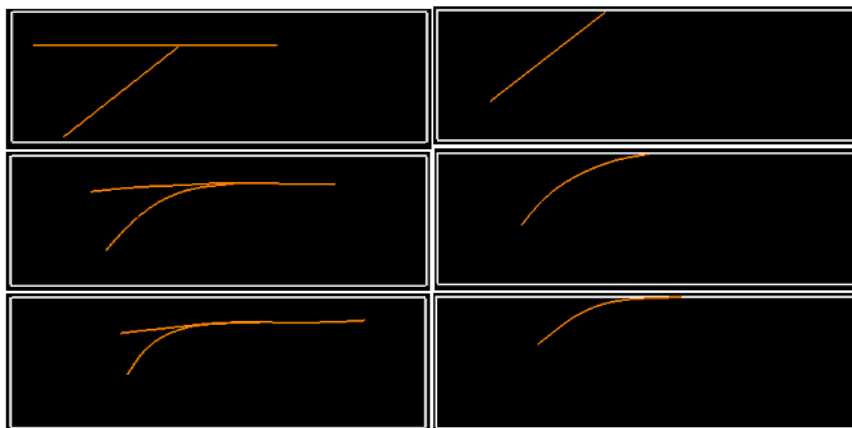
Effects of the microtubule length on microtubule-wall and microtubule-microtubule interactions were studied by computational simulation. Experimental observations demonstrated that the length of a microtubule greatly affected a microtubule-wall joining process but had little effect on a microtubule-microtubule joining process. Fig. 4.7 illustrates simulated microtubule-microtubule joining and microtubule-wall interaction processes with an approach angle 45° for microtubules having lengths of 8, 12 and 16 μm , respectively. Consistent with experimental observations, for all three microtubule lengths, microtubule bending appeared to dominate the microtubule-microtubule joining process while rotation became more obvious in the microtubule-wall joining process. During microtubule-microtubule joining, bending appeared to dominate the joining process and the microtubule length showed little effect on rotation, although there was some rotation for the short microtubules. However, for microtubule-wall joining, rotation was predominant particularly for the short microtubules. With an increase in the microtubule length, bending started to participate in the joining process.



MT-MT joining (a) MT-Wall joining



MT-MT joining (b) MT-Wall joining



MT-MT joining (c) MT-Wall joining

Fig. 4.7 Microtubule-microtubule and microtubule-wall joining processes with a bumping angle = 45° for different microtubule length: (a) length = $8 \mu m$, (b) length = $12 \mu m$, (c) length = $16 \mu m$

Fig. 4.8 illustrates two joining processes with approach angles of 15° and 45° , respectively. For microtubule-microtubule joining, the increase in the approach angle did not affect the bending of microtubule, which dominated the joining processes. For microtubule-wall joining, both bending and rotation played roles in controlling the joining process. The simulation results are well consistent with experimental observations.

When a dynein motor is attached to a microtubule, (a) it generates a power-stroke that drives the microtubule to move forward, and (b) it drags the microtubule after consuming its energy obtained from ATP hydrolysis (before detached from the MT). The latter restricts bending and rotation of microtubule. At a certain density of dynein, the number of dynein motors that are attached to the microtubule will increase with the microtubule length. Such an increase does not affect the flexibility of a microtubule during bending since the average distance between two adjacent dynein motors attached to the microtubule is constant. However, the rotation of microtubule will be largely influenced. More dynein motors attached to a microtubule would apply greater constraint to the microtubule, since the rotation occurs not only for a few segments, but for the entire microtubule. This could be the reason why the bending became dominant with an increase in the microtubule length during microtubule-wall joining.

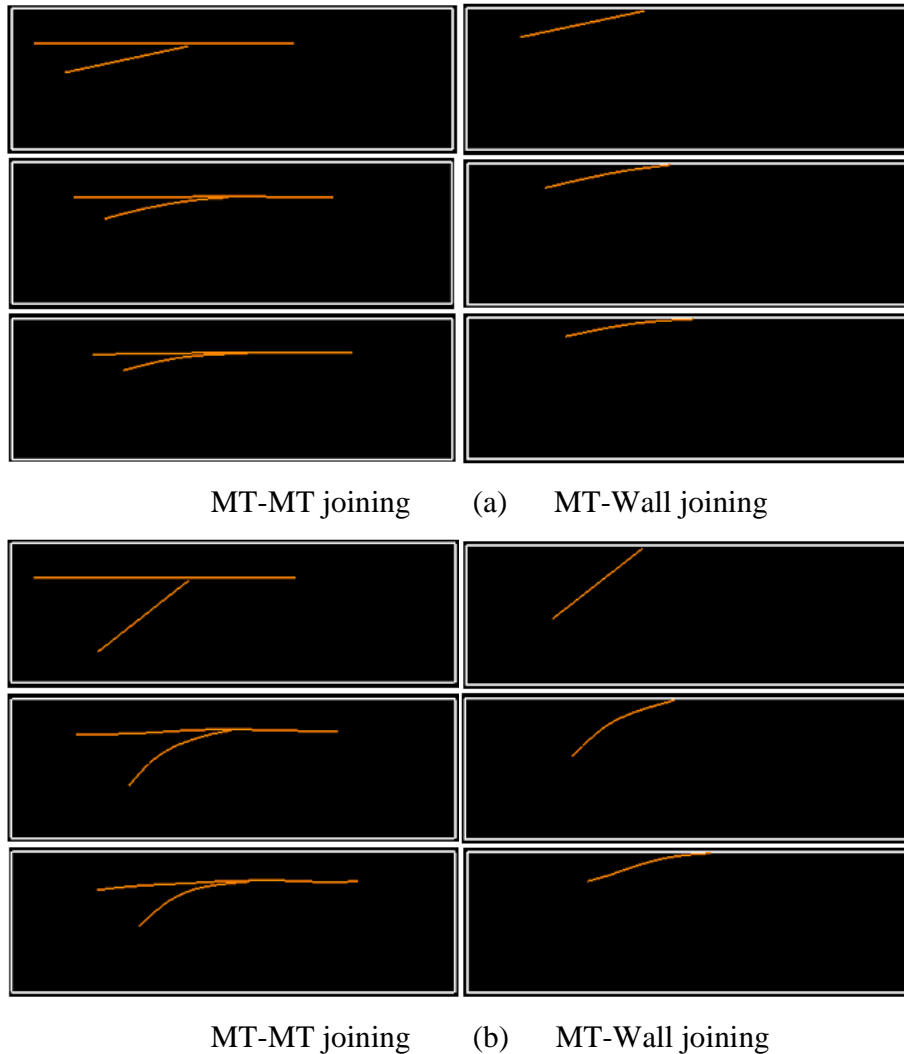
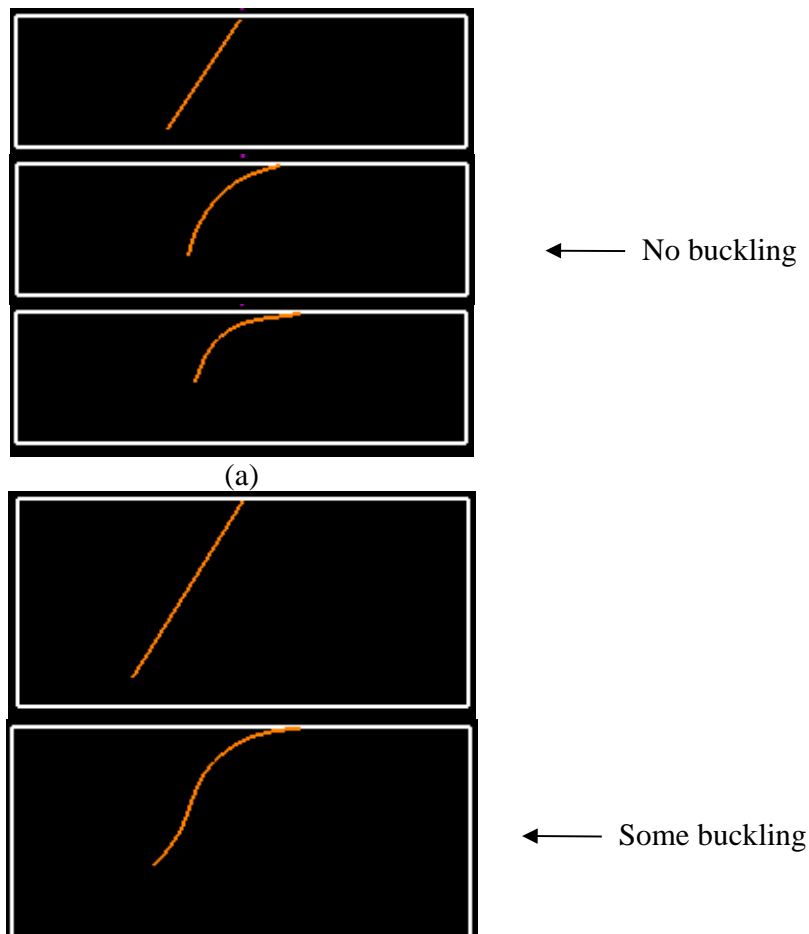


Fig. 4.8 Microtubule-microtubule and microtubule-wall joining processes with microtubule length = $12 \mu m$ for (a) bumping angle = 15° , and (b) bumping angle = 45°

Buckling may also affect microtubule joining. When increasing bumping angle, buckling may occur since collision force along axial direction of microtubule increases, which may affect the bumping process of microtubules. Normally, buckling is largely influenced by external load and microtubule length. Therefore, in this work, bumping processes with different microtubule lengths of

16, 24 and 32 μm and bumping angle at 60° were simulated. Fig.4.9 illustrates the bumping processes. For a microtubule with 16 μm length, only bending was observed without buckling. For a 24 μm microtubule length, an obvious buckling showed up during bumping process. Such buckling disappeared and only bending was observed when a part of microtubule joined with wall. With further increase of the microtubule length to 32 μm , obvious buckling was still observed. Such buckling increased with further joining. This phenomenon demonstrated that the microtubule length did affect microtubule buckling and then the bumping process. An increase in microtubule length leads to an increase in buckling.



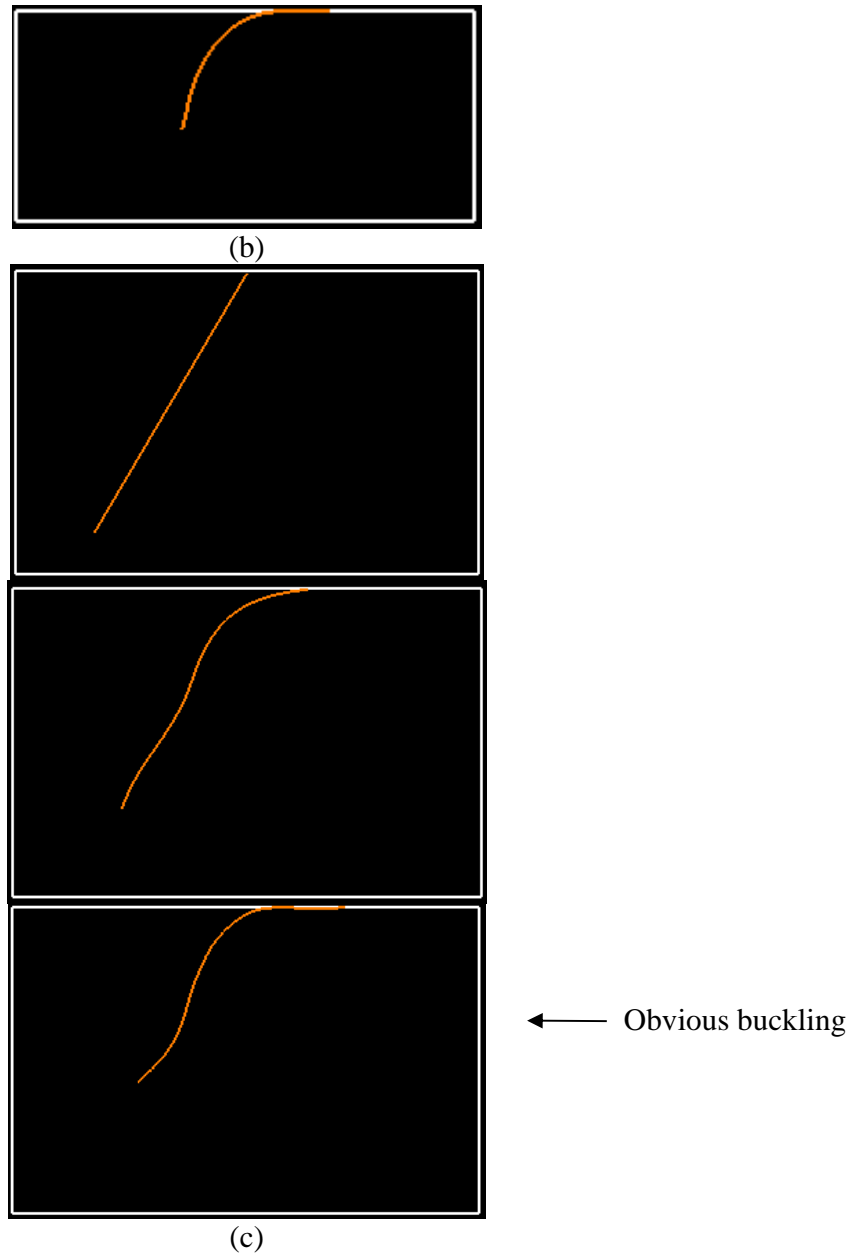


Fig.4.9 The bumping processes of microtubule with different length: (a) length = $16 \mu m$, (b) length = $24 \mu m$, and (c) length = $32 \mu m$

Bumping processes with different bumping angles at 45° , 60° , and 75° were also simulated to study the effect of bumping angle on buckling of joining process. As Fig.4.10 illustrates, with an increase in the microtubule bumping

angle, buckling becomes more obvious. With a larger bumping angle, a larger axial load from collision force will be generated, which leads to an increase in buckling of microtubule during joining process with a rigid wall.

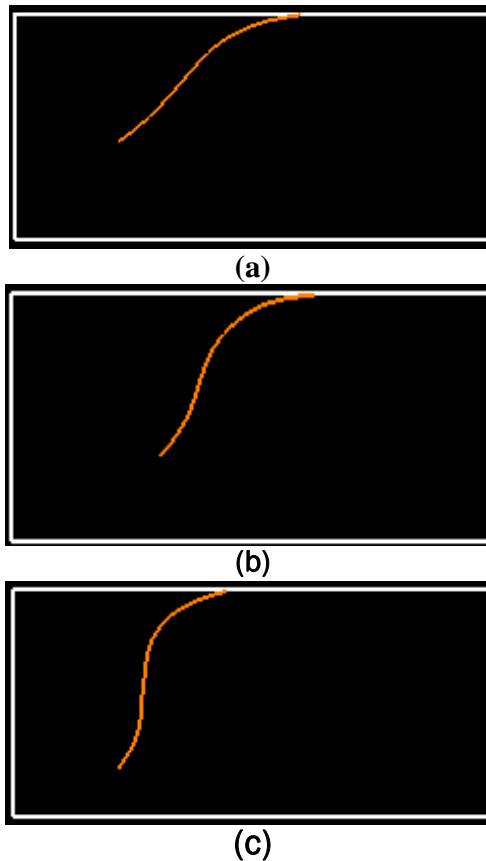


Fig.4.10 The bumping processes of microtubule with different bumping angles: (a) bumping angle = 45° , (b) bumping angle = 60° , and (c) bumping angle = 75° ,

Another parameter that affects microtubule joining is the bumping force, which is generated when a microtubule hits another microtubule or a rigid wall. The force can be divided into two force components, one is a resistant force parallel to the moving direction of microtubule, and the other is perpendicular to the moving direction, which generates a torque on the microtubule. This force

component makes the microtubule bend or rotate. If there are no dyneins attached to the microtubule, it will rotate easily without bending. If the microtubule is attached by dyneins, the motor proteins will restrict the rotation of microtubule so that the bumping torque will mainly cause local bending. For microtubule-microtubule joining, the bumping torque force for the microtubule is smaller since its counterpart is soft. The direction of bumping force will also be changed. For microtubule-wall joining, since the wall is rigid, a much larger bumping force or torque will be generated between the microtubule and wall.

In order to better understand the effects of these parameters on microtubule-microtubule and microtubule-wall joining processes, which is useful to the design of track patterns for better control of MT movement, a quantitative analysis was made and results are presented in the following sections.

4.4 Quantitative analysis of two joining processes

4.4.1 The definition of quantitative parameters

Two quantitative parameters, bending distance and instant torque, were used to reflect bending and rotation of a microtubule.

A. Definition of bending distance

As Fig.4.11 illustrates, during bending, the distance between front end (B) and distal end (A) of a microtubule decreases. CD represents the maximum distance from the points on curve ACB to line AB, which is called as bending

distance. The larger the degree of bending, the greater is the bending distance. Therefore, the distance CD can be used to represent the bending extent of a microtubule.

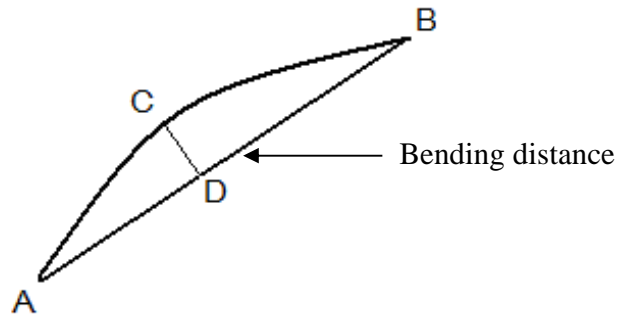


Fig. 4.11 The sketch of microtubule bending

B. Definition of instant torque

An instant torque is the total torque exerted on the microtubule at a specific moment, which includes the torque generated by bumping force and the drag force from dyneins. Normally, a larger instant torque of microtubule results in greater rotation of the microtubule at next time step. Fig.4.12 illustrates a model for calculating the instant torque. A microtubule is treated as a polymer chain composed of N segments.

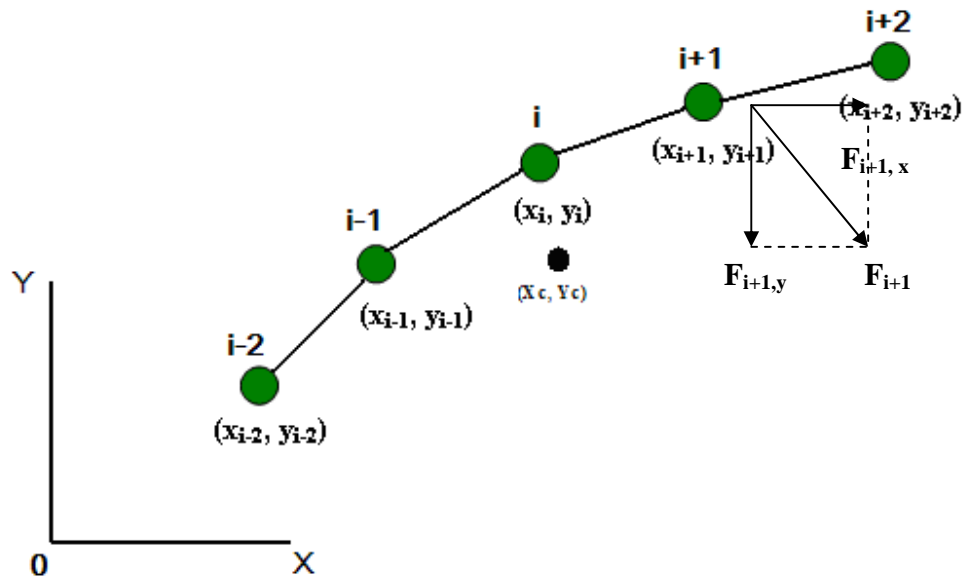


Fig. 4.12 Sketch of a bended microtubule chain

The mass of each segment concentrates on its center. These centers are treated as beads connected by strings. The position for bead i is (x_i, y_i) and its mass is m_i . The total mass of microtubule is m_t . The mass center of the microtubule (X_c, Y_c) can be calculated as:

$$X_c = \frac{\sum_{i=1}^n m_i \cdot x_i}{m_t}$$

$$Y_c = \frac{\sum_{i=1}^n m_i \cdot y_i}{m_t} \quad (4.6)$$

Since the mass of each bead is equal, that is, $m_i = m_t/n$. The center of mass can be rewritten as:

$$X_c = \frac{\sum_{i=1}^n x_i}{n}$$

$$Y_c = \frac{\sum_{i=1}^n y_i}{n} \quad (4.7)$$

Assuming that the force on bead $i+1$ is $(F_{i+1, x}, F_{i+1, y})$, we may calculate the total torque as:

$$Q = \sum_{i=1}^n F_{ix}(y_i - Y_c) + F_{iy}(x_i - X_c) \quad (4.8)$$

A positive Q is a driving force for clockwise rotation of microtubule while a negative one is for anti-clockwise rotation.

If the total force in x and y direction is not equal to zero, that is,

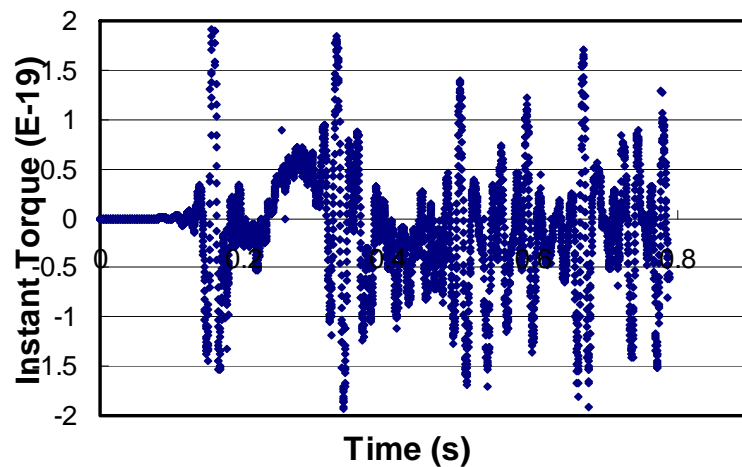
$$F_{xt} = \sum_{i=1}^n F_{ix} \neq 0, \text{ or } F_{yt} = \sum_{i=1}^n F_{iy} \neq 0 \quad (4.9)$$

then, the whole microtubule will move under the force.

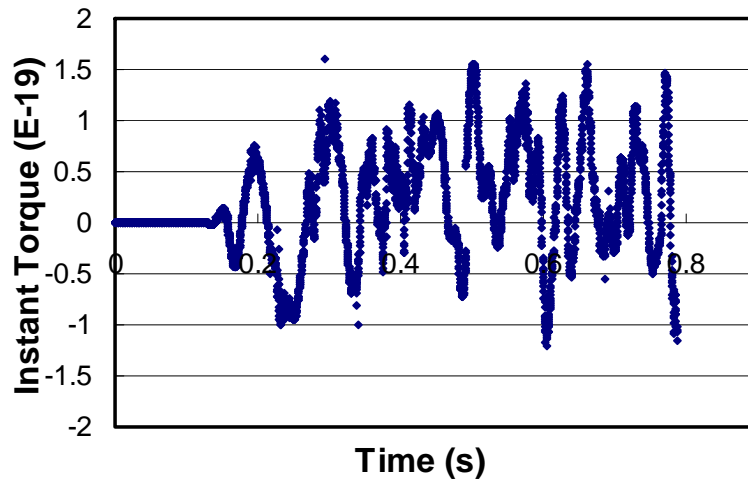
4.4.2 Quantitative instant torque analysis

Bending distances and instant torques were calculated for microtubule-microtubule and microtubule-wall bumping processes to further study the joining mechanisms. Fig. 4.13 illustrates the instant torque against time during microtubule-microtubule and microtubule-wall joining processes with the microtubule length = 12 μm and an approach angle = 45°. As shown, the instant

torque varies with pulse-like fluctuation against time. During a joining process, the bumping force from wall, the driving force from dynein motors and the viscous force from solution are not constant, which is responsible for the fluctuation in the instant torque. For microtubule-microtubule joining, the instant torque shows an approximately symmetric distribution about the line of torque=0. Such a near-symmetric instant torque distribution led to little rotation during the joining process. While for microtubule-wall joining, the instant torque was frequently positive, which provided a non-zero overall torque to drive the microtubule to rotate, resulting in obvious rotation during microtubule-wall joining.



(a) Microtubule-microtubule joining

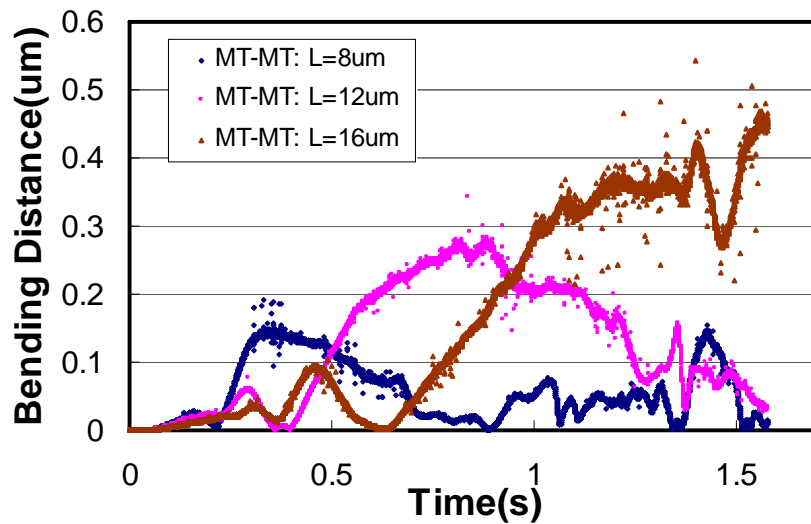


(b) Microtubule-wall joining

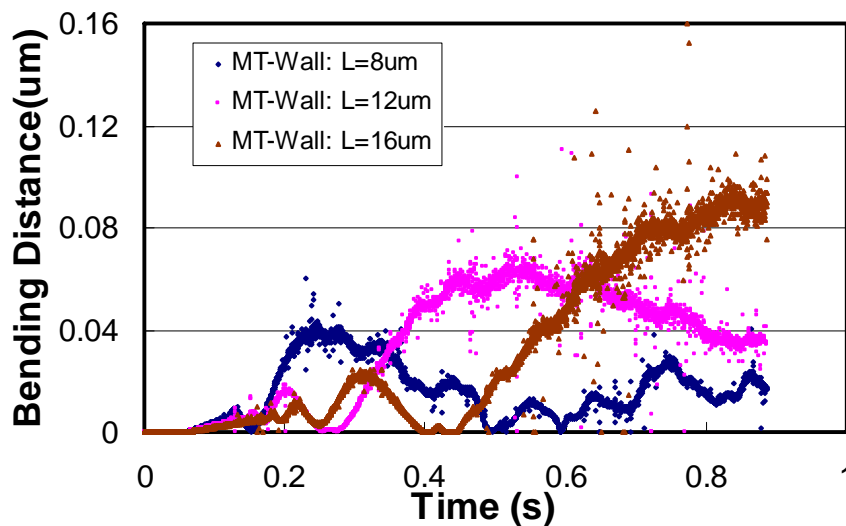
Fig.4.13 instant torque against time for two types of joining with microtubule length = $12 \mu m$ and bumping angle = 45^0

Fig. 4.14 shows changes in the bending distance with respect to time during microtubule-microtubule joining and microtubule-wall joining processes with a bumping angle = 45^0 and a microtubule length of 8, 12, 16 μm , respectively. As shown, when the length of microtubule was increased, the bending distance increased for both types of joining, corresponding to an increase in bending. The highest point of a curve represents the maximum bending of microtubule during the joining process. Compared with microtubule-microtubule joining, the largest bending for microtubule-wall joining was much smaller. This result indicates that bending played a more important role in microtubule-microtubule joining than in microtubule-wall joining, which is consistent with experimental observations. For microtubule-microtubule joining process with a microtubule length of 8 μm , the bending distance reached the maximum at about $t = 0.36s$, which represents the largest bending of microtubule at the moment. The

bending distance decreased to the minimum at $t = 0.9\text{s}$, corresponding to the completion of joining process. The simulation results showed that, for both types of joining processes, with an increase in microtubule length, the time for joining was prolonged.



(a) Microtubule-microtubule joining



(b) Microtubule-wall joining

Fig.4.14 Bending distance against time for two joining processes with bumping angle = 45° and microtubule length = 8, 12, 16 μm , respectively

The bending of a microtubule could be influenced by the stiffness of motors that drive the microtubule. As Fig. 4.15 illustrates, since the stiffness of motor (0.1pN/nm) is much smaller than that of microtubule segment (about 3000pN/nm for $d=30\text{nm}$), the front segment of microtubule is hard to bend. Therefore, the microtubule drift due to the thermal force is mainly controlled by motor stiffness. The drift of the front segment of the microtubule affects its attaching region or probability of being attached by surrounding motors, which could be an important factor for microtubule joining. The larger the stiffness of motor proteins, the smaller the microtubule drift and thus the lower the probability for motor proteins to be attached to the microtubule. This may explain the difference between dynein and kinesin; no MT-MT joining is observed when driven by kinesin, which is less flexible than dynein.

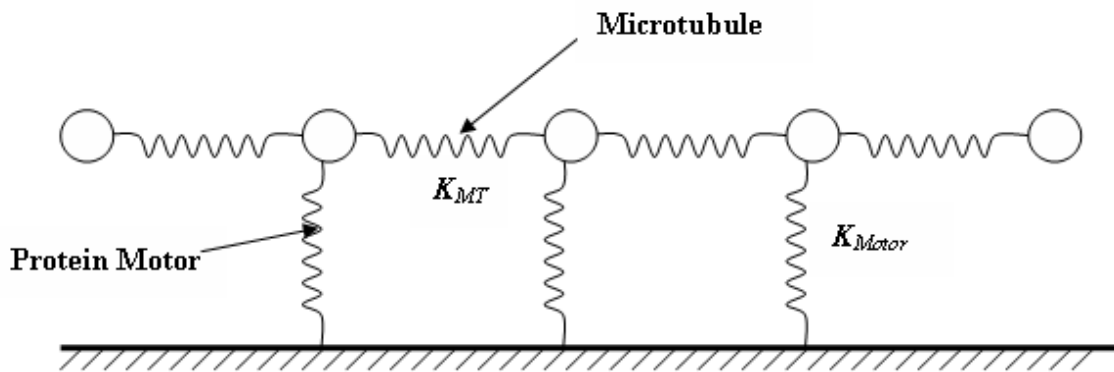


Fig. 4.15 A spring model for microtubule-motor system

When many motors are attached to a microtubule, the microtubule moves under complex loads during joining. Assume that there are $n-1$ dynein motors attaching to microtubule with length $L=nl$. When the microtubule bumps against

the wall, the bumping force generates rotation or bending of the microtubule, as Fig. 4.16 shows. Using the method of superposition, which permits to use the known displacement for simple loads to obtain the deformations for more complicated loadings, the deformation v and

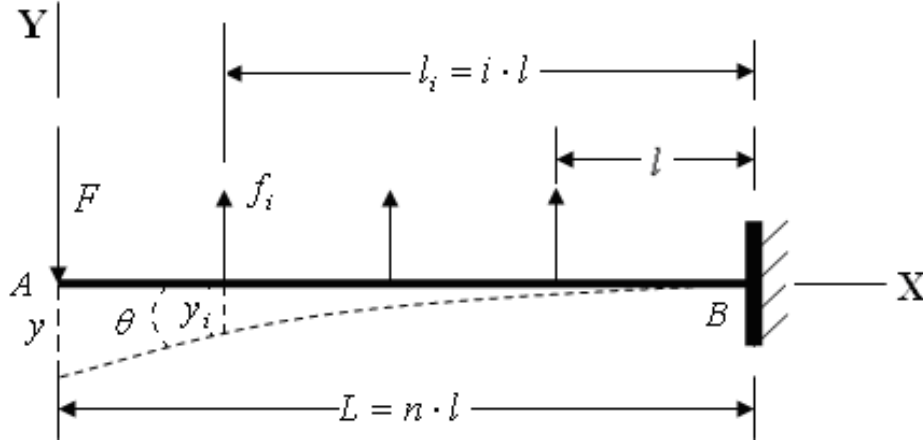


Fig. 4.16 Sketch of bending of rod

deformation angle θ for frond end A can be expressed as (see Appendix D for calculation details):

$$v = \frac{Fx^2}{6EI}(3nl - x) - \sum_{i=1}^k \frac{f_i i^2 l^2}{6EI}(3x - il) - \sum_{i=k}^{n-1} \frac{f_i x^2}{6EI}(3il - x), \quad (k-1)l \leq x \leq kl$$

$$v_A = \frac{Fn^2 l^2}{2EI} - \sum_{i=1}^{n-1} \frac{f_i i^2 l^2}{6EI}(3nl - il)$$

$$\theta_A = \frac{Fn^2 l^2}{2EI} - \sum_{i=1}^{n-1} \frac{f_i i^2 l^2}{2EI} \quad (4.10)$$

According to this equation, with an increase of microtubule length, θ will increase, which represents an increase in microtubule bending. The influence of

the number of dynein (or density of dynein) is complicated and hard to determine. A further analysis of this equation is needed.

Fig. 4.17 illustrates the bumping force against time for microtubule-microtubule and microtubule-wall joining with an approach angle of 45° and the microtubule length of $12 \mu\text{m}$. The bumping force for microtubule-wall joining was higher than that for microtubule-microtubule joining. During microtubule joining, there were two main forces: drag force from dynein motors and bumping force from wall or microtubule.

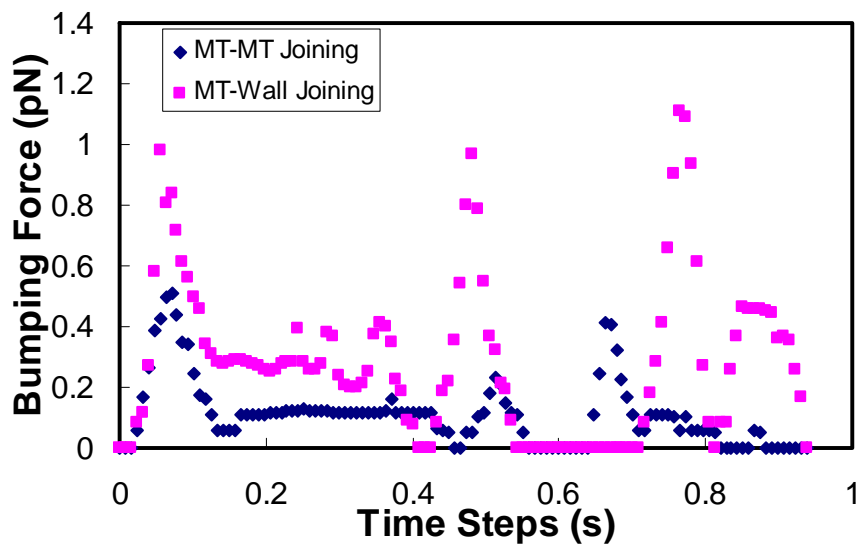


Fig.4.17 Bumping force against time for microtubule-microtubule and microtubule-wall joining with a bumping angle = 45° and a microtubule length = $12 \mu\text{m}$

Compared to the microtubule, the wall was rigid and generated a larger bumping force, as demonstrated in Fig. 4.19. In order to rotate the microtubule,

the bumping force should be large enough to overcome the drag force from dyneins, which generated an anti-rotation torque. For microtubule-microtubule joining, its bumping force was not large enough to generate rotation, so that the local bending could play a predominant role in the microtubule-microtubule joining process. While for the microtubule-wall joining, the bumping force was much larger, which could help the microtubule to escape from the control of dynein motors and rotate during the joining process. The shorter the microtubule, the lower the number of dyneins to attach to a microtubule and thus smaller the drag force. Therefore, rotation is more predominant for short microtubules.

As a final remark, this work was carried out to investigate the MT-MT and MT-wall collision processes and analyze involved instant bumping force, torque and related issues. The study generates information that is useful to the design of micro-fabricated tracks for effective control of the microtubule movement and optimal arrangement of biological motors in potential nano/micro-bio-machine systems.

4.4 Conclusions

Chapter 4 reports our recent experimental observations of two joining processes of microtubules driven by dynein c: microtubule-microtubule joining and microtubule-wall joining. When two microtubules approached each other, they frequently joined each other, no matter whether they moved in parallel or in opposite directions. Bending and rotation of microtubules participated in the

joining processes. The former appeared to dominate MT-MT joining while the latter was more obvious during MT-wall collision. The microtubule length influenced the joining processes. It was observed that when one microtubule joined another, it bent with little rotation, which was independent of approach angle or the length of microtubules. However, the microtubule-wall joining showed different behavior. When met or collided with a rigid wall, the microtubule rotated and then moved along the wall. Short microtubules rotated during the joining process with little bending. With an increase in microtubule length, the role that bending during the joining process became more important.

A computational model is proposed to study the MT-MT and MT-wall joining or collision processes with the aim of investigating the behavior of microtubules during the processes. The simulation study demonstrated that bending dominated microtubule-microtubule joining while rotation played a more important role in microtubule-wall joining process, which was consistent with experimental observations. Quantitative computational analysis was made to investigate the instant bumping force, torque and related issues. For both types of joining, with an increase in the microtubule length, bending became obvious and the time for joining was prolonged. There existed a symmetric torque distribution for microtubule-microtubule joining, resulting in little rotation; while a positive torque distribution was found for microtubule-wall joining, responsible for obvious rotation during this joining process. The larger bumping force generated during microtubule-wall collision could help the microtubule escape from the constraint dynein motors and thus promoted the rotation of the microtubule during

the joining process. The information obtained from the study would be helpful to the design of micro-fabricated tracks for effective control of the microtubule movement and optimal arrangement of biological motors in potential nano/micro-bio-machine systems.

Reference

1. Kron, S. J., J. A. Spudich. 1986. Fluorescent actin filaments move on myosin fixed to a glass surface. *Proc. Natl. Acad. Sci. USA* 83: 6272–6276.
2. Kron, S. J., Y. Y. Toyoshima, T. Q. P. Uyeda, J. A. Spudich. 1991. Assays for actin sliding movement over myosin-coated surfaces. *Methods in Enzymology* 196: 399-416.
3. Vale, R. D., J. Howard; A.J. Hudspeth, I. R. Gibbons. 1990. Properties of kinesin and dynein-induced microtubule transport. *Journal of Muscle Research and Cell Motility* 11: 535-535.
4. Mansson, A., M. Balaz, N. Albet-Torres. 2008. In vitro assays of molecular motors - impact of motor-surface interactions. *Frontiers in Bioscience* 13: 5732-5754.
5. Hess, H., G. D. Bachand, V. Vogel. 2004. Powering nanodevices with biomolecular motors. *Chemistry-A European Journal* 10: 2110-2116
6. Van Den Heuvel, M. G. L., C. Dekker. 2007. Motor proteins at work for nanotechnology. *Science* 317: 333-336.
7. Suzuki, H., A. Yamada, K. Oiwa, H. Nakayama, S. Mashiko. 1997. Control of actin moving trajectory by patterned poly (methyl methacrylate) tracks. *Biophysical Journal* 72: 1997-2001.
8. Hiratsuka, Y., T. Tada, K. Oiwa, T. Kanayama, T.Q. Uyeda. 2001. Controlling the direction of kinesin-driven microtubule movements along microlithographic tracks. *Biophysical Journal* 81: 1555-1561.

9. Hess, H., J. Clemmens, D. Qin, J. Howard, V. Vogel. 2001. Light-controlled molecular shuttles made from motor proteins carrying cargo on engineered surfaces. *Nano Lett.* 1: 235-239.
10. Nitta, T., A. Tanahashi, M. Hirano, H. Hess. 2006. Simulating molecular shuttle movements: Towards computer-aided design of nanoscale transport systems. *Lab On A Chip* 6: 881-885.
11. Oiwa, K., H. Sakakibara. 2005. Recent progress in dynein structure and mechanism. *Current Opinion in Cell Biology* 17: 98-103.
12. Sakakibara, H., H. Kojima, Y. Sakai, E. Katayama, K. Oiwa. 1999. Inner-arm dynein c of chlamydomonas flagella is a single-headed processive motor. *Nature* 400: 586-591.
13. Kagami, O., R. Kamiya. 1992. Translocation and rotation of microtubules caused by multiple species of Chlamydomonas inner-arm dynein. *J. Cell Sci.* 103: 653-664.
14. Vallee, R. B. 1986. Reversible assembly purification of microtubules without assembly-promoting agents and further purification of tubulin, microtubule-associated proteins, and MAP fragments. *Meth. Enzymol.* 134: 89-104.
15. Howard, J., A. Hyman. 1993. Preparation of marked microtubules for the assay of the polarity of microtubule-based motors by fluorescence microscopy. *Methods in Cell Biology* 39: 105-113.
16. Hunt, A. J., F. Gittes, J. Howard. 1994. The force exerted by a single kinesin molecule against a viscous load. *Biophysical Journal* 67: 766-781

Chapter 5

Simulation of self-organization of microtubule driven by dynein C

5.1 Introduction

As described in Chapter 4, microtubules can join together driven by dyneins, indicating that microtubules are mutually influenced. Such joining property or interaction makes it possible for microtubules to form specific self-organized patterns. In previous studies, it was observed that in mitosis, microtubules could be self-organized into polar asters with minus ends gathered in the center and plus ends extending outward [1], which is attributed to the capacity of centrosomes to nucleate and stabilize the MT minus ends [2]. Molecular motors could play a role in the organization of MT arrays [3]. Recently, we observed that microtubules could form stable circular patterns, driven by dynein c, as Fig.5.1 illustrates. In this system, dyneins were randomly distributed on a substrate surface (the experimental condition is similar to that reported in [4]). When microtubules were placed into the system, initially they moved randomly, driven by the dyneins. After a period of time (~ 10 min), circles formed as shown in Fig.5.1 (the figure is provided by Dr. K. Oiwa, Japan). Such self-organized movement of microtubules indicates that microtubules mutually interact, which need to be taken into account when design potential nano-bio-machines using dynein as a biological motor and microtubules as a power transfer medium (e.g., to drive a nano-gear). However, it is unclear how such circular patterns form and what parameters control the pattern formation. Getting an insight into the self-organization of microtubules driven by dynein motors is of importance to the application of dynein motors and microtubules in nano-bio-machine development. Due to the experimental limitation, it is difficult to

determine what factors govern the formation of the circular patterns. Computer modeling allows performing “computational experiments” under controlled conditions. The effect of each parameter on a specific process could thus be studied separately. This makes computer modeling an effective method complementary to experimental techniques for understanding the self-organization phenomenon and predicting microtubules’ behavior during the pattern formation process.

In this study, a phenomenological modeling study based on the general model system described in previous chapters with incorporation of a Monte Carlo approach was conducted to investigate possible roles of microtubule bias, joining, and density during the self-organization processes of microtubules driven by dynein motors. In chapter 4, a bending model developed from the general model was used to analyze joining mechanism of microtubules. The model could also be applied to determine the MT-MT joining probability distribution and microtubule bias. However, in the current 2D model, it is assumed that one microtubule would not pass another microtubule, which is different from experimental observations, in which microtubule could sometimes cross another microtubule without joining. In addition, some important factors are not considered in the model, such as the fluctuation of microtubule in the z direction, the self rotation of microtubule, or microtubule distortion, and electrostatic interaction between microtubules or between microtubule and dyneins, which may have an important influence on microtubule joining and microtubule bias. In order to theoretically determine microtubule joining and microtubule bias, a systematic work involving all these

factors needs to be done. Considering its complexity, only experimentally determined distribution of microtubule joining probability and microtubule bias were incorporated into the modeling study. Mutual influences of the parameters and their simultaneous effects on the self-organized pattern formation were investigated.

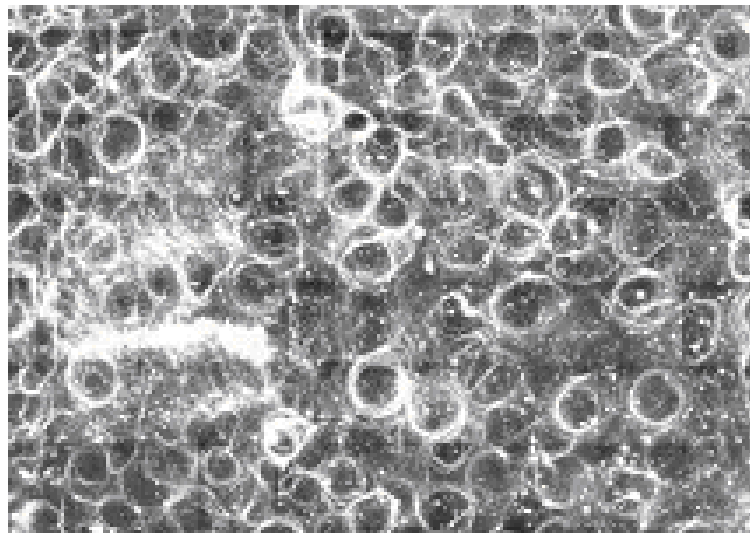


Figure 5.1 Circular pattern of microtubules driven by dynein motors.

5.2 Model Description

A computer model, based on the general model described in previous chapters incorporated with a Monte Carlo approach, was built to simulate the self-organized microtubule (MT) movement. The MT self-organization is a process involving a large number of microtubules, in which the interaction between microtubules must play an important role. In this model, two key parameters that could govern the MT self-organization are included; they are the microtubule joining probability and microtubule bias.

5.2.1 Joining probability distribution and microtubule bias

5.2.1.1 The MT joining probability distribution

The self-organized patterns have many circles, each of which contains a number of microtubules (MT). Driven by dyneins, the microtubules could move together (joining), in similar (parallel) or opposite (anti-parallel) directions. Such MT's joining should play an important role in the pattern formation. As mentioned in chapter 4, experiments demonstrated that the MT's joining was greatly affected by the bumping angle between two microtubules. By counting experimental joining events, the joining probability distribution with respect to the bumping angle could be determined. Fig.5.2 illustrates an experimentally determined joining probability distribution with respect to the bumping angle. As shown before, when two microtubules moved in parallel or anti-parallel directions and bumped at small angles, they showed higher probabilities to join. At higher bumping angles, no matter whether the merge was parallel or anti-parallel, the joining probability decreased sharply. Such joining distribution was taken into account in the present simulation.

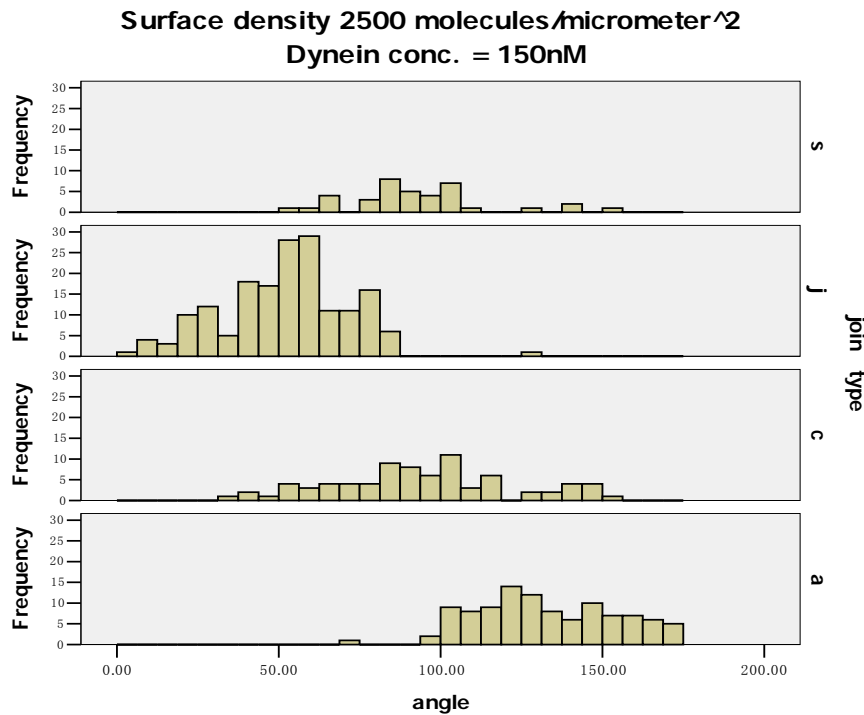


Fig.5.2 Probability distributions of different joining events. a: anti-parallel joining, c: crossing, j: parallel joining, s: stopping

5.2.1.2 The microtubule bias

Experiments also demonstrated that when a microtubule moved in a solution, there was a bias which made the microtubule move in a curved path. Fig. 5.3(a) illustrates a bias distribution observed experimentally (data were provided by K. Oiwa, (Japan)), in which, 52% microtubules moved along curved paths with their radii $>500\mu\text{m}$ (called the bias radius, R), 34% microtubules moved along ones with radii between $200\sim 500\mu\text{m}$, and 14% microtubules moved along curved paths with radius between $50\sim 200\mu\text{m}$.

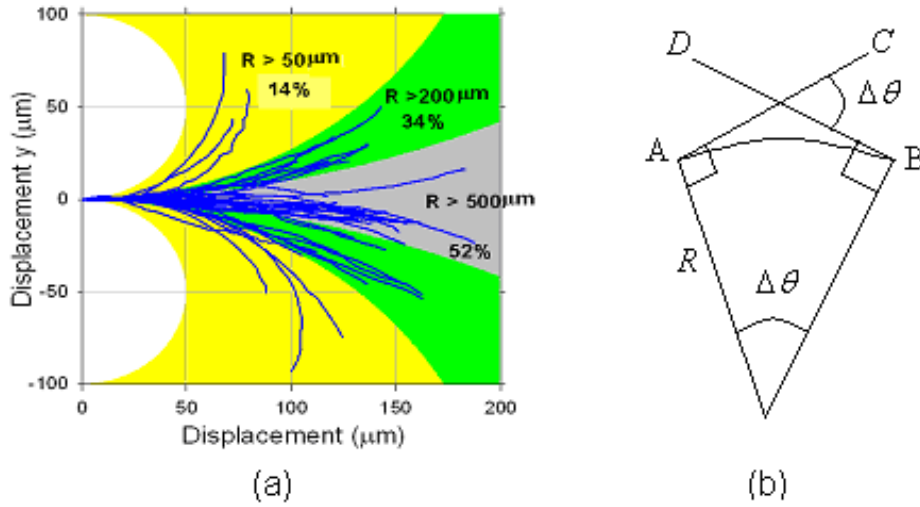


Fig.5.3 A nominal microtubule bias definition (a) Experimentally observed bias distribution of microtubule in solution; (b) parameters used to describe the MT bias

Previous research demonstrated that the microtubule bias could influence the self-organization of microtubules [5, 6]. Understanding the influence of the bias on the self-organized pattern formation would be helpful to the design of microtubule-dynein nano-bio-machine systems, although what causes the bias has not yet been clarified. In order to incorporate the microtubule bias into the present model, a nominal microtubule bias rate was defined. As illustrated in Fig. 5.3(b), when the front end of a microtubule moves from position A to position B along arc AB (assume that the MT velocity, V , is constant) after short time interval time, Δt , its moving direction will change from AC to DB with an angle change ($\Delta\theta$). A relationship between $\Delta\theta$ and Δt can be expressed as:

$$\Delta\theta = \frac{V \cdot \Delta t}{2\pi R} \cdot 2\pi = \frac{V \cdot \Delta t}{R} \quad (5.1)$$

where R is the bias radius of microtubule. A bias rate is defined as the angle change per unit time and expressed as:

$$r_{\theta} = \frac{\Delta\theta}{\Delta t} = \frac{V}{R} \quad (5.2)$$

which only depends on the moving velocity and the bias radius (R).

In the current model, a constant velocity of microtubule was used in simulation. Therefore, only the bias radius of microtubule affects the bias rate. In order to simplify the model, two bias rates (positive/clockwise and negative/anticlockwise) with equal absolute value were assigned randomly to the microtubules.

The microtubule bias and microtubule joining may be mutually influenced. It was experimentally observed that after joining, microtubules sometimes separated from each other, although in most cases they do not. Based on experimental observations and bias rate directions, when two microtubules join together, all possible situations were considered as shown in Fig.5.4. r_1 and r_2 are the bias rate of microtubule 1 (MT1) and microtubule 2 (MT2), respectively. Here the absolute value of r_1 and r_2 are equal, that is $|r_1| = |r_2|$. The joining and separation of two microtubules were decided by following rules:

A. Parallel joining:

1. For conditions (a1) and (a3), the MT2 will follow the direction of MT1, but without change bias rate since $r_1=r_2$
2. For condition (a2), MT1 will follow the direction of MT1, and change bias rate from r_2 to r_1 . (here $r_1 = -r_2$)

- For condition (a4), MT2 will separate from MT1 without change bias rate.

B. Anti-parallel joining:

- For condition (b1) and (b2), the MT2 will separate from MT1 without changing bias rate
- For condition (b3), the MT2 will follow the opposite direction of MT1 without changing bias rate since $r_1=r_2$
- For condition (b4), the MT2 will follow the opposite direction of MT1 and change bias rate from r_2 to r_1 . (here $r_1 = -r_2$)

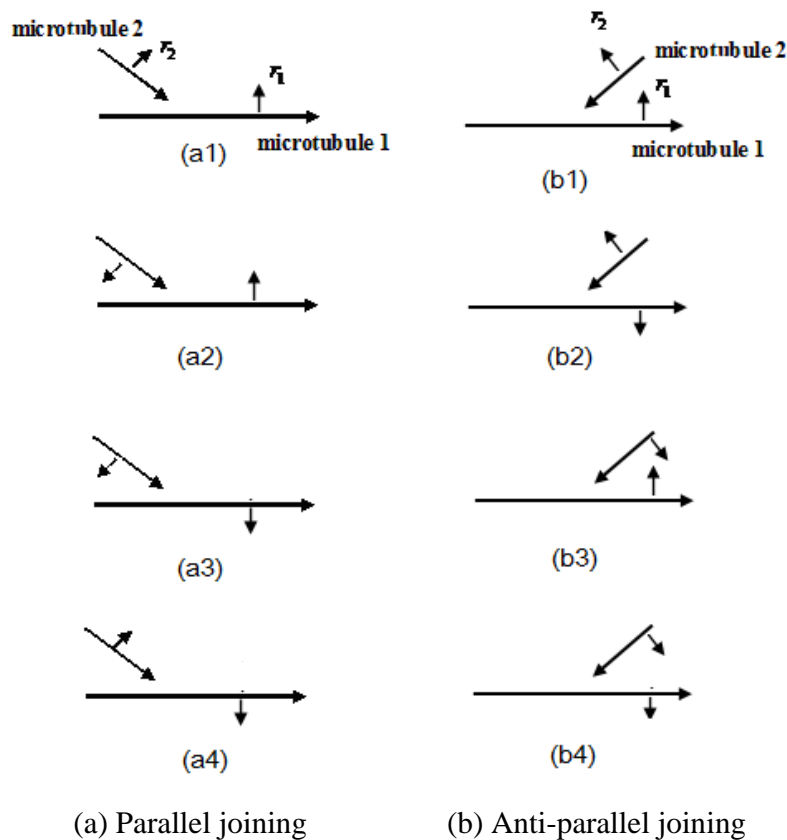


Figure 5.4 Different MT joining processes influenced by the microtubule bias under different joining condition (a) parallel joining; (b) anti-parallel joining

Which case would occur is judged by considering a few factors: the position of the front end of microtubule 2 relative to microtubule 1, the bias rates of both the two microtubules, and their moving directions. The relationship between the bias rate variation and microtubule joining has been analyzed (presented in 5.2.3) through the simulation study to understand the bias effect on the self-organized pattern formation of microtubules.

5.2.2 Multiple joining

During joining process, it is possible that several microtubules join together at the same time to form some bundles. Fig. 5.5 (a) illustrates a joining chain when microtubule 1 joins microtubule 2 as well as microtubule 2 joins microtubule 3. In this case, microtubule 1 and 2 will follow the moving direction of microtubule 3 and form a bundle, as Fig. 5.5(b) illustrates. Such situation should be considered in the simulation system.

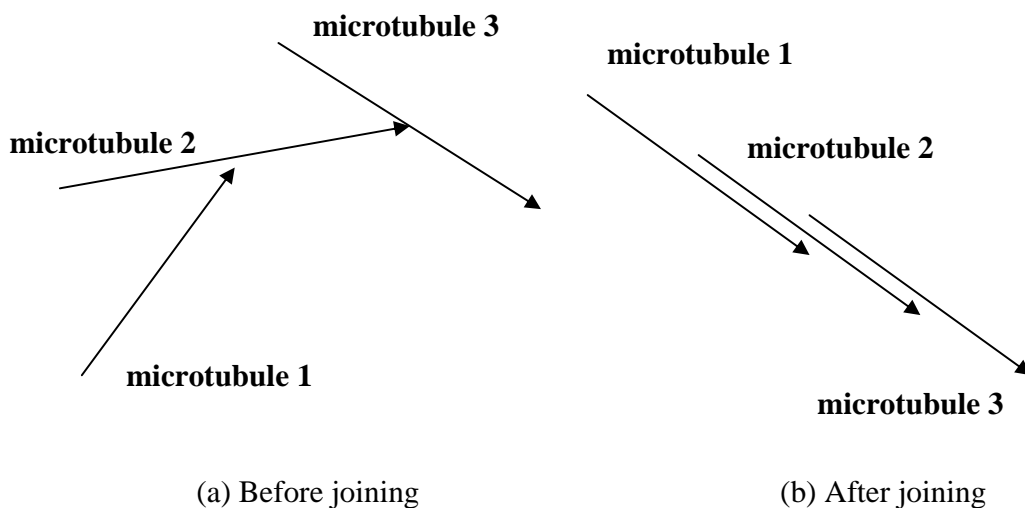


Fig.5.5 A multiple joining process

5.2.3 The simulation process

In this model, 10,000 microtubules with a $10\mu m$ length were randomly placed in the system. Periodical boundary conditions were applied in two dimensions. The dimensions of the system were $100\mu m \times 100\mu m$. The velocity of microtubules was set as $10\mu m/s$ and time step was set as 0.05s. A Monte Carlo approach was applied for simulation process.

Initially, microtubules were randomly but uniformly distributed in the system. A joining probability as a function of the bumping angle, $P(\theta)$, used based on the experimental observations shown in Figure 5.2. For microtubule i , at time t , its velocity $v(i,t)$, moving direction or angle relative to the system and bias rate are represented as $v(i,t)$, $\theta(i,t)$ and $r(i,t)$, respectively.

In simulation, the key step is to determine whether two microtubules will join or not when they meet. Figure 5.6 illustrates a merging event of two microtubule, MTs i and j . d_1 is the minimum distance between the front end of microtubule i and microtubule j [point (x_0, y_0)]. (x_{i1}, y_{i1}) is the position of front end of microtubule i . (x_{j1}, y_{j1}) and (x_{j2}, y_{j2}) are the front and tail ends of microtubule j , respectively. The bumping angle between the two microtubules at time t is $\theta(i, j, t)$.

To join together, the microtubules should satisfy two prerequisites: 1) d_1 must be smaller than a critical distance d_c , which is set as 20nm in the model; and 2) the point (x_0, y_0) is between (x_{j1}, y_{j1}) and (x_{j2}, y_{j2}) .

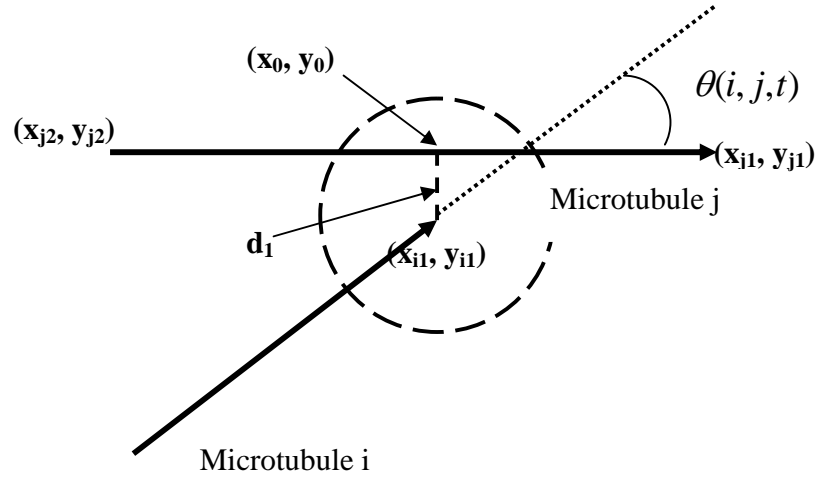


Figure 5.6 Joining condition of two microtubules

The joining probability of microtubules i and j at time t may be expressed as:

$$P(i, j, t) = P(\theta = \theta(i, j, t)) \cdot 1_{\{d_1 < d_c\}} \cdot 1_{\{(x_0, y_0) \in (\text{microtubule } 2)\}} \quad (5.3)$$

where $P(\theta = \theta(i, j, t))$ is the joining probability when the bumping angle is equal to $\theta(i, j, t)$. The value of $P(\theta)$ is determined based on the experimentally observed joining probability distribution as shown in Fig.5.2.

$1_{\{d_1 < d_c\}}$ and $1_{\{(x_0, y_0) \in (\text{microtubule } 2)\}}$ are indicator functions to indicate whether the condition satisfy the two joining prerequisites that we mentioned above.

$$1_{\{d_1 < d_c\}} = \begin{cases} 1, & \text{if } d_1 < d_c \\ 0, & \text{Otherwise} \end{cases} \quad (5.4)$$

$$1_{\{(x_0, y_0) \in (\text{microtubule } 2)\}} = \begin{cases} 1, & \text{if } (x_0, y_0) \text{ belongs to microtubule } 2 \\ 0, & \text{Otherwise} \end{cases} \quad (5.5)$$

In order to determine whether the two microtubules join together or not, a uniformly distributed random number between 0 and 1 is generated by computer

at time t as $R(i, j, t)$. A joining process function of microtubules i and j , $\delta(i, j, t)$, may be expressed as:

$$\delta(i, j, t) = \begin{cases} 1, & \text{if } R(i, j, t) < P(i, j, t) \\ 0, & \text{if } R(i, j, t) > P(i, j, t) \end{cases} \quad (5.6)$$

If $\delta(i, j, t) = 1$, microtubule i would join microtubule j and move along with microtubule j . If $\delta(i, j, t) = 0$, they would continue to move along their own directions.

Thus, the change in the moving direction of microtubule i , $\Delta\theta(i, t)$, can be expressed as:

$$\Delta\theta(i, t) = \begin{cases} 0, & \text{if } \delta(i, j, t) = 0 \text{ (without joining)} \\ \theta(j, t) - \theta(i, t), & \text{if } \delta(i, j, t) = 1 \text{ and } \theta(i, j, t) < 90^\circ \\ \theta(j, t) - \theta(i, t) + 180^\circ, & \text{if } \delta(i, j, t) = 1 \text{ and } \theta(i, j, t) > 90^\circ \end{cases} \quad (5.7)$$

The bias rate of microtubule needs to be recalculated for all possible situations as illustrated in Figure 5.4, which is related to joining condition of two microtubules and the bias rates of two microtubules. The change in the bias rate, $\Delta r(i, t)$

$$\Delta r(i, t) = \begin{cases} 0, & \text{under cases a1, a3, a4, b1, b2, b3 in Fig.5.4} \\ r(j, t) - r(i, t), & \text{under cases a2 and b4 in Fig.5.4} \end{cases} \quad (5.8)$$

here $r(i, t)$ and $r(j, t)$ are bias rates of microtubule i and j , respectively.

Therefore, the new moving angle of microtubule i at time $t + \Delta t$ becomes

$$\theta(i, t + \Delta t) = \theta(i, t) + \Delta\theta(i, t) + \Delta r(i, t) \quad (5.9)$$

The position of the front end of microtubule i at time $t + \Delta t$ can be determined as:

$$x_i(t + \Delta t) = x_i(t) + v_i(t) \cdot \cos(\theta_i(t))$$

$$y_i(t + \Delta t) = y_i(t) + v_i(t) \cdot \sin(\theta_i(t)) \quad (5.10)$$

Following these steps, we can determine trajectories of all microtubules. Consequently, the self-organized movement of a large number of microtubules could be simulated.

5.2.4 The cell list algorithm for computing efficiency

A problem in the above model is how to calculate the distance between the front end of one microtubule and any other microtubule. It will take too much time if we calculate all pairs of microtubules. For example, if there are n microtubules in the system, for each simulation cycle described above, we need to calculate $n(n-1)$ times such distance. If $n=10000$, then $n(n-1) \approx 10^8$. That is unacceptable for a computational model. In order to improve calculating efficiency, a cell list algorithm was used in the simulation. As Fig.5.7 illustrates, the system was divided into cells. The side size (L) of each square cell was $5 \mu m$. Each cell was marked by two integer numbers, i and j , which represent the position of cell in x and y direction. For example, a cell (i, j) was a $(i+1)$ th cell in x direction and $(j+1)$ th cell in y direction. For the beginning the each cycle, the central point (X_c, Y_c) of a microtubule was calculated and then its cell position was determined by the position of its central point by using following equations:

$$i = [X_c / L]$$

$$j = [Y_c / L]$$

where $[X_c / L]$ represents the maximum integer of X_c / L .

	(i-1,j+1)	(i,j+1)	(i+1,j+1)				
	(i-1,j)	(i,j)	(i+1,j)				
	(i-1,j-1)	(i,j-1)	(i+1,j-1)				
(0,0)							

Figure 5.7 A cell list system

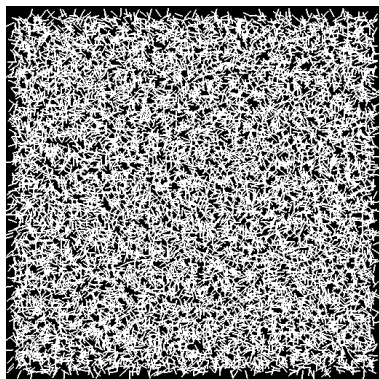
For each cycle, the central points of all microtubules were initially calculated and the cells to which the calculated positions belong were determined using the above described method. For each microtubule, the cell position of its front end was calculated, for instance, in cell (i,j) . Then, this microtubule could only have opportunity to join with the microtubules whose central points are in 9 adjacent cells: $(i-1,j+1)$, $(i,j+1)$, $(i+1,j+1)$, $(i-1,j)$, (i,j) , $(i+1,j)$, $(i-1,j-1)$, $(i,j-1)$, $(i+1,j-1)$.

5.3 Simulation results and analysis

5.3.1 The influence of microtubule bias on the MTs' self-organization

Fig. 5.8 shows simulated microtubule systems respectively with and without bias. For a system without bias, lined bundles were formed (Fig. 5.8b).

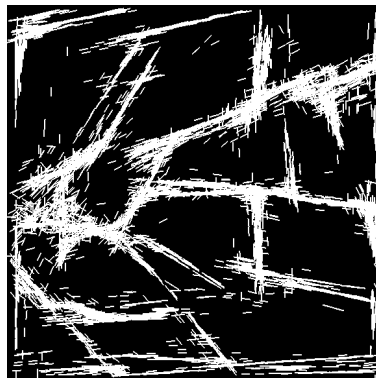
With an increase in the bias rate, the MT bundles interweaved and formed some polygon patterns with sharp angles (Fig. 5.8c). When the bias rate was increased to 0.024, a circular pattern was observed (Fig. 5.8d). The circular pattern was similar to those that were experimentally observed. However, a further increase in the bias rate, the circular pattern disappeared and the polygon pattern showed again (Fig. 5.8e). When the bias rate was increased to 0.096, even the polygon pattern disappeared and only lined bundles were observed (Fig. 5.8f). Thus, the bias helped to increase the roundness of the polygon pattern but destroyed the roundness if the bias was continuously increased. Clearly, the bias played an important role in the formation of circular patterns.



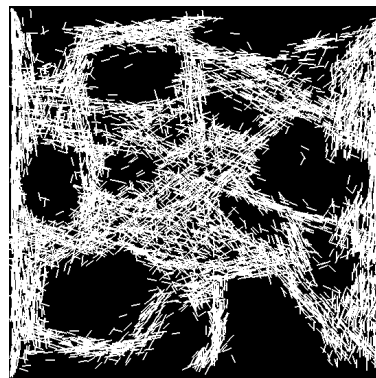
(a)



(b)



(c)



(d)

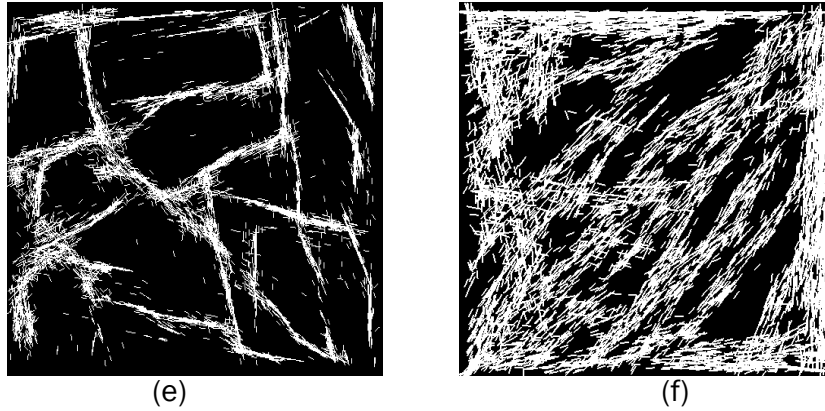


Fig.5.8 Simulated pattern formation from an initial state (a) initial state, (b) bias rate = 0, (c) bias rate = 0.006, (d) bias rate = 0.024, (e) bias rate = 0.048, (f) bias rate = 0.096

The process of self-organization was successive, beginning with randomly distributed microtubules moving in random directions as shown in Figure 5.9. After 2000 steps, the microtubules joined together and formed bundles. With further movement, the MT bundles interlaced, forming relatively round patterns. The size of the round patterns increased with time and eventually became stable. Indeed, experimentally observed MT self-organization is successive, which usually takes minutes to result in relatively stable circular patterns.

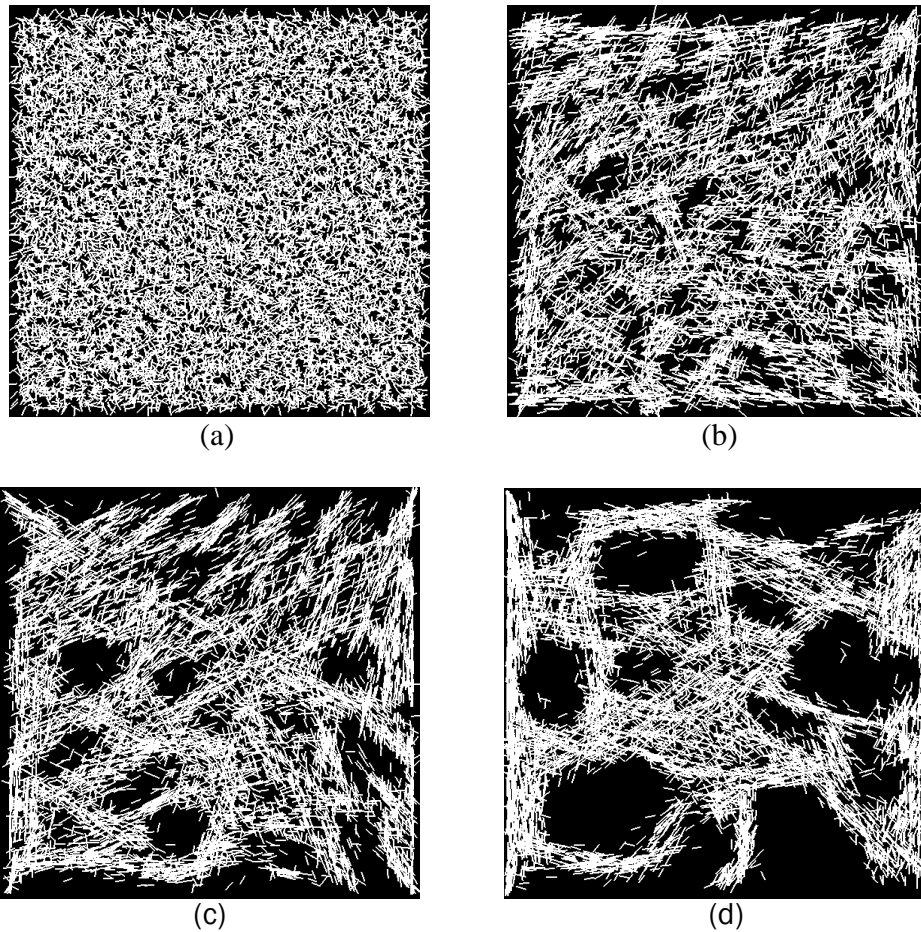
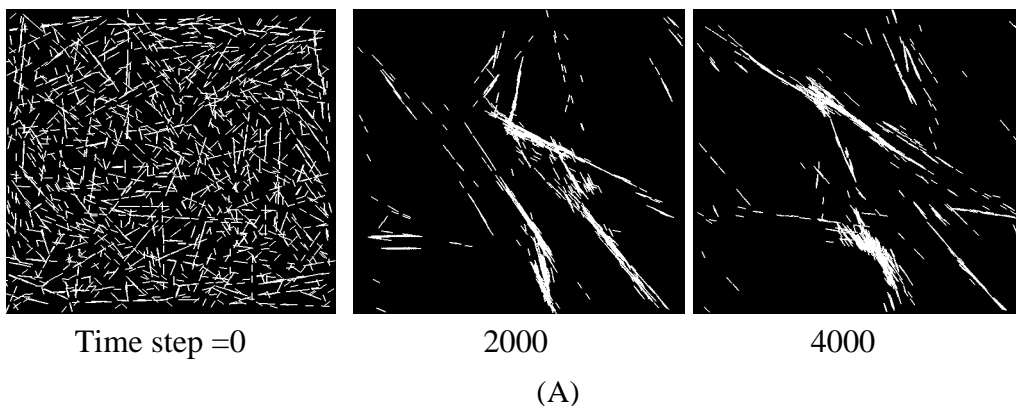


Fig. 5.9 Self-organization process of microtubules with density = $10000/10000 \mu m^2$ and bias rate = 0.024. (a) Initial state; (b) after 2000 steps; (c) after 4000 steps; and (d) after 8000 steps

5.3.2 The influence of microtubule density on MT self-organization

The microtubule density may affect the formation of self-organized MT circular patterns. In section 5.3.2, the system under study had a microtubule density = $10000/10000 \mu m^2$. In this section, processes with two different MT

densities, $2500/10000 \mu m^2$ and $225000/10000 \mu m^2$, were simulated and compared to investigate how the MT density affected the formation of self-organized MT circular patterns. The bias rate was set as 0.024. As Fig.5.10 illustrates, for the lower microtubule density, microtubule joining events decreased, which reduced the chance for microtubules to form long bundles and a MT network that led to the formation of circular pattern (as that shown in Fig. 5.9). When the MT density was low, only short bundles were observed, with which it was difficult to form polygon patterns. In contrast, with the higher microtubule density, MT joining opportunities increased, resulting in an increase in the amount of bundles. However, if the MT is too high, the strong interference between MTs also makes it difficult for microtubules to form circular pattern. In addition, for the high-density process, microtubules took much longer time than the low-density process to form bundles.



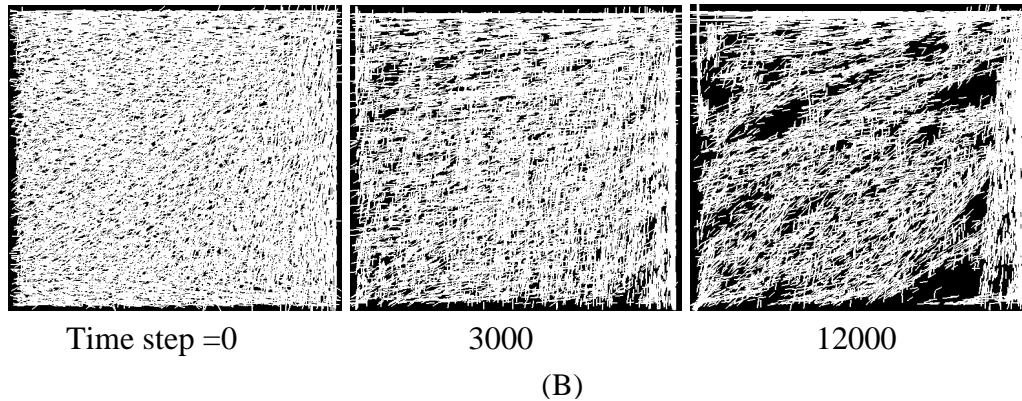


Fig. 5.10 Self-organization processes with different microtubule densities. (A) Density = $2500/10000 \mu m^2$; (B) Density = $225000/10000 \mu m^2$

5.3.3 The influence of microtubule joining probability distribution on The MT self-organization

Driven by dyneins with a fixed density, the joining probability distribution of microtubules could be affected by several other factors, e.g., microtubule length and density, MT bias, and the bumping angle, etc. The joining probability may largely influence the formation of circular patterns since the self-organization begins with the formation of MT bundles. In order to study the effect of joining probability on MT self-organization, three joining probability distributions, low, middle, and high, with respect to the bumping angle were used (see Table 5.1). The bias rate was set to be 0.024. Fig.5.11 shows simulated self-organization of microtubules with the three joining probability distributions. As shown, the low joining probability distribution resulted in polygon patterns with irregular shapes and sharp angles. With an increase in the joining probability, the polygons became round and relatively circular patterns formed. However, further increase in the joining probability led to irregular polygon patterns again. Such changes

could be explained. The MT joining is necessary to MT self-organization formation, since the network of microtubules should result from the interaction between microtubules. Otherwise, microtubules would move randomly. However, if the interaction is too strong, the flexibility of MT bundles could be reduced, thus increasing the difficulty in the development of self-organized circular patterns.

Table 5.1 Three types of joining probability distribution against bumping angle

Joining angle ($^{\circ}$)	0-30	30-60	60-90	90-120	120-150	150-180
Joining Probability						
Low	0.8	0.6	0.4	0.4	0.6	0.8
Middle	0.9	0.7	0.5	0.5	0.7	0.9
High	1.0	0.8	0.6	0.6	0.8	1.0

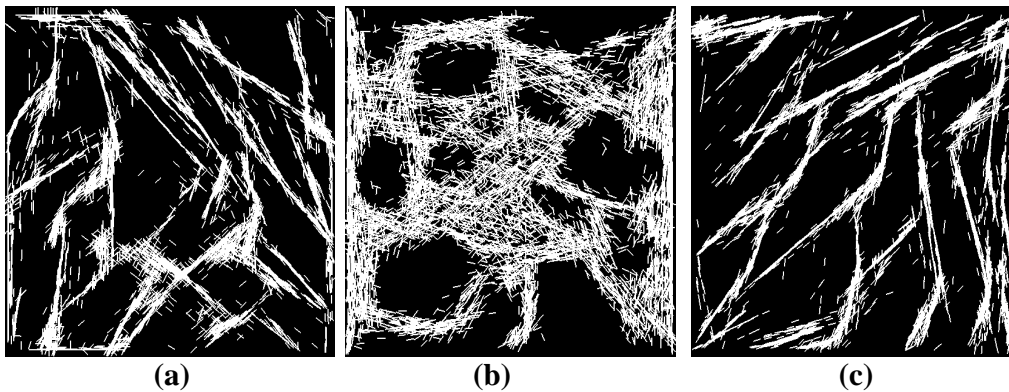


Fig.5.11 Self-organized patterns of microtubules with different joining probability distributions: (a) low, (b) middle, and (c) high.

5.4 Quantitative analysis

5.4.1 Variations in the MT joining frequency with time

In order to get an insight into the MT self-organization, a quantitative analysis was conducted to study the joining frequency of microtubules in different bumping angle ranges with respect to time. The joining frequency was an average number of joining events happened in a specific angle range for each 10 steps. Fig.5.12 shows the joining frequency as a function of time with a microtubule density = $10000/10000 \mu m^2$ and a bias rate = 0.024. In this study, the middle joining probability distribution in table 1 was used. As shown, for both low bumping angles ($0^{\circ}\sim 30^{\circ}$) and high bumping angles ($150^{\circ}\sim 180^{\circ}$), the joining frequency increased continuously with time, resulting in the formation of MT bundles. While the joining frequency for bumping angles between $30^{\circ}\sim 150^{\circ}$ slightly decreased from about 500 to 400. When bundles with large angle interlaced with each other, joining frequency of the small angles (i.e. parallel and anti-parallel) continuously increased, which facilitated the formation of circular patterns. It was observed that as time increased, the size of circular patterns increased. This should also result from the increases in joining probability of microtubules bumping at low angles (near parallel) and high angles (near anti-parallel), which favor the formation of larger circular MT bundles.

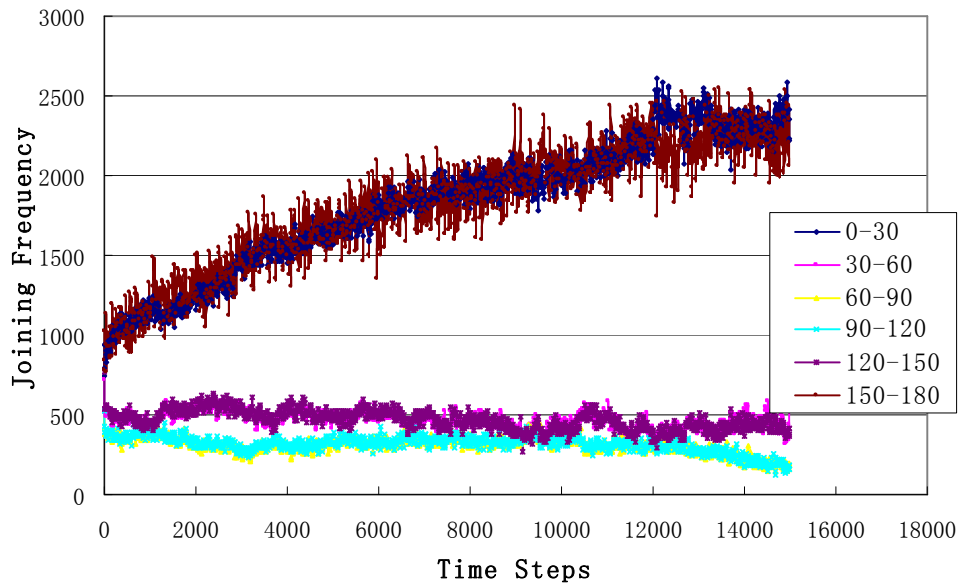
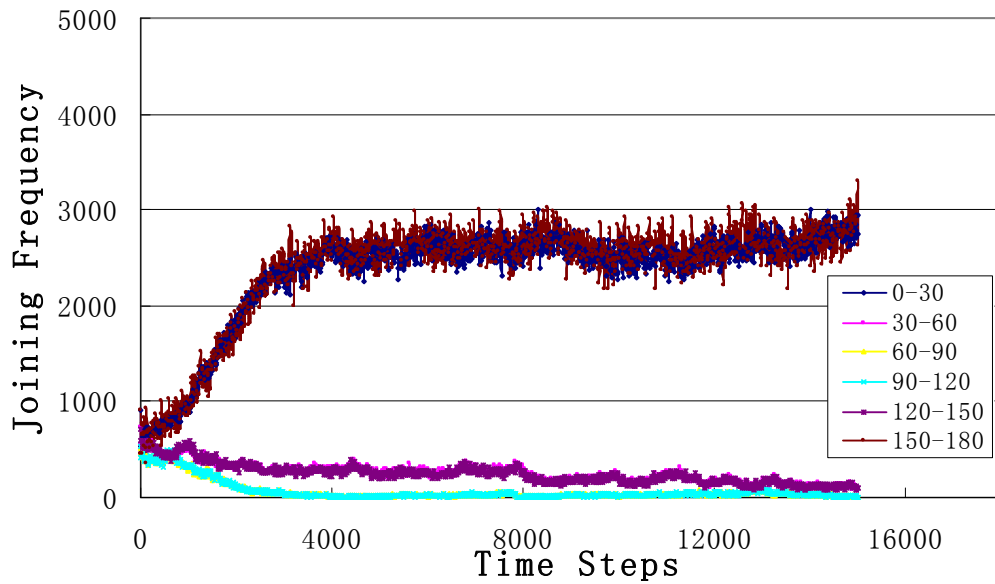


Fig.5.12 Joining frequency against time. Microtubule density = 10000/10000 μm^2
and bias rate = 0.024

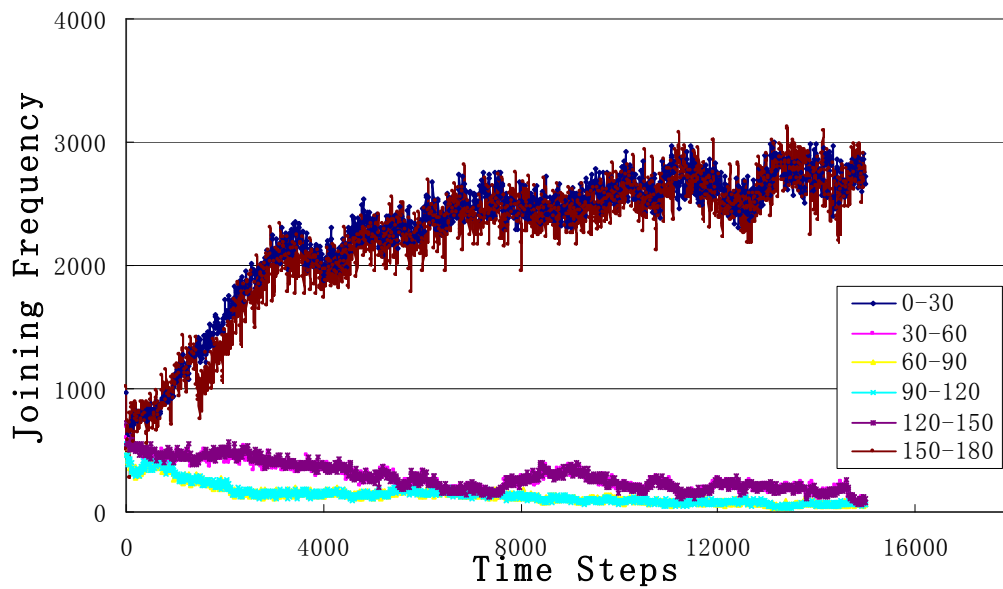
5.4.2 Influence of MT bias on the joining frequency

As mentioned earlier, the joining probability is influenced by the bias of microtubules. Fig.5.13 shows results of a quantitative analysis for self-organization processes with zero, low and high microtubule bias rates. As shown, the joining frequency for the low and high bumping angle ranges ($0^0 \sim 30^0$ and $150^0 \sim 180^0$) rapidly increased initially, and then became relatively stable. For middle bumping angles, the joining frequency decreased from about 500 to 100. It appears that the joining probability \sim time curves for different bias are similar. This may imply that although the MT joining is essential for MT self-organization

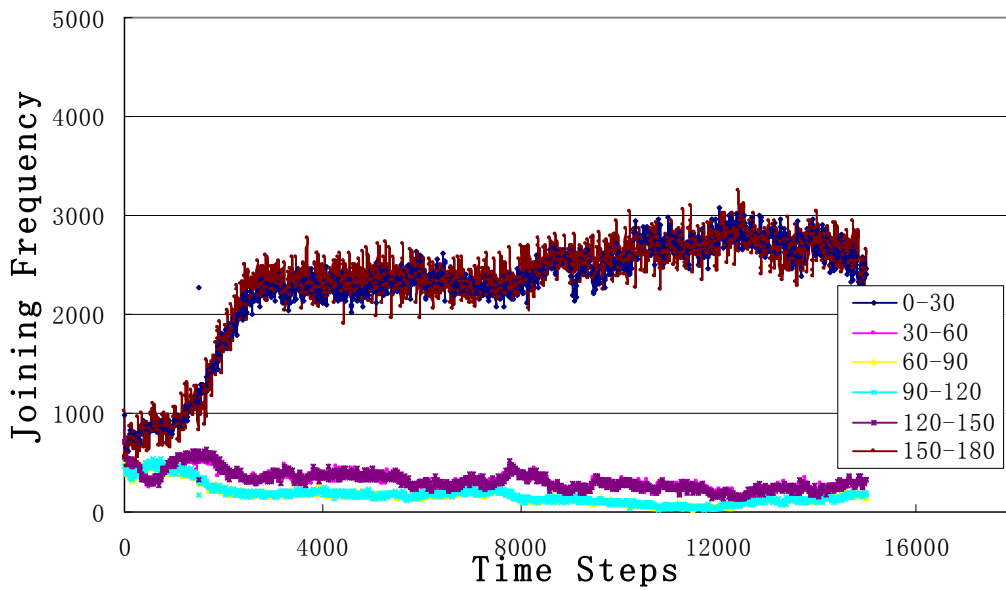
(the formation of MT bundles), the formation of circular patterns could be largely controlled by the MT bias.



(a)



(b)



(c)

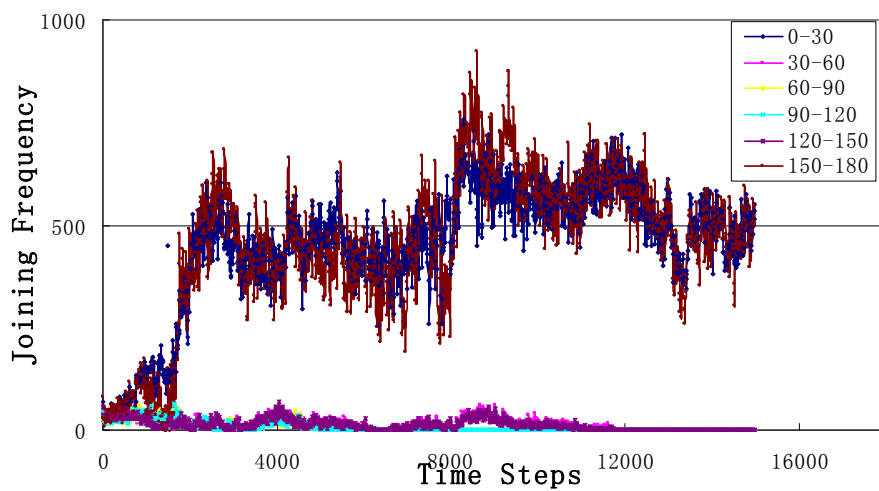
Fig.5.13 The joining frequency against time with different microtubule bias:
 (a) bias rate = 0; (b) bias rate = 0.006; (c) bias rate = 0.048. (Microtubule density
 = 2500/ μm^2)

5.4.3 The joining frequency and MT density

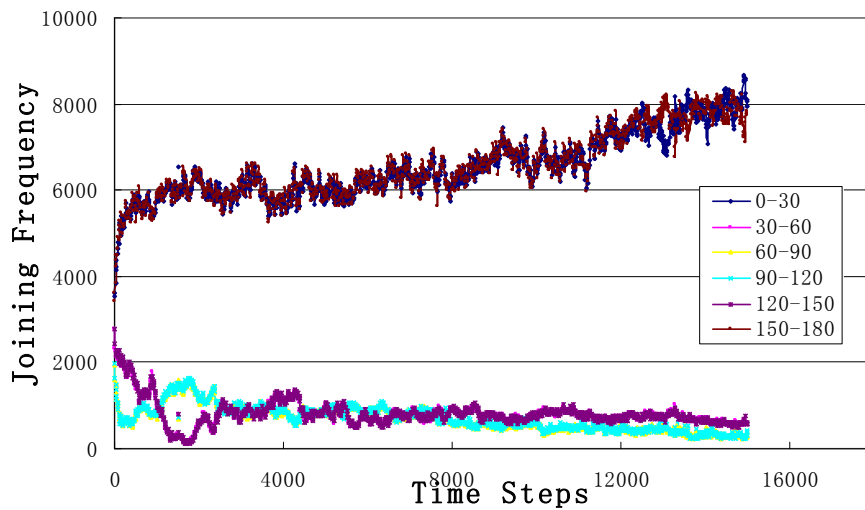
Fig.5.14 shows a quantitative analysis of self-organization processes with low and high microtubule densities. The bias rate was set to be 0.024. The joining frequency ~ time curves with both densities show similar trends but the values are very different. The lower microtubule density corresponds to lower joining frequency, which makes the self-organization less easy since the pattern formation needs the movement of a sufficiently large number of mutually influenced microtubules. In addition, with a low density, short microtubules may

not be able to form long bundles, which makes possibly generated polygon patterns unstable.

However, as indicated earlier, too many MT bundles would generate chaos in the system and result in small and irregular patterns. Therefore, controlling microtubule density is important for the self-organization of microtubules.



(a)



(b)

Fig.5.14 Joining frequency against time with different microtubule density: (a) density = $2500/10000 \mu m^2$; (b) density = $22500/10000 \mu m^2$

5.5 Conclusions

In this chapter, a phenomenological modelling study based on the general model incorporated with a Monte Carlo approach was conducted to investigate the self-organization of microtubules driven by randomly distributed dynein motors. The MT joining probability distribution, MT bias rate, and MT density were incorporated into the modelling to determine the roles that they play during the MT self-organization process. A cell list algorithm was also proposed to improve computing efficiency. The following main conclusions have been drawn from the modeling study:

- 1) Without the microtubule bias, microtubules formed linear bundles. The MT bias helped to form polygon patterns. Increasing the MT bias, the polygon became rounder or circular. However, further increases in the MT bias resulted in a disruption of the circular pattern; polygon pattern formed again and finally only linear MT bundles were observed in the system. The study suggests that the microtubule's bias is a key factor that leads to the formation of self-organized circular patterns.
- 2) The microtubule joining is necessary to the MT self-organization formation. Low joining probabilities resulted in polygon patterns with irregular shapes and sharp angles. With an increase in the joining probability, the polygons became round and relatively circular patterns

formed. However, further increase in the joining probability led to irregular polygon patterns again.

- 3) The microtubule density influenced the self-organization of microtubules. A lower MT density decreases the joining frequency and thus increases the difficulty in forming long and sufficient bundles for the formation of circular patterns. However, if the MT density is too high, the degree of disordering in the system increases, resulting in irregular patterns.

The self-organization process was analyzed in detail for more quantitative information. The obtained information would be useful to the design of potential nano-bio-machines.

References

1. Kellogg, D. R., M. Moritz, and B.M. Alberts. 1994. The centrosome and cellular organization. *Annu. Rev. Biochem.* 63: 639-674
2. Schiebel, E. 2000. Gamma-tubulin complexes: binding to the centrosome regulation and microtubule nucleation. *Curr. Opin. Cell Biol.* 12: 113-118
3. Sharp, D. J., G.C. Rogers, and J.M. Scholey. 2000. Roles of motor proteins in building microtubule-based structures: a basic principle of cellular design. *Biochim. Biophys. Acta.* 1496: 128-141
4. Oiwa K., D.Y. Li, Y. Shitaka, R. Nakamori and H. Sakakibara. 2007. Molecular and Nanometer-Scale Self-Organized System Generated by Protein Motor Functions. *Mater. Sci. Forum* 539: 3290-3296
5. Baulin, V. A., C.M. Marques, F. Thalmann. 2007. Collision induced spatial organization of microtubules. *Biophysical Chemistry* 128: 231-244
6. Glade, N., J. Tabony. 2005. Brief exposure to high magnetic fields determines microtubule self-organisation by reaction–diffusion processes. *Biophysical Chemistry* 115: 29-35

Chapter 6

Conclusions and Subjects for Future Studies

6.1 General summary of the research

In this research, a general modelling system was developed to simulate the kinetic behavior of microtubules driven by dynein motors. As described in chapter 2, a microtubule was treated as a polymer chain connected by microtubule beads. A dynein driving model was proposed to analyze the driving mechanism of dynein motors attached on a microtubule. Forces from microtubule's stretching and bending, driving and drag forces from dynein motors, and the environmental force were taken into account to determine the movement of microtubule. This model system can be incorporated with different approaches to deal with specific processes involving microtubules and motor proteins.

Chapter 3 reports the application of the general model in simulation of unidirectional motion of a single microtubule driven by dynein c, with incorporating a dynamic dissipative particles method. In this modelling, effects of motor's density, the length of microtubule, and the mixture of slow and fast motors on the motion of a single microtubule were studied, with the aim of investigating how the coordination among protein motors affects the microtubule movement. The computational results are in agreement with experimental observations reported in literature. It was demonstrated that the MT movement is greatly influenced by the coordination among protein motors. The force analysis indicated that, the average force on a microtubule was approximately zero, leading to a macroscopically constant speed of the microtubule. However, instant acceleration existed when a motor was attached to the microtubule. In addition, it

was demonstrated that there was a positive average force from the protein motors that drove the microtubule to move.

In chapter 4, experimental observations of two joining processes of microtubules driven by dynein c, microtubule-microtubule joining and microtubule-wall joining, are reported. It was demonstrated that bending dominated MT-MT joining while rotation was more obvious during MT-wall collision. The general model, which took account of the bending energy of microtubule and averaging solution effect, was extended to simulate two-dimensional motion – microtubule joining and collision. Simulation results are consistent with experimental observations. Quantitative computational analysis was made to investigate the instant bumping force, torque and related issues. Microtubule-microtubule joining showed a symmetric torque distribution, resulting in little rotation, while a positive torque distribution was found for microtubule-wall joining, responsible for obvious rotation. During microtubule-wall collision, a larger bumping force was generated, which could promote the rotation of the microtubule during the joining process. Such information would be helpful to the design of potential nano/micro-bio-machine systems by using micro-fabricated tracks for effective control of the microtubule movement and optimal arrangement of biological motors.

Chapter 5 reports a study on the self-organization phenomenon, motivated by recent experimental observations. Such self-organization of microtubules should be considered when developing potential nano-bio devices. A phenomenological model based on the general model with incorporation of a

Monte Carlo approach was proposed to investigate the self-organization of microtubules driven by randomly distributed dynein motors. In this work, the MT joining probability distribution, MT bias rate, and MT density were incorporated into the modeling to determine the roles that they play during the MT self-organization process. The simulation revealed a random-linear bundle-polygon-circular pattern formation process and demonstrated the important role that the microtubule's bias played in that the formation of self-organized circular patterns. The simulation also demonstrated that the microtubule joining probability distribution and the microtubule density greatly affected the self-organization of microtubules.

This modeling work helps to understand key parameters that influence the movement of microtubules driven by dynein motors and generate the information that is useful to the development of nano-bio-machine system.

6.2 The significance of the research

Protein motors have attracted increasing interest due to their demonstrated potential of being a biological motor for the development of future nano-bio-mechanical systems or devices, or as motors for potential transport vehicles for sensors and lab-on-a-chip applications, as well as the value of relevant research for better understating of various biological processes involving motor proteins. The success in controlling the movement of microtubules using modern nanotechnologies such as the electron beam lithography has considerably facilitated the control of bio-filaments driven by motor proteins, which has greatly

shortened the distance between the concept and reality for nano-bio-machine development.

This study has demonstrated and clarified a number of phenomena involved in the interaction between microtubules and dynein C, and identified various key parameters that govern the MT-dynein interaction and MT movement. This study generates valuable information for control of MT and motor proteins towards applications of the motor protein for nano-bio-applications and clarification of roles that motor proteins may play in various biological processes.

6.3 Suggested subjects for future work

1) Efficiency of protein motors

In Chapter 3, we analyzed the coordination function of dynein motors and the influence of mixed motors on microtubule movement. However, the efficiency of protein motors, which represents the ratio of kinetic energy consumed in driving microtubule to the total mechanical energy transferred from stored chemical energy, is still unclear. Such efficiency is important for nano-bio machine design. If knowing what factors affect the efficiency, we could develop optimal nano-bio machines design by increasing its efficiency through modifying these factors. However, it is very complicated to calculate such efficiency since many factors are involved, including bending energy, thermal energy, strain energy, chemical energy, and kinetic energy. Systematical investigations are needed.

2) The joining probability distribution of microtubule joining process

For controlled MT movement by micro-fabrication wall or self-organization of microtubules without wall restriction, microtubule joining plays a key role in these processes. In chapter 5, it has been demonstrated that joining probability distribution largely affects the self-organization of MTs. However, such probability distribution was obtained only from experimental observation, as described in chapter 4. Understanding how to control such probability distribution is important for nano device design using the microtubule-motor system. The joining probability distribution is affected by many factors, such as protein motor density and distribution, rigidity of microtubule and restricted wall, elastic modulus, velocity and length of microtubule, or properties of solution (such as viscosity or ATP concentration). Understanding the MT joining is challenging but worth being investigated with considerable efforts.

3) 3-D model

In present model, modeling was carried out in a 1-D and 2-D space. It assumed that one microtubule would not pass another microtubule, which was different from experimental observation. In some cases, microtubule could cross another microtubule without joining. Such situation could not be simulated by a two-dimensional model. In addition, as 2-D model, some important factors are not considered into model, such as vibration of microtubule on z direction, the self rotation of microtubule, or microtubule distortion, which decrease the accuracy of

modeling. A 3-D model would provide more details regarding MT-protein motors, MT-MT and MT-wall interactions.

4) Electrostatic effect among microtubules and between microtubule and protein motors

It seems that microtubules could be polarized, resulting in possible electrostatic interaction. Such effect may affect microtubule joining process. Two microtubules may attract each other if the positive pole of a MT gets close to the negative pole of the other while a resistant force may exist when two poles get close with the same type of charge. Such electrostatic effect may also affect the interaction between microtubule and dynein motors. In current model, the electrostatic interaction is not considered into model, since there is no sufficient information on the electrostatic interaction. In future work, it may be necessary to incorporate it into model, provided that sufficient experimental evidence and information have been obtained.

5) Microtubule bias

As demonstrated, the microtubule bias plays a crucial role in the self-organization of microtubules. However, it is unknown how the bias is generated and whether or not it could be influenced by interaction between microtubules and that between microtubules and motor proteins. In-depth investigation on this subject would help to clarify relevant issues involved in the MT dynamics and

movement as well as to more precisely predict and modify the self-organization of microtubules.

6) Extension of the current model for studies of medical problems

In present work, the general model has been demonstrated effective for studying microtubule motion and functions of dyneins in MT movement. Since bio-filaments and protein motors play important roles in cells of human body and many diseases are generated from malfunction of protein motors, such as Usher's syndrome and Kartagener syndrome, it is possible to modify the current model and apply it to analyze these biomedical processes.

Publications based on this work

1. Chen, Q., D.Y. Li, Y. Shitaka, and K. Oiwa. 2007. The coordination of protein motors and the kinetic behavior of microtubule--a computational study. *Biophysical Chemistry* 129:60-69
2. Chen, Q., D.Y. Li, Y. Shitaka, and K. Oiwa. 2009. Behaviors of microtubules (MTs) driven by biological motors (dynein c) at collisions against micro-fabricated tracks and MTs for potential nano-bio-machines. *Journal of Nanoscience and Nanotechnology* (in press)
3. Chen, Q., K. Oiwa and D.Y. Li. 2009. Phenomenological Simulation of self-organization of microtubule driven by dynein C. *Journal of Chemical Physics* (accepted)
4. Chen, Q., D.Y. Li, and K. Oiwa. 2009. Roles of Microtubule Bias and Joining in Self-Organization of Microtubule Driven by Dynein C – A Modeling Study. *Journal of Biomedical Science and Engineering* (accepted)

Appendix A Flow chart of the simulation of the unidirectional movement of microtubule driven by dynein motors

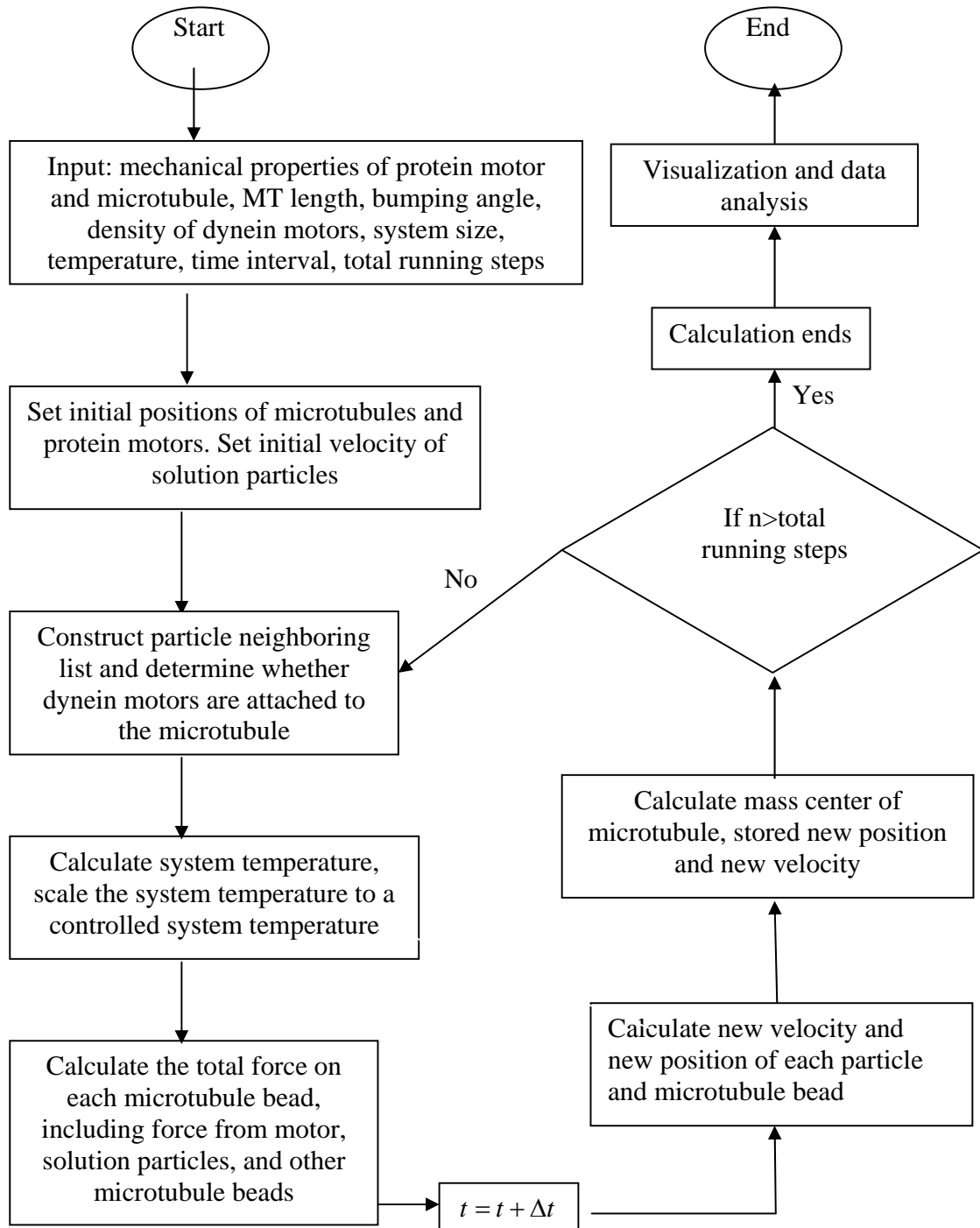


Fig.A.1 A flow chart of the simulation of the unidirectional movement of microtubule driven by dynein motors

Appendix B Flow charts of the simulation of microtubule joining driven by dynein motors

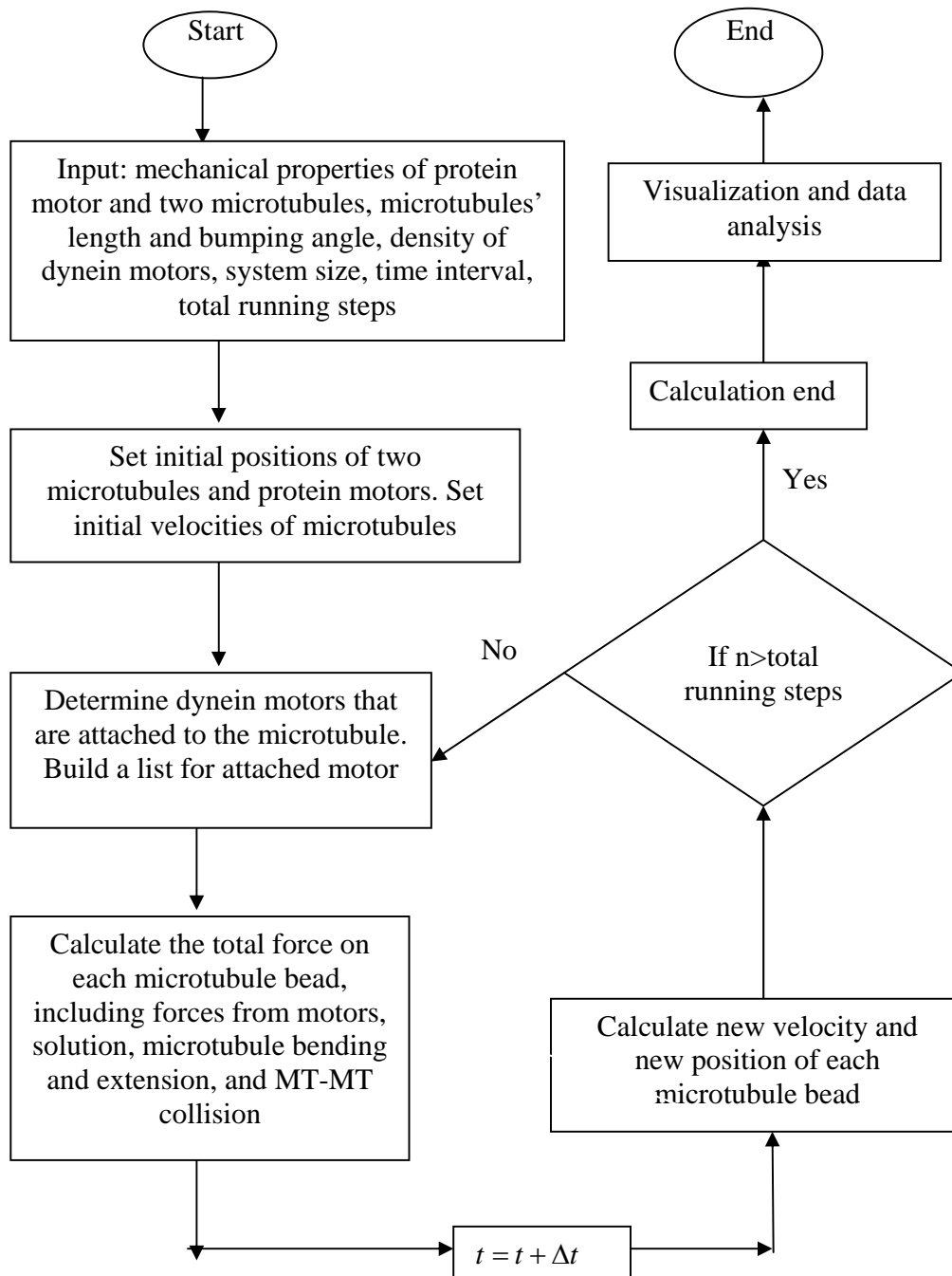


Fig.B.1 A flow chart of the simulation of microtubule-microtubule joining driven by dynein motors

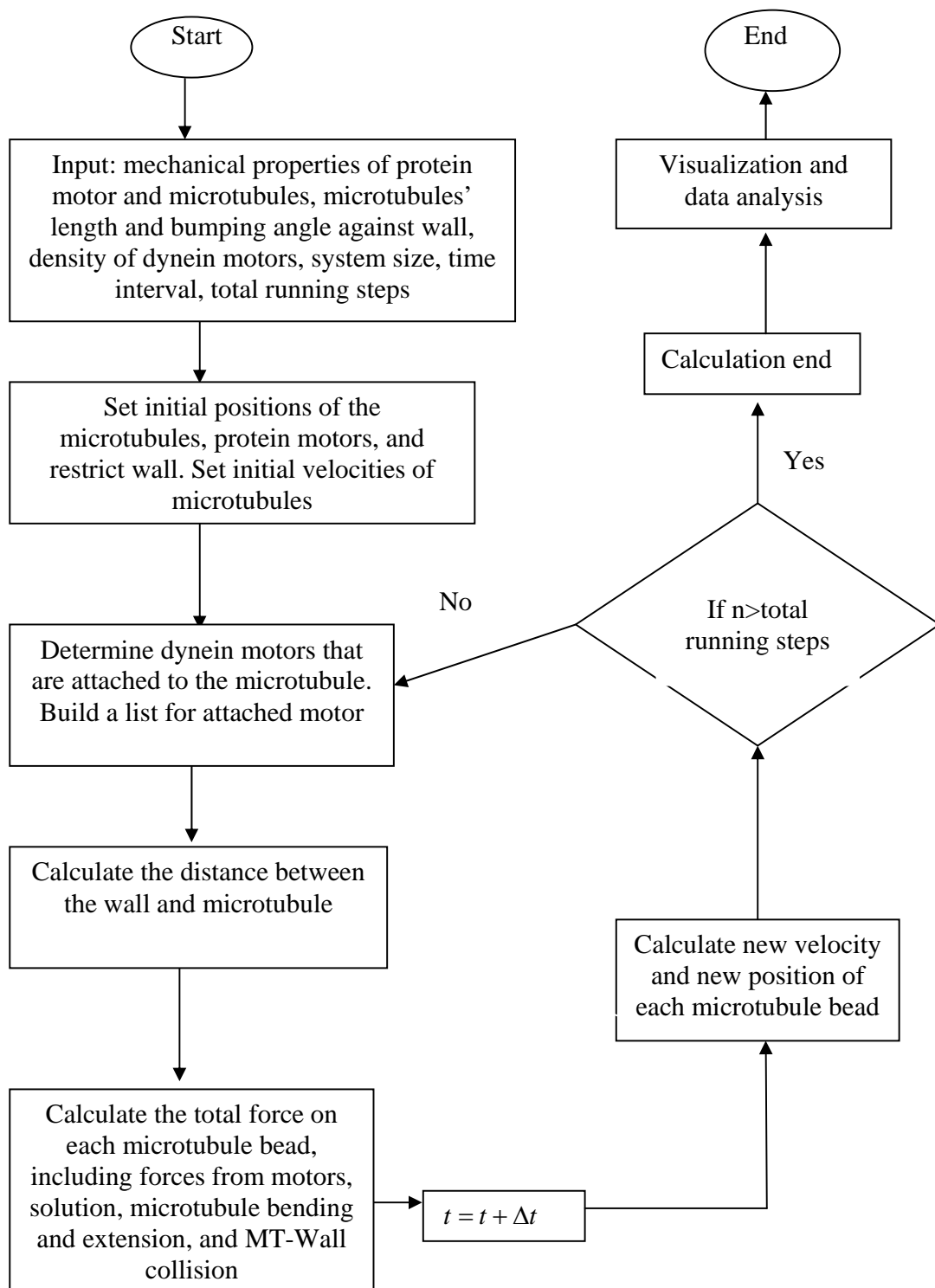


Fig.B.2 A flow chart of the simulation of MT-Wall joining driven by dynein motors

Appendix C A flow chart of Monte Carlo simulation of self-organization of microtubules driven by dynein motors

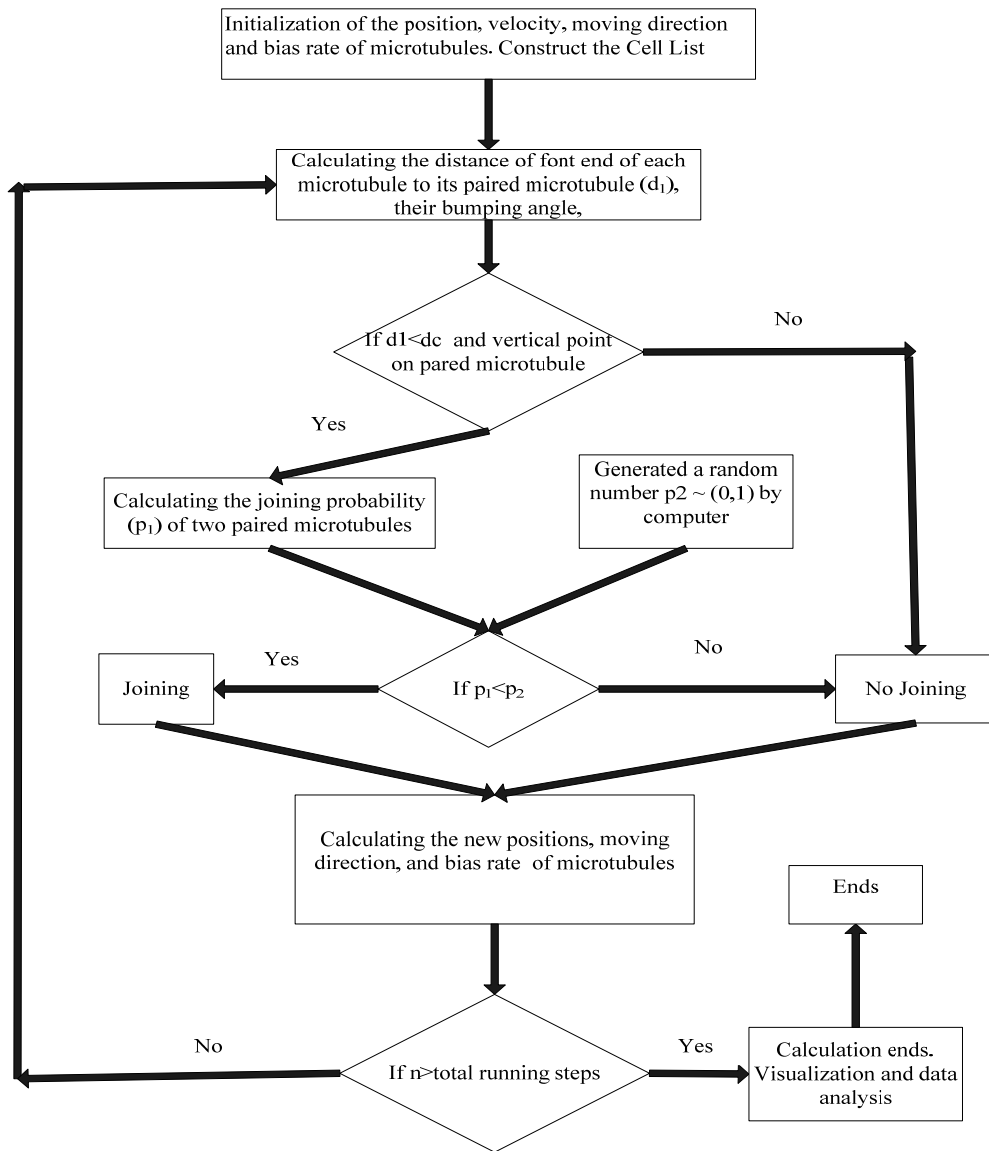


Fig.C.1 A flow chart of Monte Carlo simulation of self-organization of microtubules driven by dynein motors

Appendix D Deflection of microtubule during joining

A. Differential equation of deformed rod

For any point C on the axis of the rod, measured from the fixed origin B, is x in the direction of X-axis. As the rod deforms, its axis becomes curved and C is displaced.

The vertical deflection of C, denoted by v , is considered to be positive if directed in the positive direction of the Y-axis—that is, upward in Fig.D.1. From the geometry of the figure, we obtain

$$v' = \frac{dv}{dx} = \sin \theta \approx \theta \approx \tan \theta = \frac{y}{L} = \frac{y}{nl} \quad (\text{D.1})$$

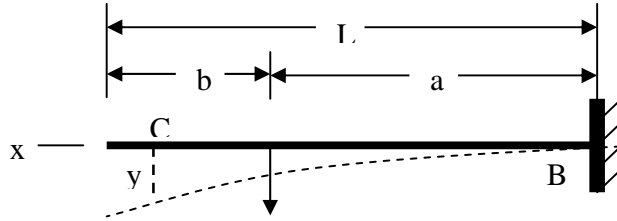


Fig.D.1 Sketch of beam deflection under a single load

Considering the relationship between the curvature of deformed rod,

ρ and the deformed angle, θ , we have

$$\frac{1}{\rho} = \frac{d\theta}{dx}$$

(D.2)

which can then be expressed as

$$\frac{1}{\rho} = \frac{d^2v}{dx^2} = v'' \quad (\text{D.3})$$

From flexure formula, we have the moment-curvature relationship

$$\frac{1}{\rho} = \frac{M}{EI} \quad (\text{D.4})$$

where M is the bending moment acting on the rod, E is the modulus of elasticity of the rod material, and I represents the moment of inertia of the cross-sectional area of the microtubule rod.

Substitution of Eq.(D.3) into Eq.(D.4) Therefore, a relationship between deflection and moment of beam can be derived as

$$v'' = \frac{d^2v}{dx^2} = \frac{M}{EI} \quad (\text{D.5})$$

which is called the differential equation of the elastic curve.

Two boundary conditions at the build-in end B also exist:

1. $v|_{x=0} = 0$ (suppose prevents rotation at B)
2. $v'|_{x=0} = 0$ (suppose prevents deflection at B)

B. Deflection of beam under a single load

$$M = \begin{cases} f(a-x), & 0 \leq x \leq a \\ 0, & a \leq x \leq L \end{cases} \quad (\text{D.6})$$

Substitute Eq. (D.6) into Eq. (D.5)

$$EIv'' = \begin{cases} f(a-x), & 0 \leq x \leq a \\ 0, & a \leq x \leq L \end{cases} \quad (D.7)$$

So

$$EIv' = \begin{cases} fax - \frac{1}{2}fx^2 + C_1 & 0 \leq x \leq a \\ C_2 & a \leq x \leq L \end{cases} \quad (D.8)$$

$$EIv = \begin{cases} \frac{1}{2}fax^2 - \frac{1}{6}fx^3 + C_1x + C_4 & 0 \leq x \leq a \\ C_2x + C_3 & a \leq x \leq L \end{cases} \quad (D.9)$$

For $v|_{x=0} = 0$ and $v'|_{x=0} = 0$, we have

$$C_4 = 0 \quad \text{and} \quad C_1 = 0 \quad (D.10)$$

For $v|_{x=a+} = v|_{x=a-}$ and $v'|_{x=a+} = v'|_{x=a-}$ we can obtain

$$C_2 = \frac{1}{2}fa^2 \quad \text{and} \quad C_3 = -\frac{1}{6}fa^3 \quad (D.11)$$

Hence the deflection of beam under a load (f) can be determined as

$$v = \begin{cases} \frac{fx^2}{6EI}(3a-x) & 0 \leq x \leq a \\ \frac{fa^2}{6EI}(3x-a) & a \leq x \leq L \end{cases} \quad (D.12)$$

Therefore, for any drag force from dynien with value $-f_k$ and distance from B as kl , we have

$$v = \begin{cases} \frac{-f_k x^2}{6EI}(3kl-x) & 0 \leq x \leq kl \\ \frac{-f_k k^2 l^2}{6EI}(3x-3kl) & kl \leq x \leq L \end{cases} \quad (D.13)$$

If a bumping force F in y direction exerts on distal end A (distance from B is L and $a = L$), then

$$v = \frac{Fx^2}{6EI}(3L - x) \quad (D.14)$$

C. Deflection of microtubule under complex loads during joining

Assume that there are $n-1$ dynein motors attached to a microtubule with length $L=nl$. When the microtubule bumps against a wall, the bumping force will generate rotation or bending of the microtubule, as Fig.1 shows

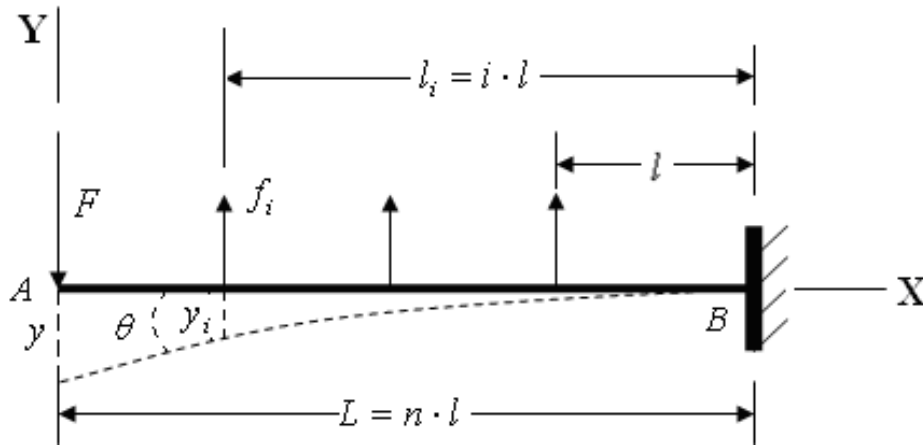


Fig. D.2 Sketch of bending of rod

In order to simplify the model, it was assumed that, during drift, each attached dynein generated the same displacement, which is called parallel drift. Hence, the drag force on each attaching point would be the same. From torque equilibrium

$$\sum_{i=1}^{n-1} f_i \cdot l_i = \sum_{i=1}^{n-1} f \cdot i \cdot l = \frac{n(n-1)}{2} fl = FL = Fnl \quad (D.15)$$

Then, the drag force f and parallel drift displacement y can be derived as

$$f = \frac{2F}{n-1} \quad (D.16)$$

$$\Delta y = \frac{2F}{k(n-1)} \quad (\text{D.17})$$

Here k is the spring constant of the dynein motor.

Using the method of superposition, which permits us to use the known displacement caused by simple loads to obtain deformations caused by a more complicated load, the deformation v can be expressed as

$$v = \frac{Fx^2}{6EI}(3nl - x) - \sum_{i=1}^k \frac{f_i i^2 l^2}{6EI}(3x - il) - \sum_{i=k}^{n-1} \frac{f_i x^2}{6EI}(3il - x), \quad (k-1)l \leq x \leq kl$$

$$v_A = \frac{Fn^2 l^2}{2EI} - \sum_{i=1}^{n-1} \frac{f_i i^2 l^2}{6EI}(3nl - il)$$

$$\theta_A = \frac{Fn^2 l^2}{2EI} - \sum_{i=1}^{n-1} \frac{f_i i^2 l^2}{2EI} \quad (\text{D.18})$$

Appendix E

DERIVATION OF THE BENDING FORCE OF MICROTUBULE

In Chapter 2, we have derived the bending force on bead i , which comes from the contribution of three bending energies between groups of three connected beads, $i-1$, i , and $i+1$:

$$\begin{aligned}
 F_{iB} &= - \sum_{j=i-1}^{i+1} \nabla(U_B(j)) \\
 &= - \sum_{j=i-1}^{i+1} \left(\frac{dU_B(j)}{d \cos(\theta_j)} \right) \cdot \nabla(\cos(\theta_j))
 \end{aligned} \tag{E.1}$$

where $U_B(i)$ is the bending potential of a short segment i , θ_i is the angle between vectors \vec{r}_{i-1} and \vec{r}_i , as Fig.E.1 illustrates.

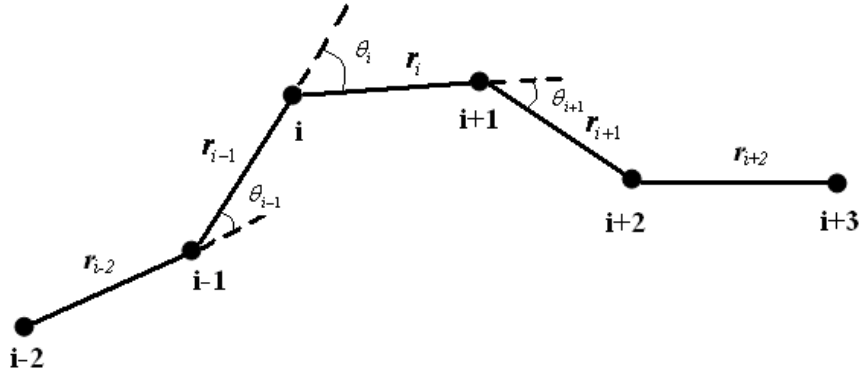


Fig.E.1 A bending microtubule chain

From Eq.(2.9), where have

$$U_B(i) = \frac{\pi E r^4 [1 - \cos(\theta_i)]}{8 \Delta l} \tag{E.2}$$

Substitution of Eq.(E.2) into Eq.(E.1)

$$F_{iB} = \frac{\pi E r^4}{8 \Delta l} \sum_{j=i-1}^{i+1} (\nabla(\cos(\theta_j))) \quad (\text{E.3})$$

We define

$$C_{a,b} = C_{b,a} = r_a \cdot r_b$$

and $D_{a,b} = D_{b,a} = C_{a,a} C_{b,b} - C_{a,b}^2$ (E.4)

Then the consines may be expressed in term of these parameters:

$$\cos \theta_i = \frac{r_i \cdot r_{i-1}}{|r_i| |r_{i-1}|} = C_{i,i-1} (C_{i,i} C_{i-1,i-1})^{-1/2} \quad (\text{E.5})$$

With respect to the position of knot i, there are a set of rules:

$$\begin{aligned} \nabla_{r_a} C_{a,a} &= 2d_a \\ \nabla_{r_a} C_{a,a+1} &= d_{a+1} - d_a \\ \nabla_{r_a} C_{a+1,a+1} &= -2d_{a+1} \\ \nabla_{r_a} C_{a,b} &= d_b \quad (b \neq a, a+1) \\ \nabla_{r_a} C_{a+1,b} &= -d_b \quad (b \neq a, a+1) \\ \nabla_{r_a} C_{b,c} &= 0 \quad (b, c \neq a, a+1) \end{aligned} \quad (\text{E.6})$$

Then, from Eq.(E.6), we derive

$$\begin{aligned} \nabla_{r_a} D_{a,a+1} &= 2C_{a+1,a+1} d_a - 2C_{a,a} d_{a+1} - 2C_{a,a} d_{a+1} + 2C_{a,a+1} d_a \\ \nabla_{r_a} D_{a,b} &= 2C_{b,b} d_a - 2C_{a,b} d_b \quad (b \neq a, a+1) \\ \nabla_{r_a} D_{a+1,b} &= -2C_{b,b} d_{a+1} + 2C_{a+1,b} d_b \quad (b \neq a, a+1) \\ \nabla_{r_a} D_{b,c} &= 0 \quad (b, c \neq a, a+1) \end{aligned} \quad (\text{E.7})$$

Combining the Eq.(E.5), (E.6) and (E.7), the equations required in Eq.(E.4) can be derived

$$\begin{aligned}
\nabla_{r_i} \cos(\theta_i) &= -(C_{i,j} C_{i-1,i-1})^{-1/2} ((C_{i,i-1} / C_{i,i}) d_i - d_{i-1}) \\
\nabla_{r_i} \cos(\theta_{i+1}) &= (C_{i+1,i+1} C_{i,i})^{-1/2} ((C_{i,i+1} / C_{i+1,i+1}) d_{i+1} - (C_{i,i+1} / C_{i,i}) d_i + d_{i+1} - d_i) \\
\nabla_{r_i} \cos(\theta_{i+2}) &= -(C_{i+2,i+2} C_{i+1,i+1})^{-1/2} ((C_{i+2,i+1} / C_{i+1,i+1}) d_{i+1} - d_{i+2})
\end{aligned}
\tag{E.8}$$

***NOTE: ALL equations in this part came from book: M.P Allen, Computer Simulation of Liquid, Appendix C, 1987**